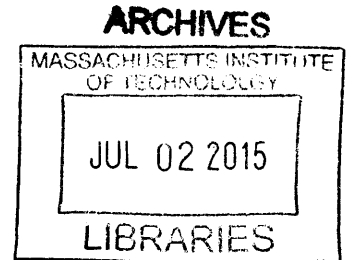


Finite Element Analysis of Embankment on Soft Indian River Clay

by

Evan Sau Yue Ma

Bachelor of Applied Science
University of Toronto (2014)



SUBMITTED TO THE DEPARTMENT OF CIVIL AND ENVIRONMENTAL ENGINEERING IN
PARTIAL FULFILLMENT
OF THE REQUIREMENTS FOR THE DEGREE OF

MASTER OF ENGINEERING IN CIVIL AND ENVIRONMENTAL ENGINEERING
AT THE
MASSACHUSETTS INSTITUTE OF TECHNOLOGY

JUNE 2015

©2015 Evan Sau Yue Ma. All rights reserved.

The author hereby grants to MIT permission to reproduce and to distribute publicly paper
and electronic copies of this thesis document in whole or in part in any medium now
known or hereafter created.

Signature redacted

Signature of Author: _____

Department of Civil and Environmental Engineering
May 21, 2015

Signature redacted

Certified by: _____

Andrew J. Whittle
Edmund K. Turner Professor in Civil Engineering
Thesis Supervisor

Signature redacted

Accepted by: _____

Heidi Nepf
Donald and Martha Harleman Professor of Civil and Environmental Engineering
Chair, Departmental Committee for Graduate Students

Finite Element Analysis of Embankment on Soft Indian River Clay

By

Evan Sau Yue Ma

Submitted to the Department of Civil and Environmental Engineering on May 21, 2015
in Partial Fulfillment of the Requirements for the Degree of
Master of Engineering in Civil and Environmental Engineering

ABSTRACT

This thesis re-analyzed the performance of an approach embankment for a new bridge across the Indian River Inlet in Delaware. The 115 ft. wide mechanically stabilized earth embankment (up to 45 feet above ground level) was founded on a 60 ft. deep layer of soft clay. Consolidation of the soft, normally consolidated clay was accelerated through installation of an array of prefabricated vertical drains. The performance was monitored during staged construction and for a period of 1.25 years after construction (2006-2008). During this, the embankment settled up to 6.5 feet, while large lateral spreading in the clay was restrained by overlying sand layers. The side walls tilted by up to 1.1° . The measured ground movement far exceeded the expectations of the designers and the embankment was eventually dismantled in 2008.

The current research evaluates site conditions from field investigations carried out in 2003 and 2007 which included a program of 1-D consolidation and triaxial laboratory shear testing on clay samples. Plane strain numerical analyses were carried out using PLAXIS 2D AE™ using the Modified Cam-Clay and MIT-E3 effective stress models to represent clay behaviour. The numerical predictions are generally in very consistent agreement with measured settlements below the embankment and with lateral deflections measured by inclinometers. The analyses show significant lateral deformations arise due to asymmetry in the loading particularly during the staged construction of the embankment. The current results suggest that the measured performance could be credibly predicted using available site investigation and laboratory test data.

Thesis Supervisor: Andrew J. Whittle

Title: Edmund K. Turner Professor in Civil Engineering

ACKNOWLEDGMENTS

First and foremost, I would like to thank my advisor, Professor Andrew J. Whittle. This thesis would not be possible without his careful and patient guidance. His knowledge and experience was invaluable and was extremely beneficial to my graduate studies here at MIT. I would also like to express my gratitude to have the opportunity to learn from Professor Herbert Einstein and Dr. John Germaine.

I wish to extend my gratitude to the Delaware Department of Transportation and to Mr. Frederick H. Schrank, Esq., Deputy Attorney General of the State of Delaware, for allowing Golder Associates to release the Indian River Inlet Bridge project data to MIT for research purposes. Further, I would also like to thank Dr. William F. Brumund of Golder Associates for allowing us the opportunity to dissect such a unique project and for offering us their time in providing insight on this analysis.

Thank you to Zhandos Orazalin for his instruction in getting me started with using the MIT-E3 model in PLAXIS. He was always available to help and was generous with his time.

Finally, I am extremely grateful for the love and support of my parents and to my grandmother for always being there for me all my life.

TABLE OF CONTENTS

ABSTRACT.....	2
ACKNOWLEDGMENTS	3
1.0 INTRODUCTION.....	10
1.1 PROBLEM STATEMENT	10
1.2 ORGANIZATION	11
2.0 BACKGROUND	13
2.1 SITE HISTORY	14
2.2 SITE INVESTIGATION.....	14
2.2.1 FIELD EXPLORATION PHASES	15
2.2.2 LABORATORY TESTING	16
2.3 SUBSURFACE STRATIGRAPHY.....	19
2.4 INSTRUMENTATION	21
2.5 CONSTRUCTION SEQUENCE.....	22
2.6 PREVIOUS ANALYSES BY OTHERS	23
3.0 DEVELOPMENT OF NUMERICAL FINITE ELEMENT ANALYSIS AT STA.289+00	30
3.1 SOIL PROFILE AND GEOMETRY	30
3.2 CONSTRUCTION SEQUENCE.....	31
3.3 INTERPRETATION OF DATA	31
3.3.1 ESTIMATION OF IN-SITU OVERBURDEN STRESS	31
3.3.2 EVALUATION OF DATA QUALITY	32
3.3.3 STRESS HISTORY	33
3.3.4 COMPRESSIBILITY PARAMETERS.....	33
3.3.5 HYDRAULIC CONDUCTIVITY AND CONSOLIDATION PROPERTIES ...	35
3.3.6 SHEAR STRENGTH PARAMETERS	37
3.4 INPUT PARAMETERS FOR MODELS	39
3.4.1 SAND PARAMETERS.....	39

3.4.2 MODIFIED CAM CLAY MODEL..... 41

3.4.3 MIT-E3 MODEL 42

3.4.4 MSE WALL PARAMETERS..... 44

4.0 FINITE ELEMENT ANALYSES OF STA.289+0054

4.1 BASE CASE ANALYSIS 54

4.2 EFFECT OF SOIL MODELING 56

4.3 PORE PRESSURE MEASUREMENTS 59

4.4 SETTLEMENT 59

4.5 LATERAL MOVEMENT 61

4.6 WALL TILT 63

4.7 SUMMARY OF MOVEMENT 64

5.0 CONCLUSIONS98

REFERENCES..... 102

APPENDIX A..... 104

List of Figures

Figure 2-1 Air Photograph of site looking towards the Southeast (Golder, 2011)	24
Figure 2-2. Borehole and cone penetration sampling plan	24
Figure 2-3. SPT $N_{1,60}$ at South bank based on MACTEC 2003a,b borings	25
Figure 2-4. Top of clay contours at South bank prior to new bridge construction	26
Figure 2-5. Index property of Indian River clay.....	26
Figure 2-6. Plan layout of instrumentation data at Sta. 289+00 (Golder, 2011).....	27
Figure 2-7. Available instrumentation and monitoring data at Sta.289+00 (Golder, 2011).....	28
Figure 2-8. Plan as-built wick drain extent and spacing.	29
Figure 3-1. Numerical model of Sta.289+00.	46
Figure 3-2. In-situ stresses below centerline of new roadway at Sta.289+00 at time of sampling (TOS) in June 2007.....	47
Figure 3-3. Stress history in clay at Sta.289+00.....	48
Figure 3-4. Compressibility parameters of the clay at the southern bank	49
Figure 3-5. Vertical hydraulic conductivity and coefficient of consolidation based on 1-D consolidation tests at the south bank.....	50
Figure 3-6. Strength parameters.....	51
Figure 3-7. In-situ undrained shear strength below centerline of new embankment comparison between initial condition and 2007 site investigation (Geocomp, 2007).....	52
Figure 3-8. CK_0UC Triaxial Testing (Geocomp, 2007)	53
Figure 3-9. Comparison of MCC and MIT-E3 effective stress paths and shear stress-strain behavior.....	53
Figure 4-1a. Total vertical stresses prior to new embankment construction	66
Figure 4-1b. Excess porewater pressure with $t=30$ years of consolidation of existing embankment	66
Figure 4-1c. Expected settlement beneath existing embankment assuming full consolidation....	67
Figure 4-2a. Vertical settlements at EOC (CD 273) for base case MCC analysis.....	68
Figure 4-2b. Vertical settlements at EOM (CD 773) for base case MCC analysis.	68
Figure 4-2c. Horizontal movements at EOC (CD 273) for base case MCC analysis.	69
Figure 4-2d. Horizontal movements at EOM (CD 773) for base case MCC analysis.....	69

Figure 4-3. Schematic relationship between maximum horizontal displacement and maximum settlement for a staged embankment construction (Ladd, 1991). 70

Figure 4-4a. Excess pore pressure at EOC (CD 273) for base case MCC analysis 71

Figure 4-4b. Excess pore pressure at EOM (CD 773) for base case MCC analysis. 71

Figure 4-5. Change in total vertical stress as a result of embankment construction predicted with the MCC model at cross section of Sta.289+00..... 72

Figure 4-6a. Vertical settlements at EOC (CD 273) with MIT-E3 analysis. 73

Figure 4-6b. Vertical settlements at EOM (CD 773) with MIT-E3 analysis. 73

Figure 4-6c. Horizontal movement at EOC (CD 273) with MIT-E3 analysis. 74

Figure 4-6d. Horizontal movement at EOM (CD 773) with MIT-E3 analysis. 74

Figure 4-7a. Excess pore pressure at EOC (CD 273) with MIT-E3 analysis. 75

Figure 4-7b. Excess pore pressure at EOM (CD 773) with MIT-E3 analysis. 75

Figure 4-8. Change in total vertical stress as a result of embankment construction predicted with the MIT-E3 model at cross section of Sta.289+00. 76

Figure 4-9. Undrained shear strength comparison with measured field data 77

Figure 4-10. Comparison of change in total vertical stress and excess pore pressure ratio as a result of embankment construction predicted with the MCC and MIT-E3 model below existing SR1 embankment (70R, -50 ft.)..... 78

Figure 4-11. Comparison of change in total vertical stress and excess pore pressure ratio as a result of embankment construction predicted with the MCC and MIT-E3 model in the zone of the wick drain (10L, -50 ft.)..... 79

Figure 4-12a. Pore pressure comparison between PLAXIS MCC prediction and measured data (10L, -50 ft.)..... 80

Figure 4-12b. Pore pressure comparison between PLAXIS MCC prediction and measured data (45L, -50 ft.)..... 80

Figure 4-13a. Pore pressure comparison between PLAXIS MCC prediction and measured data (10L, -70 ft.)..... 81

Figure 4-13b. Pore pressure comparison between PLAXIS MCC prediction and measured data (45L, -70ft)..... 81

Figure 4-14. Comparison between predicted, and measured settlement data at settlement plate 70L. 82

Figure 4-15. Comparison between predicted, and measured settlement data at settlement plate 35L.....	83
Figure 4-16. Comparison between predicted, and measured settlement data at settlement plate 15L.....	84
Figure 4-17. Comparison between predicted, and measured settlement data at settlement plate 53R.....	85
Figure 4-18. Lateral deformation comparison between PLAXIS prediction and measured data at inclinometer 75L.....	86
Figure 4-19. Lateral deformation comparison between PLAXIS prediction and measured data at inclinometer 55R.....	87
Figure 4-20. Lateral deformation comparison between PLAXIS prediction, Geocomp prediction, and measured data at inclinometer (75L, El. -32.3 ft.).....	88
Figure 4-21. Lateral deformation comparison between PLAXIS prediction, Geocomp prediction, and measured data at inclinometer (75L, El. -52.3 ft.).....	89
Figure 4-22. Lateral deformation comparison between PLAXIS prediction, Geocomp prediction, and measured data at inclinometer (75L, El. -72.3 ft.).....	90
Figure 4-23. Lateral deformation comparison between PLAXIS prediction, Geocomp prediction, and measured data at inclinometer (55R, El.-29.2 ft.).....	91
Figure 4-24. Lateral movement comparison of wall target and PLAXIS prediction at West Wall	92
Figure 4-25. Lateral movement comparison of wall target and PLAXIS prediction at East Wall	93
Figure 4-26. Slope of wall targets comparison with PLAXIS prediction at West Wall.....	94
Figure 4-27. Slope of wall targets comparison with PLAXIS prediction at East Wall	95
Figure 4-28. Deformed mesh predicted by the MIT-E3 model at embankment deconstruction. Deformations are exaggerated by five times relative to the true geometry.	96
Figure 4-29. Ground Movements at end of construction and embankment deconstruction.	97

List of Tables

Table 2-1. Summary of investigation program.	18
Table 3-1. Stages in construction of MSE embankment at Sta. 289+00.	31
Table 3-2. Selected compressibility parameters from oedometer and CRS testing.....	35
Table 3-3. Mohr-Coulomb Sand Properties used in PLAXIS	40
Table 3-4. Summary of MCC Parameters.....	41
Table 3-5. Summary of MIT-E3 Parameters	43
Table 3-6. Geogrid properties used in PLAXIS (vertical spacing=1.5 ft).....	44
Table 4-1. Comparison of measured and predictions at embankment deconstruction.	60
Table 4-2. Comparison of original predicted data, Golder 1-D consolidation analysis, current predictions and long-term consolidation settlement.	60
Table 4-3. Total lateral spread at end of monitoring, CD773	62
Table 4-4. Wall target predicted and observed comparison. Positive movement towards East. ..	63

1.0 INTRODUCTION

1.1 Problem Statement

Staged construction of earth embankments are an important geotechnical consideration for a wide variety of infrastructure and civil engineering projects. Often involving complex mechanisms, the stability and deformation of embankments constructed over soft ground must be properly engineered and analyzed. This thesis uses numerical, non-linear finite element analyses as a tool to model and predict large deformations of a highway embankment on soft clay. The project site is located at the Indian River Inlet in Delaware between Rehobeth Beach and Bethany Beach. The embankment overlies a 60 ft. thick layer of soft clay bounded between two layers of dense cohesionless soils.

The Indian River Inlet is currently bridged by a cable stay structure (completed in Spring 2012) with approach spans on either side of the inlet and carries State Route 1 (SR1). The approach earth fill embankment was constructed adjacent and partially on top of the existing SR1 embankment that was built in the 1960s. The new embankment is approximately 115 ft. wide and features a vertical, mechanically stabilized earth wall. As a result of large deformations that exceeded predictions by the designer, the embankment was eventually dismantled in May 2008. At that time the measured settlement were up to 6.5 ft., with lateral spreading up to 1.7 ft. at the top of the clay below the West wall of the embankment.

The mechanisms of ground deformation include a combination of differential undrained shear deformation and consolidation settlements. Previous research on the performance of embankments constructed over soft ground has been well established. Tavenas (1979) examine the lateral displacements underneath 21 embankments constructed directly on soft clay. Conventional methods to evaluate the undrained stability of embankments on soft ground are

based on the ratio of lateral deflections to vertical settlements as proposed by Matsuo and Kawamura (1977). Ladd (1991) recommended an undrained strength analysis approach to evaluate the stability of staged construction for foundations on soft clay. Methods for prediction of consolidation settlement of embankments on soft ground including both analytical and finite element approaches are summarized by Mesri (1985) and Olson (1998). The use of finite element and effective stress models for embankments research have been previously conducted at MIT by Ladd et al. (1994) on the I-95 test embankment. Previous Master's thesis on the geotechnical aspect of the Indian River Inlet bridge include an analysis of the geo-grid reinforced mechanically stabilized earth wall by Berkheimer (2007) at the University of Delaware.

The goal for this research is to evaluate the predictive capabilities of the effective stress models including the Modified Cam-Clay (Roscoe and Burland, 1968) and MIT-E3 (Whittle, 1993) in predicting the performance of the Indian River Inlet approach embankment. The model input parameters will be interpreted based on the available site investigation data and analyses are performed using a commercially available software, PLAXIS 2D AE™. The numerical predictions are evaluated through comparison with measured data for an instrumented section of the highway embankment.

1.2 Organization

Chapter 2 provides a discussion of the background for the project. This includes a site description of the project, site history, soil stratigraphy and geology. Field investigation and available laboratory testing data that are used for this thesis are described.

Chapter 3 describes the selection of parameters to be used in the effective stress models in the finite element analysis. This process has involved a careful re-analysis. The parameters for the

models are selected from an interpretation of the available data. A brief discussion on the required input parameters for the model is described.

Chapter 4 describes the results of the analysis and mechanisms controlling ground movements. The model predictions are compared with measured pore pressures, vertical settlements and lateral deflections as well as the tilt of the mechanically stabilized earth. The results are interpreted and analyzed in order to explain the mechanisms of the ground movements.

Chapter 5 summarizes the findings of the thesis and provide recommendations for further study.

Appendix A includes the text of the input data file and documentation required to use the MIT-E3 model in PLAXIS 2D AE™.

2.0 BACKGROUND

This chapter summarizes the project background including the site history, scope of field investigations for the new bridge approach embankments, laboratory testing, and primary description of the stratigraphy. All references to elevations are based on NAVD88 elevation datum as used on Delaware Department of Transportation (DelDOT) projects. This information was derived from a review of four key reports:

- 1) MACTEC (2003a) - Site Characterization and Preliminary Geotechnical Study dated on September 26, 2013 (Phase 1)
- 2) MACTEC (2003b) - Final Geotechnical Roadway Report dated on December 24, 2003 (Phase 2)
- 3) Geocomp (2007) - Independent Geotechnical Review dated on August 17, 2007
- 4) Golder (2011) - Geotechnical Assessment of Embankment Approach dated on January 3, 2011.

The project site is located at the outfall of the Indian River in the southeastern part of Delaware. An aerial photo of the site is shown in Figure 2-1. As a result of excessive scour, DelDOT made the decision to replace the existing State Route 1 (SR1) Bridge 3-156 in 2003 with a new structure built on an adjacent parallel alignment. The extent of the new construction encroaches on the existing SR1 embankment and was built on top of it. This thesis focuses on the performance of the earth fill approach embankment on the South side of the inlet. The proposed southern approach embankment begins at approximately Sta.285+00, and rises to a height of approximately 45 feet above ground level at its highest point at Sta. 295+00. The approximate width of the new embankment is 115 ft. wide. The existing SR1 embankment begins at approximately Sta. 285+00 rising to 35 feet at Station 295+00. Park facilities exist around the

base of the embankment connected by an access road. Apart from the approach embankments, the natural ground is relatively level (at El. +2.7ft).

Due to space constraints, the approach embankment is constructed as a mechanically stabilized earth (MSE) wall reinforced by geosynthetic grids. Each wall is approximately 1200 feet in length. To accommodate the expected settlements during staged construction, remediation measures include surcharge loading of up to 8 feet of earth and Prefabricated Vertical (PV) drains were used to accelerate the rate of consolidation. Vibrating wire piezometers, settlement plates, wall targets, and inclinometers were installed at several sections along the approach embankments, while wall targets and PK nail surveys were installed throughout the length of the roadway. Due to excessive ground deformations measured during and after construction (over a period of approximately 780 days) that greatly exceeded expected settlements by the designer, DelDOT decided to remove and reconstruct the embankments in May 2008.

2.1 Site History

Several bridges have historically spanned the Indian River Inlet. Earlier bridges consisted of a simple timber trestle bridge (1934), and a concrete and steel swing bridge (1938) that collapsed in 1948. This was replaced by a second swing bridge in 1952. In 1963, the Delaware Department of Transportation began construction on the State Route 1 (SR1) highway and embankment to the East of the previous bridges. The northbound SR1 bridge was completed in 1965 and the southbound SR1 bridge was completed later in 1976. In 2005, the construction began on the proposed replacement on top of portions of the existing embankment.

2.2 Site Investigation

Three rounds of site exploration were conducted in order to characterize the soil stratigraphy and engineering properties. Two phases of investigation were conducted as part of the original bridge

design works (MACTEC, 2003a, b) and a third phase was conducted in 2007 as part of an independent project review (Geocomp, 2007). It is important to note that the approach embankment was constructed to its full height at the time of the 2007 site investigation. Figure 2-2 shows the locations of the borings from all three field exploration phases. The borehole and piezocone soundings ground surface elevations, borings depths, and completed field and laboratory testing on the southern approach are summarized in Table 2-1.

2.2.1 Field Exploration Phases

The first MACTEC site investigation comprised twelve (12) deep borings (105-175 ft deep) were drilled on the southern bank of the Indian River, six of which were drilled near the proposed southern embankment (BI-01-BI-06). In-situ Ménard type pressuremeter (PMT) tests were carried out in boreholes BI-03 and BI-10.

The second phase included another thirty-eight (38) deep borings (105-170 ft deep) with BII-01 through BII-20 at the locations of the proposed southern approach embankment and pier locations. Field shear vane (FV) tests were performed at three depths within the clay layer in borehole BII-14, and in an additional test in borehole BII-20.

Geocomp (2007) drilled three (3) additional deep soil borings as part of their independent review. One of these (GC289-1) located along the centerline of the approach embankment at Sta.289+00, and two more (GC292-70-1, and GC292-70-2) were located at Sta. 292+70. Field shear vane tests were carried out in boreholes GC289-1 and GC292-70-1 at various depths in the clay stratum. These sections correspond to the location where instrumentation was available. Standard penetration tests were conducted at regular intervals in the borings.

Twenty (20) static piezocone penetration tests (CPTs) were performed in the second phase of site investigation (MACTEC, 2003b) including CII-01-CII-12 taken on the southern bank of the Indian River. These soundings were extended to depths ranging from 72 feet to 107 feet terminating at the base of the clay layer in the region of the southern approach embankment. Shear wave velocity tests measurements were also made using a seismic piezocone apparatus (CII-12 and CII-13)*. Measurements of pore pressure dissipation tests were obtained at six locations within the clay (CII-07, CII-09, CII-10, CII-11 (at two depths), and CII-13) in order to measure excess pore pressures in the clay. A further six (6) piezocone sounds were performed by Geocomp (2007). CPT289-1 through CPT289-5 were located at station Sta. 289+00, and the other test was located on the centerline of the new abutment at Sta. 292+70.

Groundwater levels prior to construction were monitored on a monthly basis in Phase 1 from wells installed in boreholes BI-2, BI-6, BI-7, BI-11 from August 2003 to November 2003. Observations found the groundwater levels vary from El. 0.0ft. to El. +4.7ft.

2.2.2 Laboratory Testing

The Phase 1 and Phase 2 site investigations included extensive index test data and a more limited program of laboratory tests for engineering properties comprising:

- 145 moisture content, 67 Atterberg limits, 66 sieve analysis,
- Ten (10) compression tests (Incremental load (IL) oedometer),
- Seven (7) undrained triaxial shear tests (CIUC).

* These data were obtained at 3 feet intervals using a downhole method

Geocomp (2007) generated further index property and physical property data and focused more exclusively on engineering properties of the clay:

- 28 Atterberg Limits, 23 Sieve Analysis, 7 Specific Gravity, 15 Unit Weight,
- Fifteen (15) 1-D Consolidation, Constant Rate of Strain (CRS) tests,
- Three (3) 1-D Consolidation (IL Oedometer),
- Thirteen (13) Undrained Direct Simple Shear Tests (CK₀DSS, Geonor Type) at a OCR=1, 2, and 4,
- Seven (7) Undrained Triaxial Compression Shear (CK₀UC) at OCR=1.

In addition, Golder Associates (2011) had completed rubber balloon and nuclear gauge tests to determine the fill weight and density of the new SR1 embankments.

Borehole ID	Date of Investigation	Elevation (ft)	Depth Completed (ft)	Key Field and Laboratory Testing [Test Type (Depth)]
BI-1	08/05/03	+2.6	105	
BI-2	07/21/03	+2.6	125	
BI-3	07/28/03	+2.5	110	PMT (63', 73') 1-D IL Consolidation (61', 41') CIUC (41', 51')
BI-4	07/31/03	+2.5	115	
BI-5	07/16/03	+2.6	147	
BI-6	07/16/03	+5.6	175	CIUC (56')
BI-7	07/16/03	+5.8	175	1-D IL Consolidation (42')
BII-1	10/02/03	+4.0	25	
BII-2	10/02/03	+4.0	25	
BII-3	10/17/03	+3.5	25	
BII-4	10/16/03	+3.5	25	
BII-5	10/20/03	+6.0	25	
BII-6	10/16/03	+3.5	25	
BII-8	10/16/03	+0.5	25	
BII-9	10/20/03	+2.1	105	1-D IL Consolidation (34')
BII-10	10/02/03	+2.8	110	PMT (6', 21', 26', 101.5')
BII-12	10/16/03	+3.0	120	1-D IL Consolidation (50')
BII-13	10/13/03	+3.8	25	

BII-14	10/28/03	+0.8	110	FV (42', 72', 57') 1-D IL Consolidation (74') CIUC (59')
BII-15	10/28/03	+1.3	94	
BII-16	10/13/03	+5.7	25	
BII-17	10/15/03	+27.9	125	1-D IL Consolidation (70') CIUC (70')
BII-18	10/23/03	+2.0	170	1-D IL Consolidation (61', 144')
BII-19	10/31/03	+2.9	175	PMT (108.5')
BII-20	12/01/03	+3.8	170	
CII-1	10/02/03	+4.0	72	
CII-2	10/02/03	+4.0	91	
CII-3	10/02/03	+4.0	94	
CII-4	10/02/03	+4.0	100	
CII-5	10/02/03	+2.5	100	
CII-6	10/02/03	+2.5	100	
CII-7	10/01/03	+3.0	72	Pore Pressure Dissipation (48')
CII-8	10/02/03	+3.7	107	
CII-9	10/01/03	+2.0	97	Pore Pressure Dissipation (68')
CII-10	10/01/03	+2.7	100	Pore Pressure Dissipation (55.1')
CII-11	10/01/03	+2.1	100	Pore Pressure Dissipation (40.4')
CII-12	10/01/03	+3.5	104	Seismic Shear Wave
GC289-1	05/18/07	+28.7	173	FV (68', 72', 76', 81', 86', 91', 96', 101', 106', 111') 1-D CRS Consolidation (65', 67', 75', 85', 100', 105', 110', 165') 1-D IL Consolidation (65', 80', 90') CK ₀ DSS (71', 85', 105', 165') CK ₀ UC (75', 90', 100')
GC292+70-1	05/29/07	+44.9	184	FV (81', 85', 90', 95', 100', 105', 110', 114', 120', 125', 130') 1-D CRS Consolidation (85', 90', 100', 115', 130') CK ₀ DSS (85', 100', 125') CK ₀ UC (90', 120')
GC292+70-2	05/31/07	+3.2	92	1-D CRS Consolidation (74') CK ₀ DSS (49' 76') CK ₀ UC (74')
CPT-289-1	05/29/07	+28.7	120	Pore Pressure Dissipation (71', 81', 91', 101', 111')
CPT-289-2	05/24/07	+3.0	100	
CPT-289-3	05/23/07	+1.6	100	Pore Pressure Dissipation (40', 50', 60', 70', 80')
CPT-289-4	05/22/07	+8.6	105	Pore Pressure Dissipation (40', 45', 50', 55', 60', 65', 70', 75', 80', 85',

				90', 95', 100')
CPT-289-5	05/25/07	+4.4	102	
CPT-292+70-1	05/24/07	+46.9	135	Pore Pressure Dissipation (88', 98', 108', 118', 128')

Table 2-1. Summary of investigation program.

2.3 Subsurface Stratigraphy

The Indian River estuary region belongs to the Atlantic coastal plain physiographic province on the Eastern seaboard of the United States. At the Indian River Inlet, the surficial deposits formations consist of recent Holocene deposits underlain by the Omar Formation and the Beaverdam Formation (Ramsay, 1999). The Holocene deposits are characterized by fine-medium to medium-coarse sand, clayey silt, silty clay, and organic rich clayey silt beds. The Omar Formation comprises the Pleistocene units that were deposited in lagoonal, tidal delta, marsh and spit environments and predominately comprises of grey clayey sand to sandy silt with scattered shell and organic deposits. The underlying Beaverdam is the oldest of the late Miocene to Late Pliocene comprised of fine to coarse sand interbedded with fine silty sand to sandy and clayey silt. The stratigraphy at the site includes four main soil units:

Stratum 1: Upper Sands

Stratum 1 consists of non-plastic alluvial sands deposits from medium dense to dense coarse sands (SP) and silty sands (SM) with average SPT \bar{N} -values=25±15 bpf. Corrected for in-situ overburden pressure, SPT $N_{1,60}$ values for the South bank are provided in Figure 2-3. The thickness of the stratum ranges from 23 feet to 46 feet, with thicker deposits to the North. The sand typically includes up to 8% of fine particles and has a natural moisture content, $w=18\pm 15\%$.

Stratum 2: Soft Clays

Soft compressible Holocene clays occur beneath the upper sands. These consist of plastic clays (CH), lean clays (CL), and highly plastic silts (MH). SPT blow counts were generally very low ranging from weight of hammer (WOH) to 12 blows, with an average $\bar{N}=2$ bpf. The top of clay elevations on the south embankment vary from El. -24 feet to -33 feet, and generally dip towards the North and the Indian River Inlet. Figure 2-4 shows a schematic of the top of clay contours. The thickness varies from 50 feet to 63 feet on the southern bank of the inlet. Average percent fines was found to be 94% with values from 74% to 100%. Natural moisture content ranged, $w=26\%$ to 68% , averaging 52% . Figure 2-5 summarizes the Atterberg limits within the clay layers, $w_L=32\%$ to 93% , averaging 55% and plasticity index, $I_p=11\%$ to 64% , averaging 38% , generally increasing with depth in the clay.

Stratum 3: Lower Sands

Medium dense to very dense fine to coarse sands (SP) and silty sands (SM, SP-SM) underlie the soft clay material with a wide range of SPT blow counts and an average $\bar{N}=30$ (Figure 2-3). The thickness of this layer ranged from 36 to 43 feet at the southern approach.

Stratum 4: Sandy Silty Clay

This layer comprises of medium-dense clayey sands (SC) and firm to stiff sandy clays (CL) with a few samples of plastic clay (CH). The thickness of the layer varies from 19 feet to 40 feet, and typically includes materials with fines content, $CF=59\pm 27$, $w=23\%$, $w_L=21\%$ to 51% and $I_p=8\%$ to 18% .

2.4 Instrumentation

Three stations on the southern approach were monitored with piezometers, settlement plates, and inclinometers at Station 285+00, 289+00 and 292+70. Additionally, wall targets and PK settlement nail data was made available. Figure 2-6 shows the plan locations of the monitoring instruments within the southern approach and Figure 2-7 shows the elevation of the locations installed at Sta. 289+00. All ground deformation measurements, wall target movements, and pore pressure monitoring were reported on a weekly basis.

The primary focus for this thesis will be on Sta.289+00. The instrumentation at this section includes four (4) vibrating wire piezometers installed within the clay stratum unit (Stratum 2) below the new embankment (Figure 2-7) at El. -50ft. and El -70ft. The VWP are installed in pairs offset at 10ft (10L) and 45ft (45L) west of the centerline of the new embankment. The piezometers are assumed to be located equidistant from the lines of the prefabricated vertical (PV) drains. They were installed between January 5 and January 10, 2006 and were monitored from February 2, 2006 to September 7, 2008.

Twenty-six (26) settlement plates were installed to observe the vertical ground settlements; these include four (4) SPs installed at Sta. 289+00 including settlement points measured relative to roadway centerline at 55 feet east (55R), 15 feet west (15L), 35 feet west (35L), and 70 feet west (70L). The plates were installed prior to the embankment construction and data are available from March 1, 2006 to September 7, 2008. However, no data was provided for the installation date.

Nine (9) vertical inclinometers were installed to measure the horizontal movements in the ground with two inclinometers installed close to the east and west faces of the MSE walls along the South embankment at each station. Inclinometers were installed 55 feet to the right (55R), and 75

feet to the left (75L) of centerline at Sta. 289+00 on February 6, 2006 with readings available from February 5, 2006 to March 10, 2008.

Two wall targets were installed on the West Wall (MSE Wall 1) at El. +12ft. and El. +28.5ft. on July 10, 2006, and October 19, 2006 respectively. Similarly, three wall targets were installed on the East wall (MSE Wall 2) at El+17 ft, El+21.5 ft, and El+26 ft on October 5, 2006. The measurements were base-lined on October 20, 2006 and October 14, 2006 for the West and East walls respectively.

2.5 Construction Sequence

Construction on the south embankment began on February 17, 2006 and was completed on February 20, 2007 (Construction Days (CD) 0). The rate of embankment construction was approximately 1.5 feet every two weeks, with the exception of a temporary suspension of construction activities in October 2006. The mechanically stabilized earth wall of the approach embankment was constructed with Tensar Uniaxial (UX) series high density polyethylene geogrids (Berkheimer, 2007) and wire aggregate baskets on the exterior face. Geogrid layers, 23 feet in length, were spaced every 1.5 foot intervals vertically with the MSE wall baskets. The embankment was backfilled in 8-inch thick lifts with borrow sand in the core and $\frac{3}{4}$ inch aggregate at the face and at the base of the walls. Deconstruction began May 5, 2008.

Prefabricated vertical drains (PVDs) were installed to accelerate consolidation processes within the clay during construction. The PVDs are band-shape plastic cores enclosed in a geotextile fabric with a nominal dimension of 4 inches, and were installed in a triangular grid with a spacing of 6 feet extending to depths of up to 115 feet through the underlying clay. PVD installation began on September 27, 2005 at the south embankment and was completed between

April 3 and April 28, 2006. Figure 2-8 shows the as-built location of the PV drains, which extend to 60 ft to the East (R) of the centerline of the roadway and 130 ft to the West (L).

2.6 Previous Analyses by Others

As part of the scope of work in the design of the 2003 embankment, MACTEC had prepared a report on the interpretation of geotechnical engineering parameters and an evaluation of embankment construction including settlement estimates along various sections of the proposed alignment (MACTEC, 2003b). Conventional geotechnical analysis including settlement calculation and limit equilibrium slope stability analysis. The designers had expected consolidations settlements of up to 3.75 feet under the centerline of the new embankment and 2.92 feet at the western edge of the new embankment (and 1 foot under the center line of the existing SR1 embankment) at Sta.289+00. With surcharge and wick drain placement, the expected time rate of settlement was 8 months for 95% consolidation (MACTEC, 2005).

Geocomp reinterpreted soil properties based on the Phase 3 site investigation (Geocomp, 2007) and revised the estimates of long-term settlement and lateral deflection through finite element analyses using the Soft-Soil-Creep model in PLAXIS 2D.

Additional geotechnical assessments were completed by Golder Associates (Golder, 2011) as part of design and investigative services for a lawsuit filed by DeIDOT. Golder had reinterpreted the data based on the MACTEC site investigation and predicted new results for settlement, and undrained shear deformations.



Figure 2-1. Air Photograph of site looking towards the Southeast (Golder, 2011)

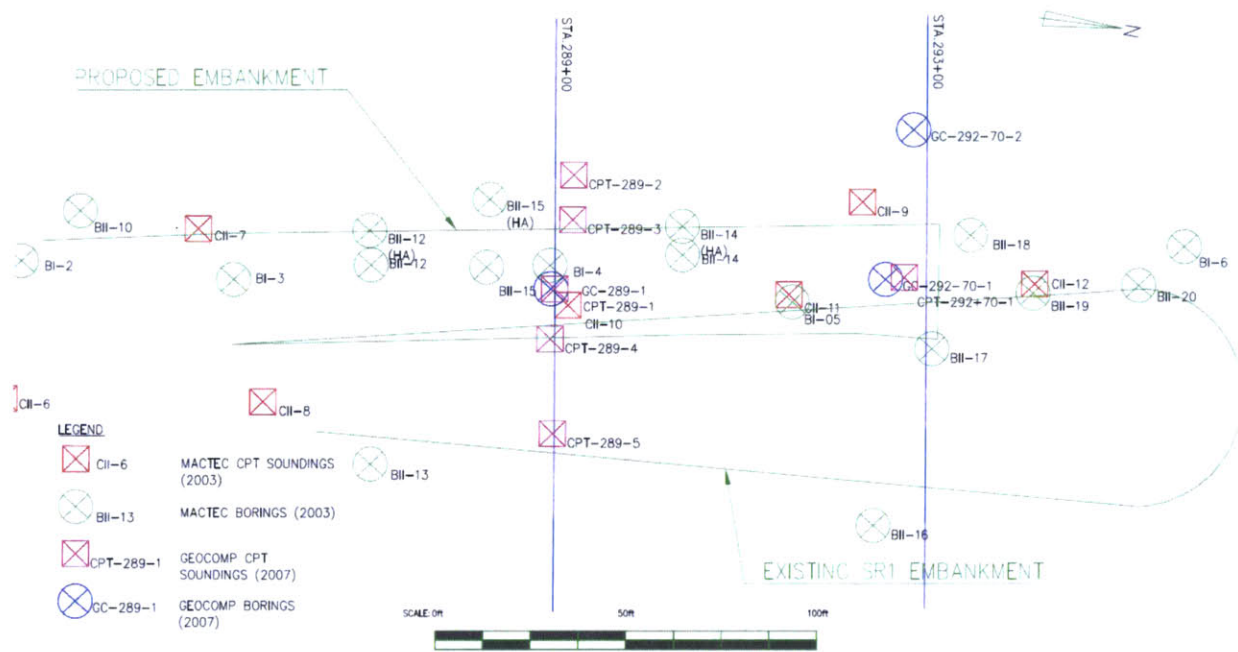


Figure 2-2. Borehole and cone penetration sampling plan

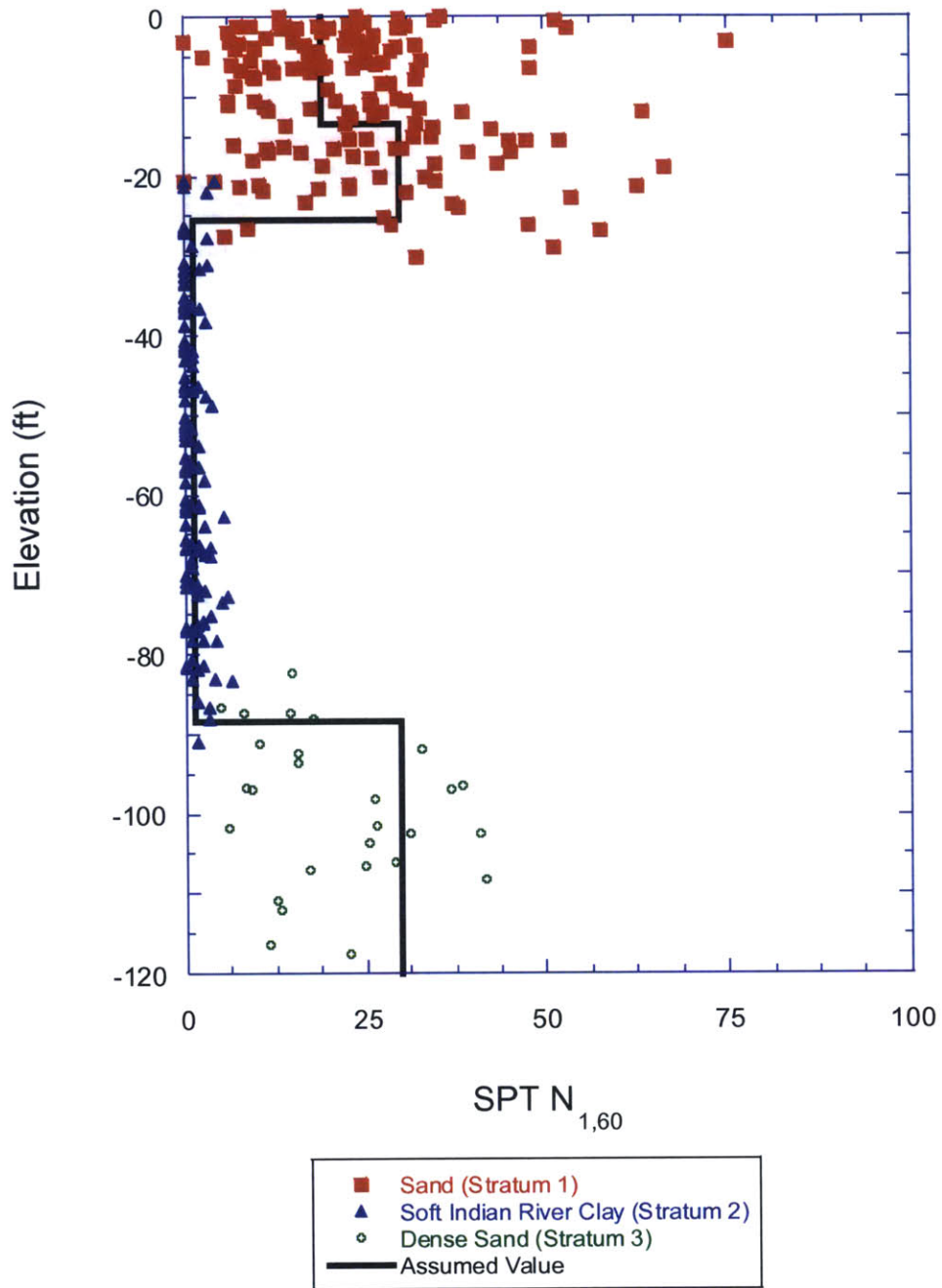


Figure 2-3. SPT N_{1,60} at South bank based on MACTEC 2003a, b borings

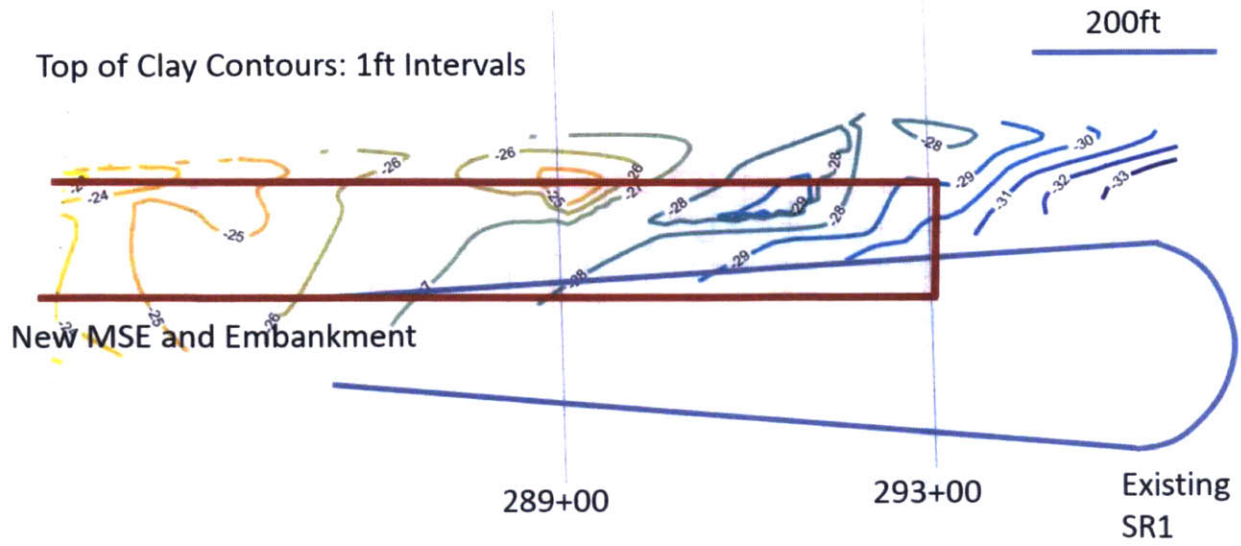


Figure 2-4. Top of clay contours at South bank prior to new bridge construction

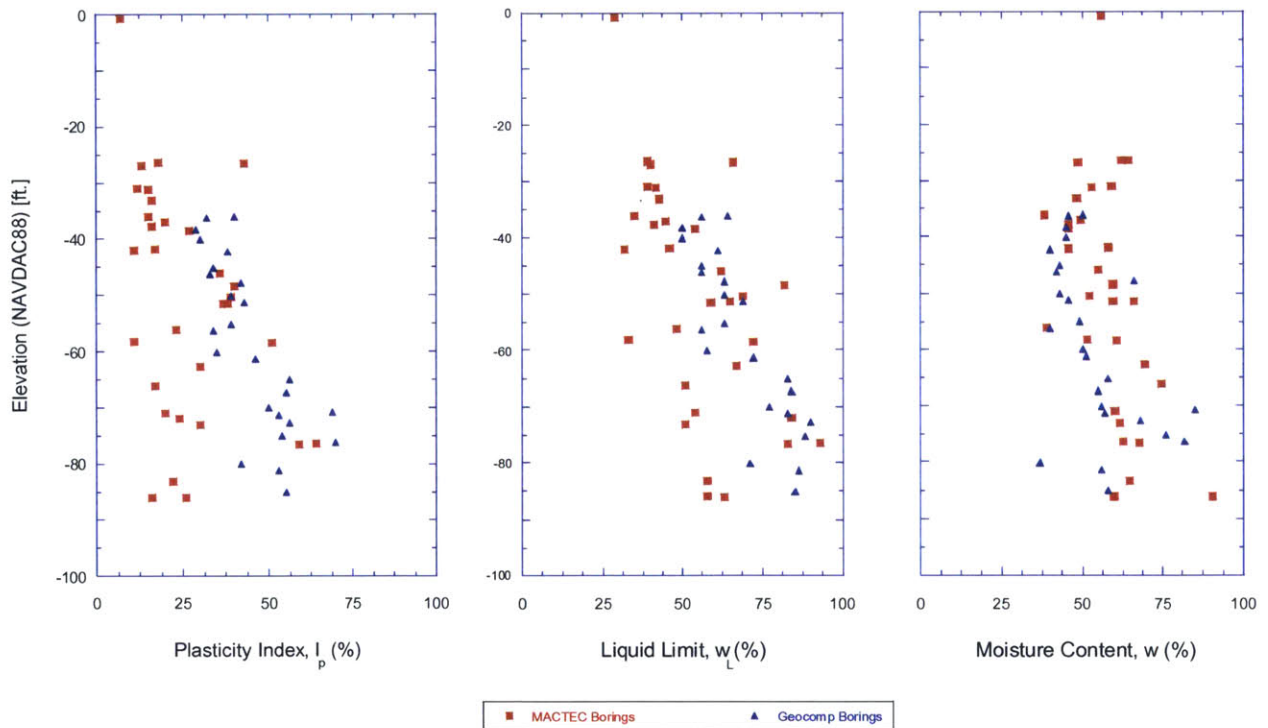


Figure 2-5. Index property of Indian River clay.

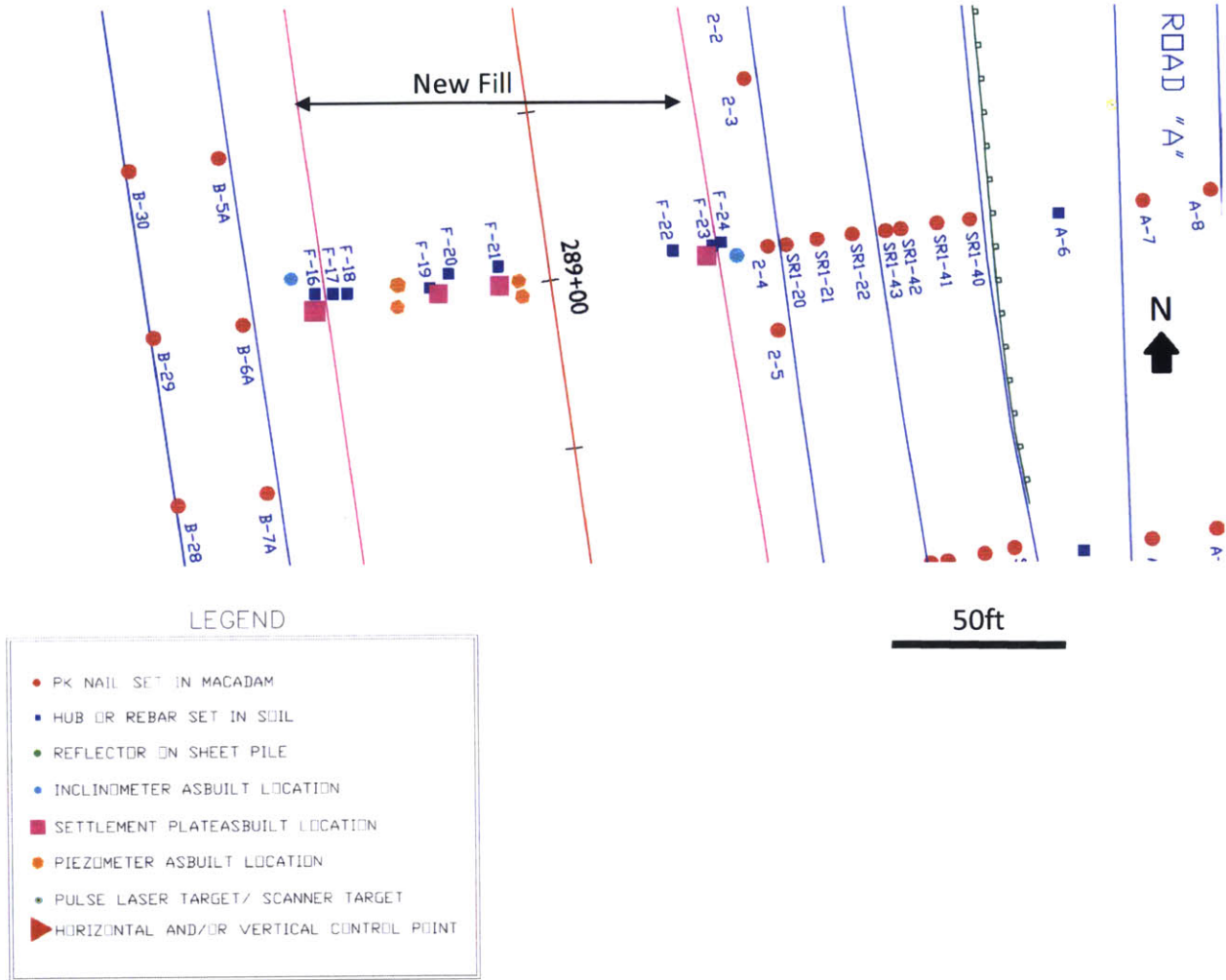
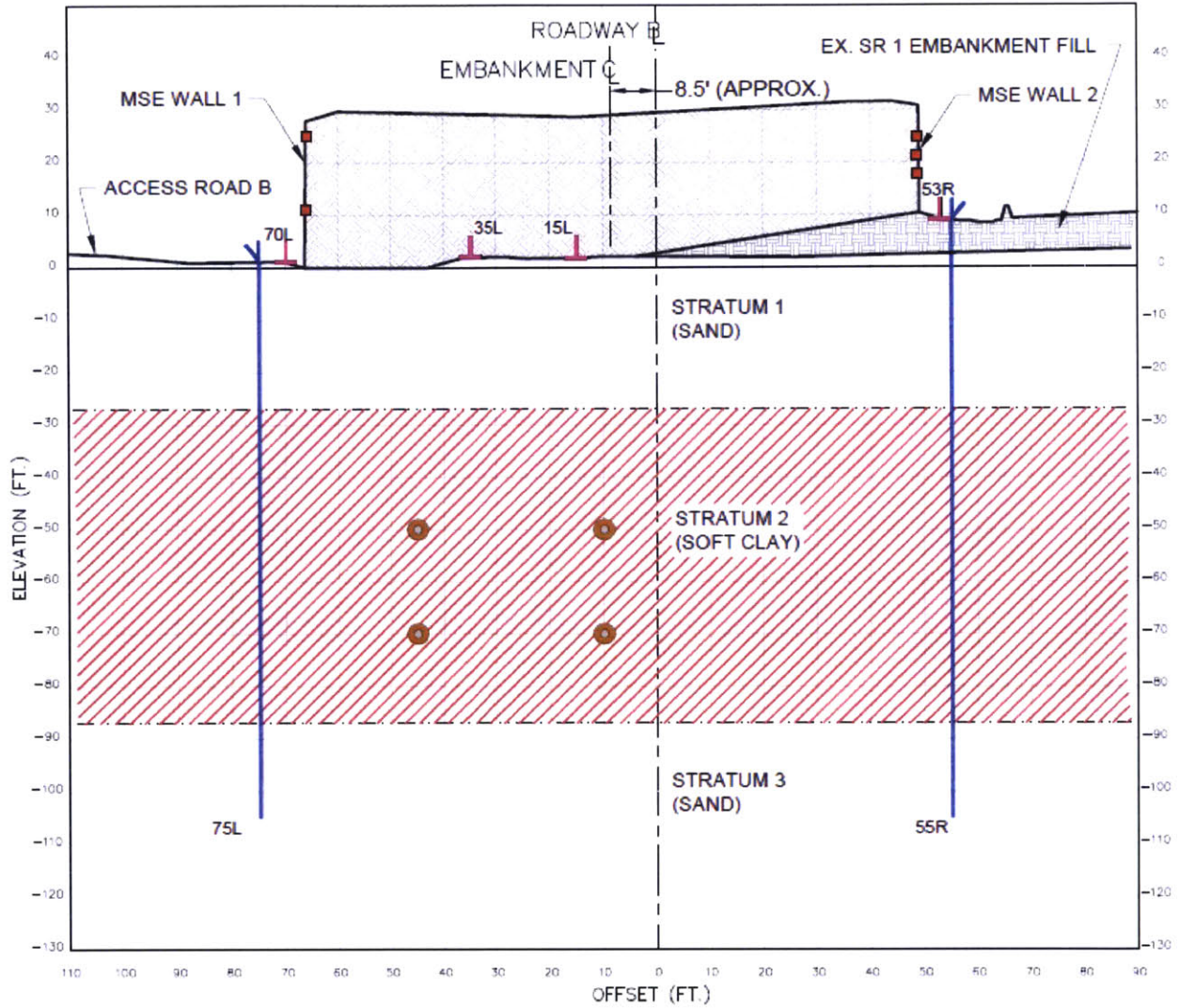


Figure 2-6. Plan layout of instrumentation data at Sta. 289+00 (Golder, 2011)



LEGEND





-  SETTLEMENT PLATE (15L, 35L, 70L, 53R)
-  INCLINOMETER (55R, 75L) (ELEV= -105')
-  PIEZOMETER (45L/-70', 45L/-50', 10L/-50', 10L/-70')
-  WALL TARGETS



Figure 2-7. Available instrumentation and monitoring data at Sta.289+00 (Golder, 2011)

3.0 DEVELOPMENT OF NUMERICAL FINITE ELEMENT ANALYSIS AT STA.289+00

This chapter describes the assumptions and interpretation of the soil stratigraphy, construction sequence, in-situ conditions, and material properties used to reanalyze the Southern approach embankment for the Indian River Inlet bridge. The thesis focuses on conditions at Sta. 289+00 due to the availability of measured data, and opportunity for comparison with prior work by others. Chapter 4 describes results of 2-D plane strain finite element analysis conducted with PLAXIS-2D AE™ (Brinkgreve et al., 2014).

3.1 Soil Profile and Geometry

At Sta.289+00, the initial ground surface is level at El. +2.7ft. In-situ groundwater conditions were assumed to hydrostatic, with horizontal soil layers comprising 28 feet of sand (Stratum 1), 63 feet of Indian River clay (Stratum 2), and 33 feet of sand (Stratum 3). An array of prefabricated vertical (PV) drains was installed through the full depth of the clay layer[†] at a spacing $s=6$ feet between $120L \leq x \leq 57R$. The new embankment at this point is 115.5 feet wide and the height is 33 feet (nominal top of embankment elevation at El. +35.7ft). It is constructed on the existing SR1 embankment which was opened to traffic in 1976 and is 9 feet high. As a result of limited data on pore pressure or groundwater conditions, there is an uncertainty about the state of the consolidation of the clay underneath the previous embankment. It was assumed that it was fully consolidated as the last construction in the area occurred more than 30 years ago before the time of construction. The vertical face of the embankment was constructed with mechanically stabilized earth (MSE) wall on either side with HDPE geogrid reinforcement,

[†] The limits of the wick drains were amended from the original design in 2005, which called for installation of wick drains to beyond 127 feet to the East, due to conflict with existing SR1 traffic. In addition, the contractor was unable to install the PV drains to full depth beyond Sta.289+50. However, the depth of the clay at Sta.289+00 remained unchanged.

exterior wire basket face, and sand backfill in the core. The assumed geometry is shown in Figure 3-1.

3.2 Construction Sequence

With consolidation analysis, the sequence and rate of construction will have an effect on the development of excess pore pressures and therefore the expected the rate settlement. Before construction of the new embankments, the existing SR1 embankment was constructed and the assumption was that it was allowed to consolidate until the excess pore pressures have been fully dissipated in the modeling. Table 3-1 summarizes the construction staging used to represent the construction of the southern approach embankment at Sta. 289+00.

Date Completed	Description	Duration (days)
-	Construction and Consolidation of Existing SR1 Embankments (Assumed Fully Drained)	(>30 years)
20-Feb-06	Wick Drains	1
15-Mar-06	Construct Approach Embankment to El 9.0ft	23
09-Apr-06	Construct Approach Embankment to El 12.2ft	25
18-Jun-06	Construct Approach Embankment to El 15.3ft	70
18-Jul-06	Construct Approach Embankment to El 21.7ft	30
21-Sep-06	Construct Approach Embankment to El 32.0ft	65
20-Nov-06	Construct Approach Embankment to El 35.7ft	60
03-Apr-08	Consolidation Until Deconstruction	500

Table 3-1. Stages in construction of MSE embankment at Sta. 289+00.

3.3 Interpretation of Data

This section discusses the assessment of sample and testing quality, followed by an interpretation of soil parameters for modeling.

3.3.1 Estimation of In-situ Overburden Stress

The soil properties of primary interest for this study were obtained from site investigation boreholes (MACTEC 2003a, b; Geocomp, 2007) close to the centerline of the new roadway (at Sta. 289+00). The 2003 data (Phases 1 and 2) are affected by stresses induced by the prior SR1 embankment, while the 2007 data are affected by the partially consolidated conditions beneath

the new embankment. Since sampling was conducted at two different points in time, the in-situ overburden stress must be estimated in order to analyze and discriminate the available test data at the time of the different sampling programs. In addition, the vertical effective stresses must be estimated in order to understand the stress history and over-consolidation ratio (OCR) of the clay. In-situ stresses along the centerline of the embankment were calculated from the available piezometer data and total vertical stresses were estimated using elastic solutions by Poulos and Davis (1974) before construction (Phases 1, 2) and at the time of sampling in 2007 (Phase 3). The pore pressures were analyzed from piezometers located 10 feet left of the center line and at elevations of -50ft, and -70ft, in the soft clay. Figure 3-2 summarizes the changes in vertical effective stress during construction and estimates the overburden stress at the time of Geocomp sampling in 2007.[‡]

3.3.2 Evaluation of Data Quality

In order to characterize the clay behavior, the available data must be interpreted. However, disturbance during sampling and poor laboratory testing may lead to large scatter in results and therefore erroneous interpretation. Sample quality was assessed with methods as described by Ladd and DeGroot (2003). In 1-D consolidation tests, sample disturbance is correlated with vertical strain, ε_{v0} , measured for re-loading to the in-situ overburden stress, σ'_{v0} . The available incremental load (IL) consolidation and constant rate of strain (CRS) tests were evaluated on this basis. For this project, the strain varies from $\varepsilon_{v0}=2.6\%$ to 20%. Tests with $\varepsilon_{v0}>9\%$ were considered to be of poor quality. Oedometer test with $\varepsilon_{v0}>14\%$ were discounted entirely and deemed to be unreliable.

[‡] Geocomp had performed a similar calculation for the in-situ vertical effective stresses, assuming a unit weight, $\gamma_t=120\text{pcf}$ constant throughout the depth of the soil layers. This analysis assumes unit weights consistent with the original design by MACTEC with total unit weights as outlined in Table 3-3 and Table 3-4.

3.3.3 Stress History

The stress history of a soft clay stratum is important in representing the 1-D mechanical yielding and is critical in all calculations of consolidation settlement. The overconsolidation ratio (OCR) is defined as the ratio between the vertical pre-consolidation pressure, σ'_p and the in-situ vertical effective stress, σ'_{v0} .

$$OCR = \frac{\sigma'_p}{\sigma'_{v0}} \quad (3-1)$$

Preconsolidation stresses were determined from oedometer data using the conventional Casagrande graphical method. The OCR prior to construction was calculated using the original MACTEC (2003a, b) data and a single 1-D consolidation tests from Geocomp (2007) borehole GC292+70-2 (Figure 3-3b) located away from the zone of influence of the new embankment during construction. Further 1-D Consolidation and CRS tests conducted by Geocomp (2007) were used to evaluate the OCR below the centerline of the new roadway at the time of sampling in 2007 (Figure 3-3c). The results show that tests with high sample disturbance (Poor, Figure 3-3a) are linked to $OCR < 1$ values while the more reliable measurements show $OCR = 1.0-1.3$ through the full depth of the layer. Measurements below the embankment centerline in June 2007 also consistently show $OCR \approx 1$.

3.3.4 Compressibility Parameters

Compressibility parameters are important in computing consolidation settlements of the clay stratum. The compression index, $C_c = \Delta e / \Delta \log \sigma'_v$, is defined by measuring the drained compression behavior in $e - \log \sigma'_v$ space corresponding to the virgin consolidation line. Similarly, the recompression index ratio of 1-D overconsolidated clay, C_r , is defined from the unload-reload behavior, typically averaged over one log cycle of stress. The compression indices

can be related to the more conventional Compression Ratio, CR, and recompression ratio as follows:

$$CR = \frac{C_c}{1 + e_0} \quad (3-2)$$
$$RR = \frac{C_r}{1 + e_0}$$

where, e_0 is the in-situ void ratio which can be estimated based on phase relationships assuming full saturation within the clay.

$$e_0 = \frac{G_s w}{S} \quad (3-3)$$

where, $G_s = 2.7$ is the specific gravity (MACTEC, 2003a,b)

S - saturation (1 if fully saturated)

w - natural moisture content (See Figure 2-5)

Figure 3-4a, b, and c summarize results of the in-situ void ratio, compression and recompression index for the IR clay. The results show significant scatter, even accounting for likely effects of effects of sample disturbance. Our best interpretation suggests that the clay stratum can be divided into two sub-units. The upper clay has lower in-situ void ratio and compression indices than the lower material (below El. -56ft.). As summarized in Table 3-2, typical properties of the upper clay include $e_0 = 1.4$, $C_c=0.6$, and $C_r=0.06$, compared to $e_0 = 2.4$, $C_c = 1.1$, and $C_r = 0.11$ for the lower clay. Using conventional 1-D consolidation analyses and our calculation of the vertical effective stress change due to embankment construction, these parameters yield settlement of 68.1 inches below the centerline of Sta.289+00 at end of primary consolidation.

Estimation of C_c by others were generally lower than our interpretation. MACTEC (2003) had used a single value for $C_c=0.5$ throughout the depth of the clay layer. Geocomp (2007) estimates $C_c=0.54$ at the top of clay at El -30ft increasing to $C_c=0.81$ below El. -79ft, assuming a consistent value for e_0 of 1.5 through the depth of the clay stratum. Golder Associates (2011) had interpreted $C_c=0.72$ and $e_0=1.669$ for the full depth of the clay.

Layer	Elevation	Compression Index, C_c	Recompression Index, C_r	In-situ Void Ratio, e_0
Upper Clay	-25.3 ft. to -56.0 ft.	0.6	0.06	1.4
Lower Clay	-56.0 ft. to -88.3 ft.	1.1	0.11	2.4

Table 3-2. Selected compressibility parameters from oedometer and CRS testing

3.3.5 Hydraulic Conductivity and Consolidation Properties

The hydraulic conductivity and consolidation properties of the IR clay can be interpreted directly from 1-D CRS and oedometer consolidation tests. Conventional consolidation theories assume that the vertical coefficient of consolidation, c_v , remains constant where:

$$c_v = \frac{k_v}{m_v \gamma_w} \quad (3-4)$$

k_v is the vertical hydraulic conductivity
 m_v is the coefficient of compressibility
 γ_w is the unit weight of water

In general, normally consolidated clays exhibit non-linear compression properties that can be characterized by the compression index, C_c :

$$e - e_0 = C_c \log \left(\frac{\sigma'_v}{\sigma'_{v0}} \right) \quad (3-5)$$

Similarly, the hydraulic conductivities, k_v , also varies with void ratio:

$$e - e_0 = C_k \log \left(\frac{k'_v}{k'_{v0}} \right) \quad (3-6)$$

$$\left(\frac{k'_v}{k'_{v0}} \right) = \left(\frac{\sigma'_v}{\sigma'_{v0}} \right)^{\frac{C_c}{C_k}} \quad (3-7)$$

The coefficient of consolidation, c_v , is therefore only constant for the case where the parameters $C_c=C_k$. In this case, the value of c_v is obtained as follows:

$$c_v = \frac{k_{v0}(1 + e_0)\sigma'_{va}}{0.434C_c\gamma_w} \quad (3-8)$$

σ'_{va} is the average vertical effective stress

The previous section reports values of C_c from 1-D compression tests, while Figure 3-5 shows values of k_{v0} and c_v from the oedometer and CRS tests (MACTEC, 2003a,b; and Geocomp, 2007, respectively). There is significant scatter in the k_{v0} (Figure 3-5a) but no discernible trend with depth.

On this basis, we selected an average value, $k_{v0}=1.00E-4$ ft/day for Stratum 2. Values of $c_v=0.058$ ft²/day and 0.042 ft²/day can then be derived from equation 3-8 for the upper and lower units of the IR clay, and are broadly consistent with data in Figure 3-5b. There were no measurements reported for C_k , and we assume $C_k=C_c$ in order to ensure that c_v remains constant throughout consolidation.

As the numerical model for this thesis uses a 2-D plane strain analyses (as opposed to a 3-D model), a further adjustment must be made to the permeability within the zone of PV drains. In order to account for this, the horizontal permeability is adjusted to ensure accurate representation of radial consolidation to the drains. Ignoring the effect of smear zones (that can affect PV drain efficiency), Hird et al. (1992) derive an expression for the equivalent permeability in the plane-strain model:

$$\frac{k_{ps}}{k} = \frac{2}{3(\ln(n) - \frac{3}{4})} \quad (3-9)$$

where, $n=d_e/d_w$

d_e is the influence zone of drain, for triangular spacing $d_e=1.05$ times spacing

d_w is the diameter of drain

Based on the geometry with $d_e=6.3$ ft., and a wick drain equivalent diameter, $d_w = 0.33$ ft., the ratio of plain strain to axisymmetric permeability was estimated to be 0.275. Therefore, the permeability in the wick drain section is reduced, $k_{ps}=2.75 \times 10^{-5}$ ft/day.

3.3.6 Shear Strength Parameters

Undrained shear strength parameters in the clay are always important to assess stability of staged construction projects and provide important guidance on expected changes in shear resistance of clay with consolidation. The three site investigations include a variety of sources of information on the undrained strength properties of the IR clay. These data are of highly variable quality and can be summarized as follows:

1. Phase 1 and 2 (MACTEC, 2003a,b) included a set of consolidated undrained triaxial shear tests (CU) on sets of samples from borings BI-3, BI-6, BII-14 (on Figure 2-2) in the vicinity of Sta. 289+00. The reported data include estimates of the drained effective stress envelope (c' , ϕ') from sets of three tests. The results are more scattered but suggest a friction angle $\phi'=23.6$ to 27.9° . MACTEC also reported three field vane tests, BII-14, with $s_u=390-400$ psf at depths ranging from 42 to 71 ft. (no information on correction factors). These data imply very low undrained shear strength ratios ($s_u/\sigma'_{v0}=0.1-0.14$) and are not considered reliable relative to expected properties of normally consolidated clays (Ladd, 1991).

2. Geocomp (2007) carried out much more extensive laboratory and investigations of undrained shear strength parameters. They report lab tests (in simple shear, CK_0 UDSS, and triaxial compression, CK_0 UC) for samples obtained from boring GC289-1 below the center of the new

SR1 approach embankment. Field vane data were also obtained from this borehole. In addition, they conducted a series of five piezocone tests (CPT-289-1 to CPT289-5) along the East-West transect at Sta. 289+00. Test CPT-289-1 is at the center of the new embankment, while CPT-289-2 and CPT-289-3 are located to the West of the new embankment and CPT-289-4, CPT-289-5 are to the East (below the pre-existing SR1 fill). These tests are difficult to interpret due to the uncertainties in the consolidation effective stress state within the clay (See Figure 3-2). Geocomp made a careful comparison and found reasonable agreement between ‘benchmark’ laboratory DSS tests (assumed to be normally consolidated with $s_{uDSS} = 0.24 \sigma'_{vc}$) and

- 1) Field vane tests, s_{uFV} obtained with a vane correction factor, $\mu=0.6$ (Bjerrum, 1972),
- 2) Piezocone Test (CPT289-1) with a cone factor $N_k=11$.[§]

As shown in Figure 3-7, their interpretation implies that prior to construction of the new embankment, s_u varies linearly with depth from 0.5-1.2 ksf. At the time of the Geocomp investigation, the undrained shear resistance at the top of the clay is estimated as $s_u=1.4$ ksf, decreasing to a minimum value of $s_u \approx 1.1$ ksf at the mid-layer and exceed $s_u > 1.5$ ksf at the base of the clay.

While this interpretation is credible, it is important to emphasize that it is highly dependent on the interpreted consolidation stress state, σ'_{vc} , and is based on a small number of pore pressure measurements. In reality, radial drainage/consolidation produces large gradients in effective stresses within the zone of PV drains. The Geocomp estimate is likely a lower bound on available shear resistance at a midpoint section between the PV drains.

[§] Geocomp had selected a cone factor of $N_k=11$ based on laboratory undrained DSS tests which suggest an undrained strength ratio, $s_u/\sigma'_{vc} = 0.24$.

The numerical analyses performed in this thesis use effective stress soil models (MCC, MIT-E3) that predict undrained shear strength as a function of selected material properties and consolidation stress state. These soil models must be calibrated from reliable laboratory shear test data. The most widely used calibrations are done using undrained triaxial compression tests (CK₀UC). Hence, we have focused on data reported by Geocomp (2007). The Geocomp test program includes a set of four CK₀UC tests that are consolidated to stress levels within the normally consolidated range (ie. $\sigma'_{vc} \geq \sigma'_p$) as shown in Figure 3-8. The results include shear stress-strain and effective stress paths for undrained theory to axial strain levels, $\epsilon_a > 10\%$. The data enable estimation of the large strain friction angle, $\phi'_{TC} = 31^\circ, 37^\circ$ ($\sin\phi' = \tan\alpha'$). Two pairs of tests, assumed to represent the upper and lower units of IR clay, are shown in Figure 3-8a. The tests have $K_0 = 0.46, 0.54$, and undrained strength ratios $s_{uTC}/\sigma'_{vc} = 0.34-0.36$ and $0.30-0.32$, respectively. The peak undrained shear resistance is mobilized at shear strain levels at $\epsilon_a \approx 0.5$ and 2.0% respectively.

3.4 Input Parameters for Models

This section will briefly summarize the required input parameters for the modeling of the soil as well as the embankment walls.

3.4.1 Sand Parameters

The sand materials were modeled as Mohr-Coulomb (MC) soil model, a linear elastic, perfectly plastic soil model. The model requires elastic stiffness parameters, (E', ν'), and Mohr-Coulomb strength parameters, (c', ϕ'). In the absence of advanced soil testing techniques used for this project, we assumed the sand is fully drained, and cohesionless ($c'=0$). Young's modulus and friction angle were estimated from SPT empirical correlations.

It is understood that there exist a wide range of uncertainty in the determination of friction angles from SPT correlation. However, the overall magnitude and shape of the ground deformations does not differ significantly for reasonable ranges of those properties. A correlation proposed by Hatanaka and Uchida (1996) with normalized SPT $N_{1,60}$ values was used as an approximation. Figure 2-3 shows the SPT $N_{1,60}$ values for the southern approach.

$$\phi' = [15.4(N_1)_{60}]^{0.5} + 20^\circ \quad (3-10)$$

For an average SPT $N_{1,60}=19$ for the medium sand and $N_{1,60}=30$ for the dense sand, the resulting parameters are $\phi'=38^\circ$ and 42° , respectively. Similarly, a range of values can be interpreted for the stiffness. A correlation with SPT is given by Bowles (1997) for normally consolidated sands.

$$E = 500(N + 15) \text{ [kPa]} \quad (3-11)$$

For the same values of SPT above, this corresponds to a stiffness of approximately 400 ksf and 500 ksf for the medium and dense sand layers respectively. Table 3-3 provides a summary of the modeling parameters for the sand material.

Parameter	Stratum 1 – Medium Sand	Stratum 2 – Dense Sand	Stratum 3 – Dense Sand	New Embankment Fill	Existing SR1 Approach Fill
Drainage	Drained	Drained	Drained	Drained	Drained
Top Elevation (El. ft.)	2.7	-13.3	-88.3	35.7	12.2
Unit Weight, γ_t (pcf)	120	125	125	125	125
E' (ksf)	400	500	1000	1000	500
v	0.32	0.3	0.3	0.3	0.3
ϕ' (°)	38	42	42	42	42

Table 3-3. Mohr-Coulomb Sand Properties used in PLAXIS

3.4.2 Modified Cam Clay Model

The Modified Cam Clay (MCC) is a well-known critical state soil model developed by Roscoe and Burland (1968). The model requires five input parameters:

1. Poisson's Ratio, ν'_{ur}
2. Compression index, λ ($=0.435C_c$)
3. Swelling index, κ , (assumed to be linked to C_r)
4. Large strain friction angle, ϕ'_{TC} ($M=6\sin\phi'_{TC}/3-\sin\phi'_{TC}$)
5. Initial in-situ void ratio.

It was assumed that the clay is K_0 normally consolidated prior to construction of the original SR1 embankment. Table 3-4 summarizes the input parameters for upper and lower units of the IR clay using the MCC soil model.

Parameter	Upper IR Clay	Lower IR Clay
Top Elevation (El. ft)	-25.3	-56.0
Unit Weight, γ_t (pcf)	100	100
λ [C_c]	0.261 [0.6]	0.478 [1.1]
κ [C_r]	0.0522 [0.06]	0.0957 [0.11]
ν	0.25	0.25
e_0	1.4	2.4
K_0	0.54	0.45
M [ϕ']	1.243 [31°]	1.506 [37°]
OCR	1	1
k (ft/d)	1.0E-4	1.0E-4
C_k	0.6	1.1

Table 3-4. Summary of MCC Parameters

3.4.3 MIT-E3 Model

The MIT-E3 model is an advanced effective stress model that describes the rate independent behavior for normally to moderately overconsolidated clay including small-strain non-linearity, anisotropic stress-strain-strength and hysteresis due to cyclic loading, and post-peak behavior. (Whittle, 1993; Whittle & Kavvadas, 1994). It has previously been used to predict the behavior of embankments on soft ground including an I-95 test section on Boston Blue Clay (Ladd et.al, 1994). The general form of the model requires 15 input parameters and is detailed by Whittle & Kavvadas (1994).

- K_{0NC} - coefficient of lateral pressure at rest, measured k_0 -consolidated triaxial testing
- e_0 - initial void ratio
- λ - the slope of the virgin consolidation line. Values correspond to the MCC compression index in the previous section.
- $\frac{2G}{K} = \frac{3(1-2\nu)}{(1+\nu)}$ - ratio of elastic shear modulus to bulk modulus
- κ_0 - Elastic bulk modulus estimated from shear wave cross hole testing
- ϕ'_{TC} , ϕ'_{TE} - critical state friction angles as determined previously. ϕ'_{TE} was assumed to be equal to ϕ'_{TC} in the absence of triaxial extension tests for this project

The remaining set of parameters are determined by fitting the model to the behavior from laboratory tests by parametric studies and are given in the Table 3-5.

Figure 3-9 provides a comparison between the predicted triaxial testing for the MCC and MIT-E3 models. Both models provide a reasonable representation of the measured stress-strain properties and effective stress paths. However, it is important to note that MIT-E3 describes undrained strength anisotropy and can consistently explain differences in undrained shear

strength measured in different modes of shearing (DSS vs. TC). In contrast, the MCC generates a unique undrained shear strengths for all modes of shear in 2D (plane strain) finite element models.

Test Type	Parameter / Symbol	Physical contribution/meaning	Upper IR Clay	Lower IR Clay
1-D Consolidation (Oedometer, CRS, etc.)	e_0	Void ratio at reference stress on virgin consolidation line	1.40	2.40
	λ	Compressibility of virgin normally consolidated clay	0.260	0.478
	C	Non-linear volumetric swelling behavior	10.0	10.0
	n		1.55	1.55
	h	Irrecoverable plastic strain	0.3	0.3
K ₀ -Oedometer or K ₀ -Triaxial	K _{0NC}	K ₀ for virgin normally consolidated clay	0.54	0.45
	2G/K	Ratio of elastic shear to bulk modulus (Poisson's ratio for initial unload)	0.94	0.94
Undrained Triaxial Shear Tests: OCR=1; CKoUC OCR=1; CKoUE	ϕ'_{TC}	Critical state friction angles in triaxial compression and extension (large strain failure criterion)	31.0°	37.0°
	ϕ'_{TE}		31.0°	37.0°
	c	Undrained shear strength (geometry of bounding surface)	0.95	0.95
	S _t	Amount of post-peak strain softening in undrained triaxial compression	3.0	3.0
	ω	Non-linearity at small strains in undrained shear	0.4	0.4

OCR=2, CKoUC	γ	Shear induced pore pressure for OC clay	0.5	0.5
Shear wave velocity	κ_0	Small strain compressibility at load reversal	0.003	0.004
Drained Triaxial	ψ_0	Rate of evolution of anisotropy (rotation of bounding surface)	100	100

Table 3-5. Summary of MIT-E3 Parameters

3.4.4 MSE Wall Parameters

The mechanically stabilized earth wall consisting of HDPE geogrids, aggregate, and wire baskets was modeled in PLAXIS using a simplified approach as described in the following section. The length of each geogrid was 23 feet, and with a vertical spacing of 1.5 feet along the wall. The HDPE geogrids were modeled with elasto-plastic geogrid elements in PLAXIS. Input parameters were axial stiffness per unit length, EA, and tensile capacity, N [F/L]. The axial stiffness can be determined using properties given by Tensar product specifications (at $\epsilon_a=5\%$). Similarly, the yield force was taken as the junction strength given by the supplier, as shown in Table 3-6.

Product	Elevation [ft]	Tensile Strength at $\epsilon_{5\%}$ [kip/ft]	Axial Stiffness, EA [kip/ft]	Yield Force [kip/ft]
UX1400HS	26.7 ft to 35.7 ft	2.1	42.6	4.5
UX1500HS	17.7 ft to 25.2 ft	3.6	71.2	7.2
UX1600HS	10.2 ft to 16.2 ft	4.0	79.6	9.3
UX1700HS	2.7 ft to 8.7 ft	5.1	102.8	11.0

Table 3-6. Geogrid properties used in PLAXIS (vertical spacing=1.5 ft)

As a simplifying assumption, the wire basket assembly were modeled as elastic plates in PLAXIS with axial stiffness, EA, flexural stiffness, EI. The stiffness of material was assumed to be for typical concrete and the dimensions of the assembly was assumed to be 2ft thick.

$$EA = E_b A_b = 1.03(10^6) \text{ ksf} \quad (3-12)$$

where, E_b = stiffness of wire basket assembly = $5.15(10^5)$ kip/ft
 A_b = area of wire basket per foot = 2 ft^2

$$EI = E_b I_b = 3.44(10^5) \text{ kip.ft}^2/\text{ft} \quad (3-13)$$

where, I_b – second moment of inertia per foot = 0.67 ft^4

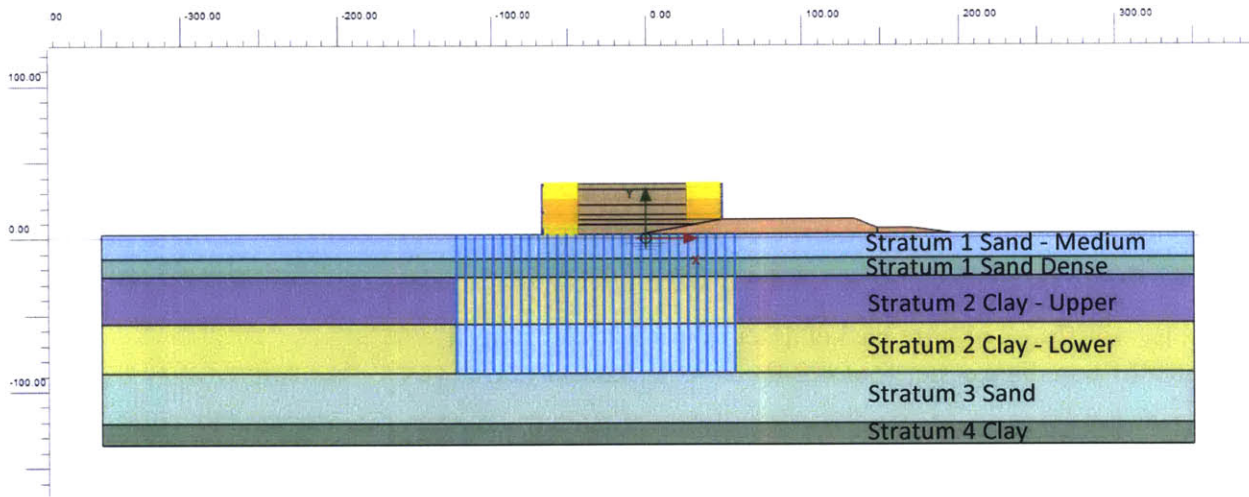


Figure 3-1. Numerical model of Sta.289+00.

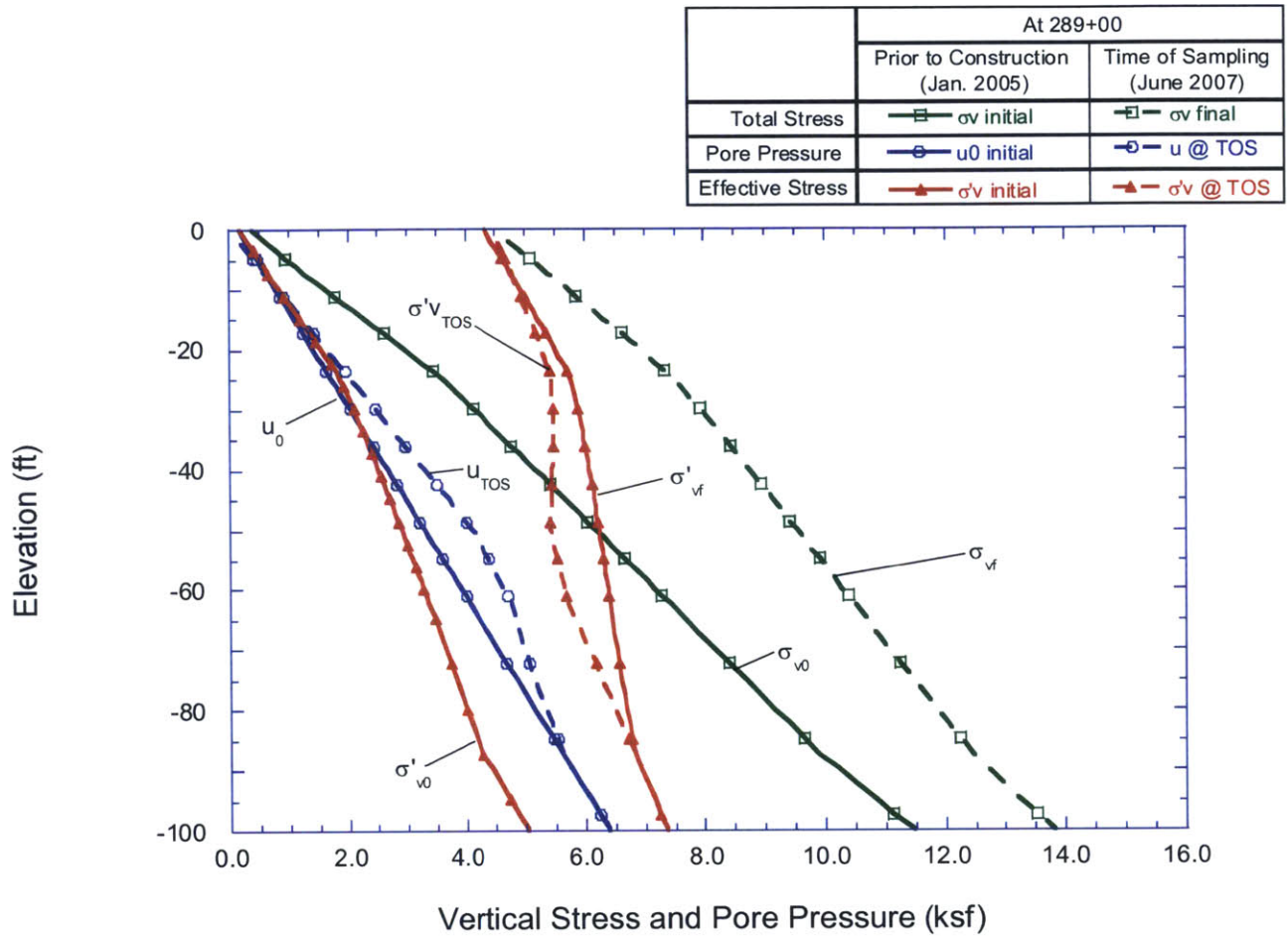


Figure 3-2. In-situ stresses below centerline of new roadway at Sta.289+00 at time of sampling (TOS) in June 2007

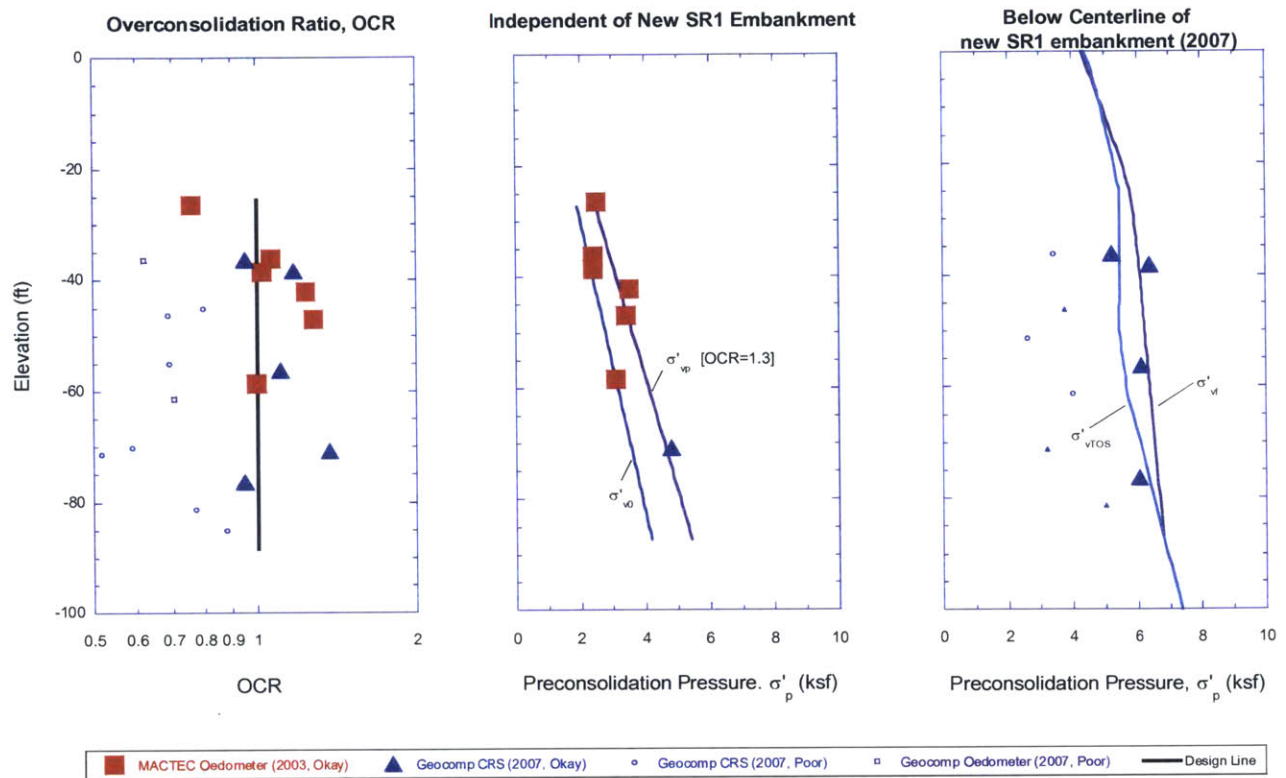


Figure 3-3. Stress history in clay at Sta.289+00.

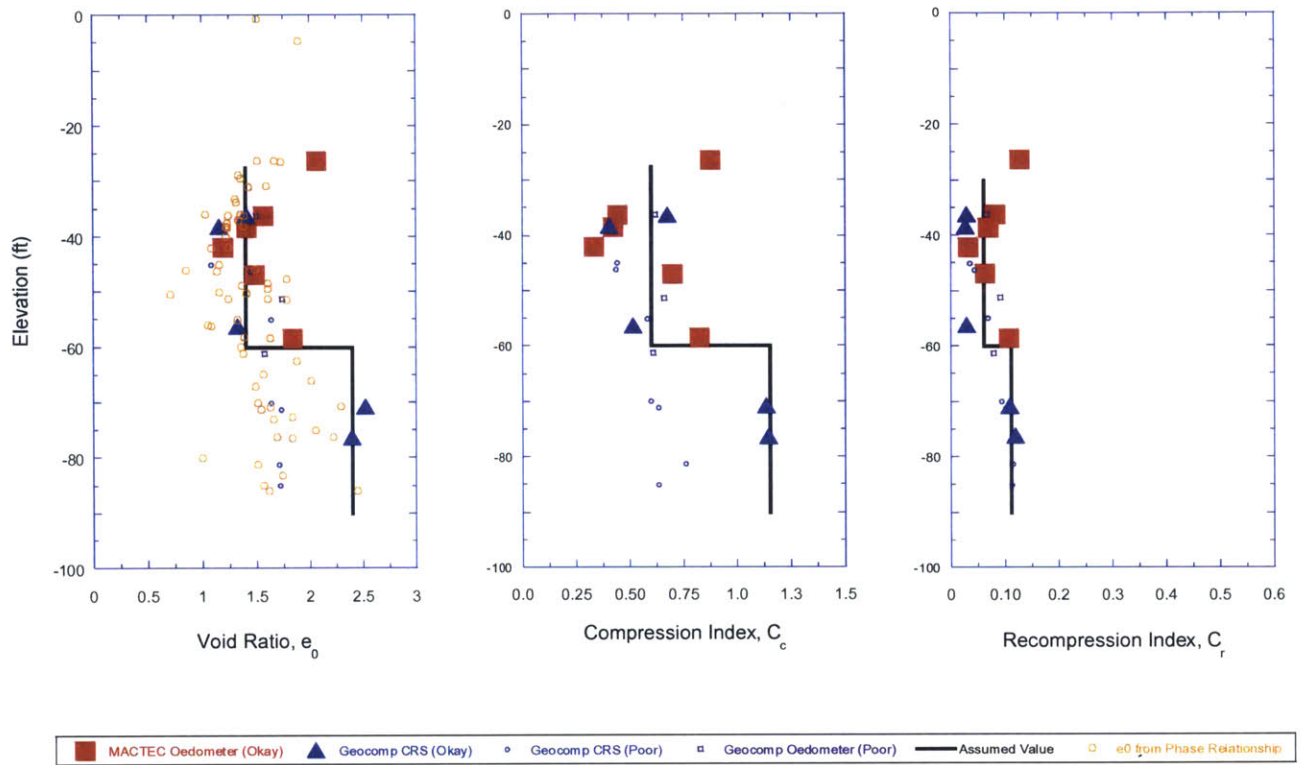


Figure 3-4. Compressibility parameters of the clay at the southern bank

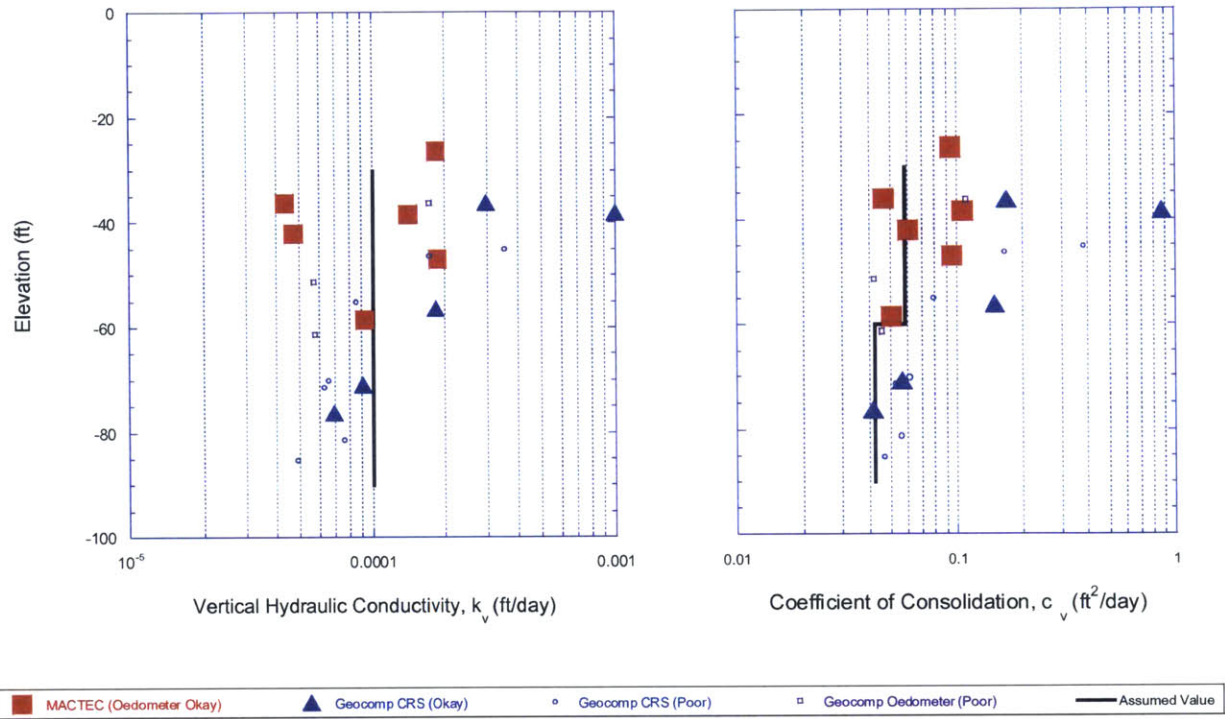


Figure 3-5. Vertical hydraulic conductivity and coefficient of consolidation based on 1-D consolidation tests at the south bank

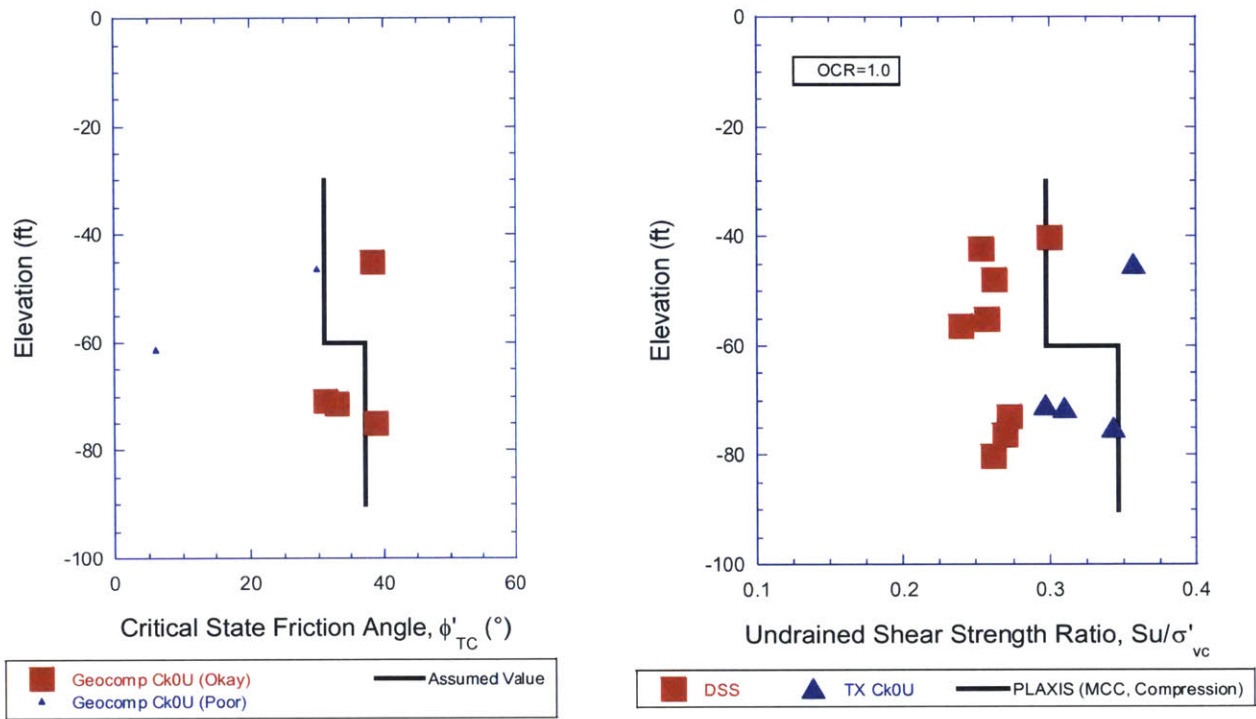


Figure 3-6. Strength parameters

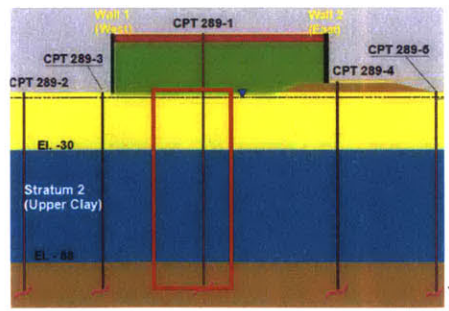
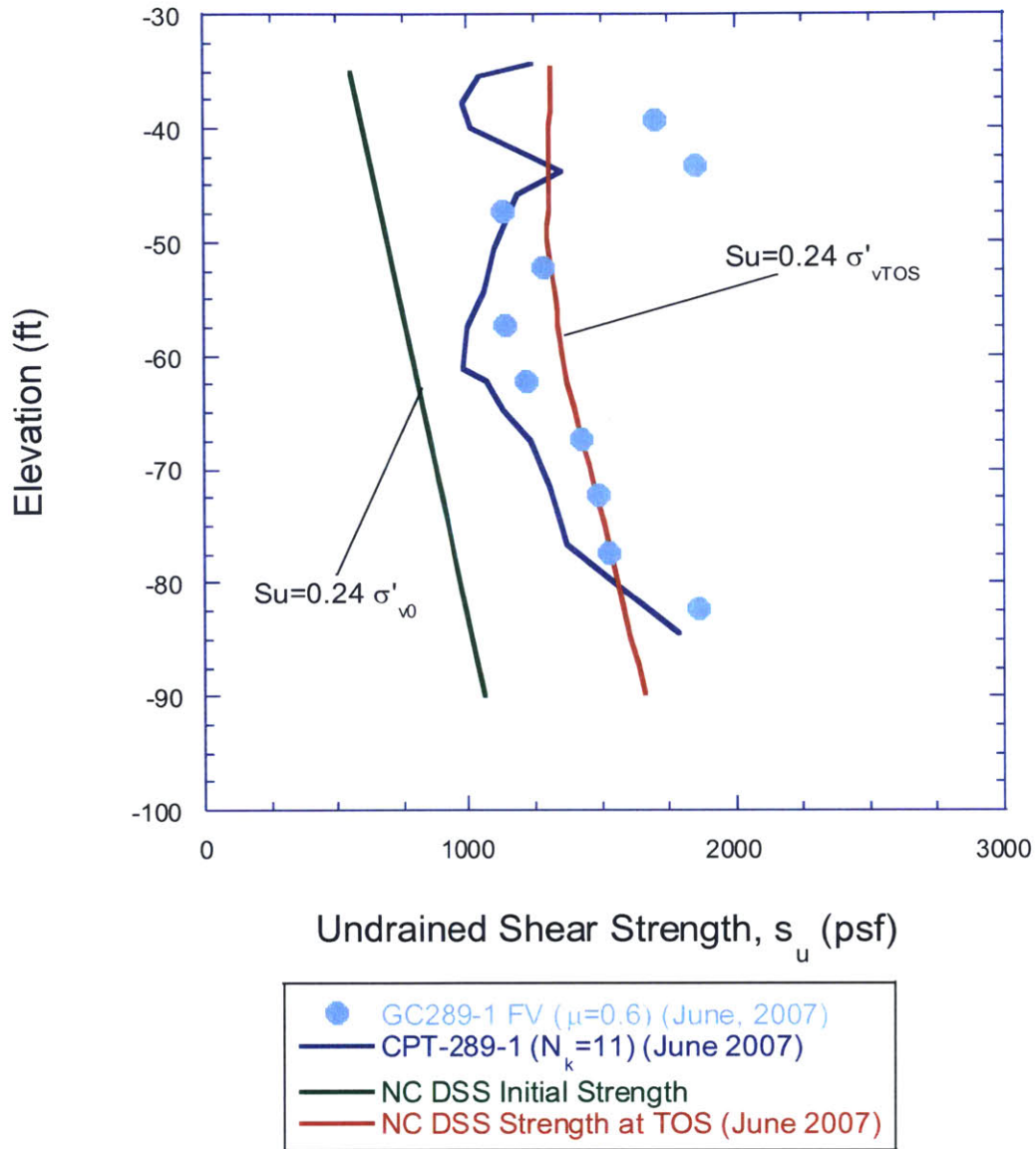


Figure 3-7. In-situ undrained shear strength below centerline of new embankment comparison between initial condition and 2007 site investigation (Geocomp, 2007)

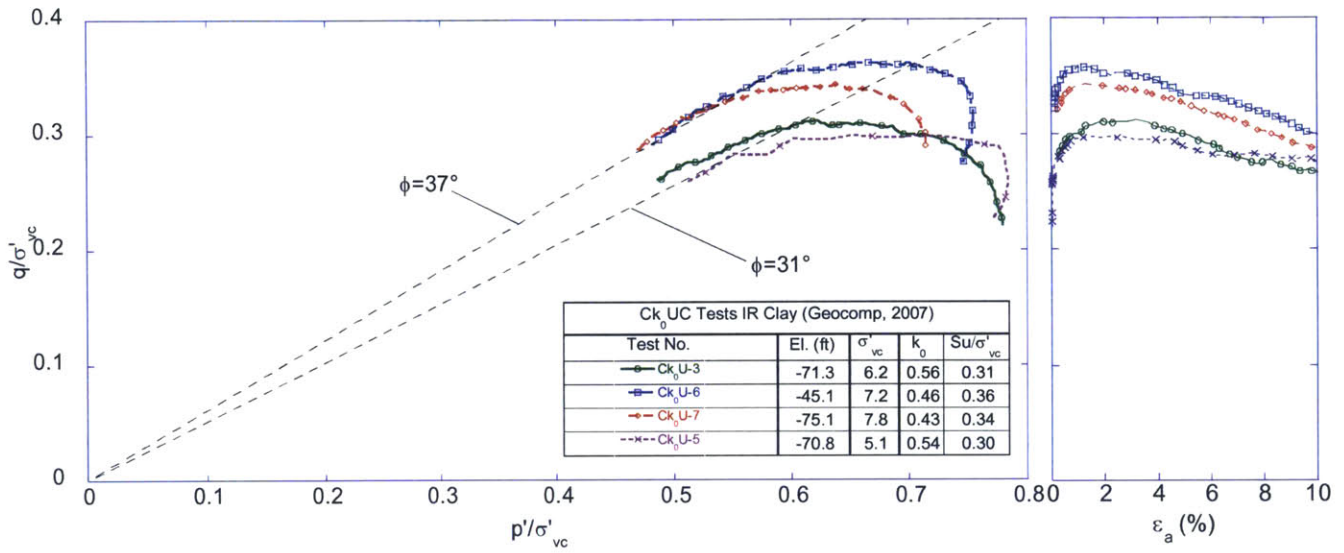


Figure 3-8. CK₀UC Triaxial Testing (Geocomp, 2007)

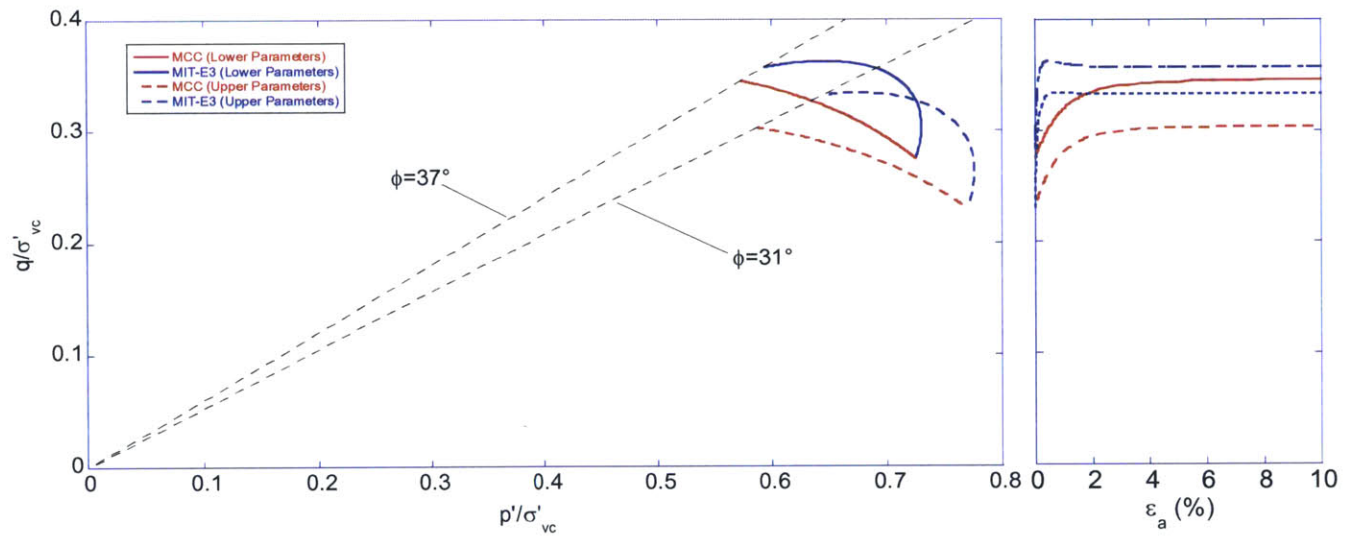


Figure 3-9. Comparison of MCC and MIT-E3 effective stress paths and shear stress-strain behavior.

4.0 FINITE ELEMENT ANALYSES OF STA.289+00

This chapter describes results of 2-D finite element analyses performed using PLAXIS-2D AE™ (Brinkgreve et al., 2014) for the southern approach embankment of the new Indian River Inlet bridge at Sta.289+00 (approximately 400 feet from the face of the abutment, Figure 2-2). The finite element models use effective stress models (MCC, MIT-E3) to describe the stress-strain strength properties of the Indian River (IR) clay. The previous chapter (Section 3-4) describes input parameters for these models based on available site investigation data (MACTEC 2003a,b; Geocomp, 2007). These analyses subdivide the IR clay into upper and lower sub-units with parameters listed in Table 3-4 and Table 3-5. A schematic of the instrumentation data used for comparison of pore pressure, settlement, and lateral movement is provided in Figure 2-7.

4.1 Base Case Analysis

Figure 4-1 shows the stress-state in the ground prior to the construction of the new approach embankment. The clay is consolidated beneath a much lower embankment (9.5 ft. above grade) of the pre-existing SR1 bridge (west of new alignment). It was initially assumed that the fill was in place for a minimum of 30 years. The analyses show that the pre-existing fill would have induced a settlement of 2.1 ft. (at $t = 30$ years) and that significant excess pore pressures would remain within the clay ($\Delta u/\Delta\sigma_v=0.39$, Figure 4-1b). These results suggest that the IR clay is under-consolidated at the time of new embankment construction (with an expectation of a further 0.5 ft. of settlement). In fact, we do not know the exact date of prior embankment construction and there is no direct evidence of on-going consolidation processes (excess pore pressure or settlements). Hence, it is reasonable to assume the full consolidation has occurred prior to new embankment construction as shown in Figure 4-1c. Consolidation beneath the new approach embankment is accelerated through an array of full depth PV drains installed in triangular array as shown in Figure 2-8. Following Hird et al. (1992), the hydraulic conductivity of the clay

within the PV drain is modified (Equation 3-9 and Section 3.3.5) to reflect intrinsic limitations in modeling radial flow with a 2-D plane strain model. Figures 4-2a-d show the ground deformations and excess pore pressures predicted at Sta.289+00 at the end of construction (EOC, November 20, 2006 at Construction Day, CD 273 and at the end of monitoring period (EOM, April 3, 2008 at CD 773). The results correspond to predictions using the MCC soil model.

1. Figures 4-2a and b show that the largest settlements occur under the western side of the approach embankment with maximum settlements at ground surface increasing from $s=3.9$ ft. at EOC (CD 273) to $s=5.8$ ft. at EOM (CD 773).
2. Figures 4-2c and d show the lateral deformations (i.e. spreading) beneath the new embankment. The largest deformations occur at the top of the clay layer beneath the western wall of the embankment and increase from $h_m=1.3$ ft. (EOC) to 1.7 ft. (EOM). Much smaller spreading occurs to the East side of the fill ($h_m=0.63$ ft. (EOC) to $h_m=0.74$ ft. (EOM, Figure 4-2c) and shows little change with subsequent construction (EOM, Figure 4-2d). The results also show clearly how the overlying sand layer acts to restrain lateral spreading in the clay.
3. The lateral spreading ratio on the West side $h_m/s=33-30\%$ (EOC and EOM, respectively). These results represent relatively high spreading ratios compared to data reported in the literature. For example, Ladd (1991) reports $h_m/s=0.1-0.3$ for embankments constructed on soft clay with PV drain arrays from a series of case studies in Figure 4-3.

Figure 4-4a and 4.4b show excess pore pressures within the clay at CD 273 and CD 773. The results highlight clearly the role of the PV drains in accelerating the construction beneath the new approach embankment. At the end of construction (EOC, CD 273) the maximum excess pore pressures within the zone of PV drains, $\Delta u \approx 2.3-2.6$ ksf (ie. $\Delta u/\Delta \sigma_v \approx 0.3$ to 0.33, with

slightly smaller excess pore pressures to the East side of the PV drains. The results at CD 773 (EOM) show very small excess pressures remaining with the PV drain arrays ($\Delta u \approx 0.6$ ksf) but significant pore pressures were developed (outside the PV drained zone) below the original SR1 embankment. Predicted excess pore pressures were approximately, $\Delta u \approx 2.6$ ksf at EOC and $\Delta u \approx 2.0$ ksf at EOM. **

Figures 4.5a, b, and c provide a more detailed view of the changes in total vertical stresses within the clay from CD 273-CD 773 (ie. EOC to EOM). The results show that radial drainage within the zone of PV drains causes stiffening of the clay adjacent to the drains and hence, produces local arching of the stresses (ie. $\Delta \sigma_v$ increases above each line of drains, Figure 4.5c). There is also a modest (but significant) reduction in vertical stress in the area adjacent to the PV drains (most notably on the East side below the SR1 abutment). These arching effects are not typically considered in simplified 1-D analyses of soil consolidation settlements, but explain why the dissipation of excess pore pressures is retarded in this region.

4.2 Effect of Soil Modeling

Figures 4-6a-d compare vertical and horizontal components of ground deformations computed at EOC and EOM conditions (CD 273 and CD 773) using the more complex MIT-E3 model to describe the behavior of the IR clay (with input parameters listed in Table 3-5). The computed patterns and locations of maximum ground deformations are very similar to results using the MCC but show some differences.

** It should be noted that due to a conflict with the installation of the wick drains over the existing SR1 embankment, the limits of the drains were only installed to 57 feet right of the center line of the new embankment, which resulted in such large pore pressures.

In all cases, the MIT-E3 model predicts slightly larger settlements than MCC. For the lateral deflections, there was slightly more movement on the west and slightly less movement on the east side of the embankment.

1. Figures 4-6a and b show that the largest settlements at ground surface increasing from $s=4.1$ ft. at EOC (CD 273) to $s=6.8$ ft. at EOM (CD 773).
2. Figures 4-7c and d show the largest lateral deformations on the west increase from $h_m=1.4$ ft. (EOC) to 2.0 ft. (EOM). On the east side of the fill $h_m=0.56$ ft. (EOC) and $h_m=0.68$ ft. (EOM).
3. The lateral spreading ratio corresponding to these values on the West Side are $h_m/s=34-29\%$ (EOC and EOM, respectively).

Figure 4-8 shows the excess porewater pressure computed by the MIT-E3 model. For both EOC and EOM, the MIT-E3 model predicts greater excess porewater pressures in the clay than the MCC model. This result is related to the greater lateral movements in the clay underneath the West edge of the embankment with the MIT-E3 model compared to the MCC model.

It is interesting to compare predictions of the undrained shear strengths for the MCC and MIT-E3 models with results from the Phase 3 site investigations (Geocomp, 2007). Geocomp performed piezocone and field vane test through the centerline of the new approach embankment at Sta.289+00 (CPT289-1 and GC289-1) in late May 2007 (i.e. CD 481). Figure 4-9 compares the interpreted undrained shear strengths with predictions using the MCC and MIT-E3 soil models. The results show that the two models compute very similar strengths in undrained triaxial compression (s_{uTC}) which are slightly higher than s_{uFV} but overestimate the piezocone

strength assuming $N_k=11$ ^{††}. The MIT-E3 soil model predicts different undrained shear strengths for different modes of shearing (due to its anisotropic formulation). Values of s_{uDSS} computed by MIT-E3 are in close agreement with the piezocone data (CPT289-1).

For normally consolidated clays, the lateral deformations are governed primarily by undrained shear behavior (Tavenas, 1979). As shown in this and the previous section, the majority of the horizontal movements occur before the end of construction. In fact, practically no horizontal movements occur after the end of construction in both models on the East side, while the rate of movement to the West decreases significantly. Due to the construction and consolidation of the previous roadway embankment, the available undrained shear strength is greater underneath the existing SR1 embankment causing less shear deformation on the East side. The MIT-E3 predicts greater increase in undrained shear strength with consolidation than the MCC model. As such, greater differential horizontal and vertical movements predicted by the MIT-E3 model is expected.

Figure 4-10 and Figure 4-11 compare the changes in total vertical stress and the ratio of excess pore pressure to total vertical stress with time for the two soil models at mid-depth of the clay to the west of the embankment and below the centerline of the roadway respectively. MIT-E3 predicts that there is a change in total vertical stress of approximately 0.9 ksf directly underneath the new embankment and a reduction to the west. While the redistribution of total vertical stress is similar between the two models in the zone of the wick drains (Figure 4-11), there is a greater stress reduction in the zone beneath the existing SR1 embankment in the MIT-E3 model. The excess pore pressure ratio in the zone of the wick drains decreases quickly as consolidation

^{††} Geocomp selected $N_k=11$ in order to match lab measurements of S_{uDSS} .

occurs. Outside of the zone of the wick drains, the ratio does not decrease below unity, indicating the excess porewater pressure is larger than the applied vertical stress.

4.3 Pore Pressure Measurements

Figures 4-12 and 4-13 compare the computed and measured excess pore pressures within the PV drained area at elevations El. -50ft. and El. -70ft., respectively. The measured data at El. -50ft. (Piezometers #6 and #8, Figure 4-21a, b) show maximum pore pressures, $\Delta u \approx 4.2\text{--}4.5\text{ksf}$ occurring in September 2006 two months before end of construction (CD 215) and abutment construction. The excess pore pressures almost fully dissipate by the EOM (CD 773). The numerical predictions generally overestimate the excess pore pressures during construction but are quite consistent with rates of dissipation after EOC (CD 273). Pore pressure data at El. -70 ft. are much less consistent as shown in Figure 4-13a and b. At Piezometer 7, measured pore pressures show hardly any increase in pressure throughout embankment construction. On the other hand, the observed pore pressures exhibit erratic behavior at piezometer 5 with hardly any dissipation with time. Discrepancies between the computed and measured behavior are likely due to small imprecision in the relative locations of the piezometers and PV drains (i.e. there are high gradients of excess pore pressure within the PV drain zone while data from the FE analyses are at the midpoint between line of drains) or measurement errors due to electrically defective equipment.

4.4 Settlement

Figures 4-14 through 4-18 compare the predictions with measured settlement plate data and prior FE analyses reported by Geocomp (2007). Table 4-1 summarizes the results at EOC (CD 273) and EOM (CD 773) conditions.

Not surprisingly, points closest to the centerline (35L, Figure 4-15 and 15L, Figure 4-16) undergo the largest settlement. The results show EOC (CD 273) settlements in the range of 47-50 in., increasing to 75-80 in. at EOM (CD 773). Immediately outside the footprint of the embankment, results for 70L (West) side show much larger settlements (35 in. at EOC to 64 in. at EOM, Figure 4-14) than those on the eastern side, 53R (18 in. at EOC to 35 in., Figure 4-17).

The numerical analyses, especially those with the MIT-E3 soil model are in excellent agreement with the measured settlement response at three of the four monitoring points and underestimate slightly (by about 9%) the data for 70L (West side, Figure 4-14). The MCC model predicts very similar magnitudes of ground settlement through the end of construction (CD 273) but smaller settlements during the subsequent consolidation phase through EOM (CD 773). Differences between the two soil models amount to 5-10 in. at the end of monitoring.

Geocomp (2007) reported similar comparisons of settlement time for plates at 70L, 15L and 53R. Their analyses also used PLAXIS 2D but were obtained with the Soft Soil Creep (SSC, Vermeer and Neher, 2000) model using a set of input parameters (calibrated from lab tests or fitted to data). The Geocomp results are in good agreement with the current analyses for the two points outside the footprint of the fill embankment (70L, and 53R, Figures 4-14 and 4-17, respectively), but predict smaller settlements beneath the fill at EOC for 15L (Figure 4-16).

Table 4-2 provides a comparison between original design predictions, Golder (2007) 1-D consolidation predictions and the MIT-E3 PLAXIS results. Comparisons were also made between the original MACTEC design (2003) and Golder assessment based on lab and field data. In general, the finite element analysis predicts greater differential settlements. The simple analysis conducted by Golder do not account for the stiffness of the embankment and treats the

embankment as a uniform load. Further, end of primary consolidation (EOP, 95% consolidation) for both MIT-E3 and MCC are significantly greater than those predicted by Golder at EOP. However, this is not an exactly commensurable comparison with respect to settlement time as they had assumed 95% consolidation occurs before the end of monitoring (CD 793). Golder had also predicted a uniform settlement of 14 inches due to creep effects to model clay settlements 30 years after EOM (CD 793).^{**}

Settlement Plate	70L	35L	15L	53R
Measured (in.)	63.6	78.1	73.2	34.8
MCC (in.)	47.9	69.6	67.6	31.0
MCC (% error)	24.7	10.9	7.7	10.9
MIT-E3 (in.)	57.7	78.7	75.6	34.8
MIT-E3 (% error)	9.3	0.8	3.3	0.0

Table 4-1 Comparison of measured and predictions at embankment deconstruction.

Settlements (in.)		West Edge (66.5)	35L	CL	East Edge (50R)
Original Design	MACTEC (2003)	26.5	-	45	-
End of Primary Consolidation	Golder (Lab Tests)^{§§}	62	72	66	51
	Golder (Field Data)	67	76	69	50
CD 773	MIT-E3	79.5	79.0	71.3	41.7
	MCC	66.9	69.6	64.2	37.7
Long Term Settlement	MIT-E3	95.4	96.7	90.4	60.8
	MCC	75.6	78.4	73.2	46.7

Table 4-2. Comparison of original predicted data, Golder 1-D consolidation analysis, current predictions and long-term consolidation settlement.

4.5 Lateral Movement

This section compares the current analyses with the inclinometer measurements. Figure 4-18 and 4-19 show the lateral movement through the depth of the foundation soils at EOC (CD 273) and EOM (CD 773) conditions for the West (75L) and East sides (55R) of the embankments, respectively. Figures 4-20 through 4-23 show the lateral deformation results at El. -32.3ft., El.

^{**} Golder use secondary compression parameter, $C_{\alpha} = 0.013$ to estimate long term settlements. They had also assumed 95% consolidation (EOP) to occur by EOM (CD 773).

^{§§} Golder used data from MACTEC (2003)

-52.3ft., and El. -72.3ft. from the 75L inclinometer, and from El. -29.2ft. from the 55R inclinometer.

There is very close agreement between the computed lateral deformations on the West side of the embankment (75L) for the MCC and MIT-E3 soil models (Figure 4-18). Both analyses show the largest lateral deflections occurring at the top of the clay, increasing from 15 in. to EOC (CD 273) to 20 in. at EOM (CD 773) conditions. The analyses are in excellent agreement with lateral deflections reported at CD 773 and highlight the key role of the sand (above El. -25.3ft) in restraining against lateral spreading.

Results of the East side (55R, Figure 4-19) show qualitatively similar behavior. Most of the lateral spreading the clay occurs during the construction phase with maximum movements at the top of the clay. There is minimal lateral spreading on the East side. This result reflects the important role of the PV drains in stiffening the clay (Figures 4-5, 4-8, 4-10, and 4-11). The results for the MCC model show slightly larger lateral spreading (1.5-2 in.) in the clay than MIT-E3 and are in excellent agreement with the data reported at EOM (CD 773) conditions. Again, the overlying sand and original SR1 fill provide a major restraint against lateral spreading.

Table 2-3 summarizes the integrated lateral spread corresponding to the total volume of clay layer displaced on either side of the embankment. As can be seen in Figures 4-18 and 4-19, the majority of the lateral deformation occurs before the embankment construction. Therefore, this result is related to the undrained shear deformations within the clay. The measured data show spreads of $68\text{ft}^3/\text{ft}$ on the West and $23\text{ft}^3/\text{ft}$ and East side respectively. The MIT-E3 model slightly under predicts the total deformation by $4.5\text{ft}^3/\text{ft}$, while the MCC model over predicts the

total deformation by 1.2 ft³/ft. However, the MIT-E3 model more accurately reflects the differential deformation observed in the field. These results are summarized in Table 4-3.

Our analyses are generally in good agreement with the measured lateral deformation time response reported at selected elevations in the clay (Figure 4-20 to Figures 4-23). However, it should be noted that the lateral spread is sensitive to both the excess pore pressure buildup as well as the stiffness parameters in the upper sand layers. Given our limited knowledge of clay permeability and sand stiffness, it is surprising to achieve realistic predictions for the lateral deflections.

In contrast, the analysis by Geocomp (2007) significantly overestimate the measured lateral deflection using the Soft-Soil-Creep model. The discrepancy is most probably caused by the assumed input values of the creep parameters in the SSC model. It is difficult to estimate reliable creep parameters based on the available data and, hence, our current analyses do not include creep.

Integrated Lateral Spread (ft³/ft)	Inclinometer Data	Numerical Analyses	
		MIT-E3	MCC
75L (W)	68	65.7	63.7
55R (E)	23	20.8	28.5
Total Deformation	91	86.5	92.2
EW-Differential Deformation	45	44.9	35.2

Table 4-3. Total lateral spread at end of monitoring, CD773

4.6 Wall Tilt

Horizontal wall target data was compared with the results from the PLAXIS analysis and used to estimate the tilt of the mechanically stabilized earth walls. As surveying began at different times on the project as the wall was constructed, the measurements were base-lined for October 20, 2006 (CD 242) for the West wall (MSE Wall 1) and October 14, 2006 (CD 236) for the East wall

(MSE Wall 2). Two wall targets were available on Wall 1 and three wall targets were available on Wall 2 at Sta.289+00.

The horizontal (East-West) measurements were compared with the analysis results by resetting displacements to zero on the baseline dates. Figure 4-24 and Figure 4-25 compare the computed and measured wall movements versus time. The results of the finite element analyses generally underestimate the measured westward horizontal movement of the West wall (by up to 3.5 in. at the top of the wall, El. +28.5ft., Figure 4-24). The analyses are in much closer agreement for the East wall showing a net westward movement at all three elevations (Figure 4-25). Figure 4-26 shows the deformed mesh from the analyses from which these results were obtained. It is important to emphasize that the deformation mode of the embankment is correctly captured but that wall movements are sensitive to the stiffness of the geosynthetic grid and these were modelled using a simplified approach. Table 4-4 summarizes the observed and predicted deflections and rigid body wall tilt at EOM (CD 773) conditions. Finally, Figures 4-27 and 4-28 compare the traces of the wall tilt for the West and East walls. These results highlight the under-prediction of the West wall tilt and much closer agreement for the East wall.

MSE Wall 1 Horizontal Movement			MSE Wall 2 Horizontal Movement		
Target	Measured	MIT-E3	Target	Measured	MIT-E3
1-26 (12ft) [in.]	-7.2	-6.1	2-20 (17ft) [in.]	-9.2	-6.6
1-73 (28.5ft) [in]	-11.5	-8.0	2-21 (21.5ft) [in.]	-10.1	-7.1
	-	-	2-43 (26ft) [in.]	-10.8	-7.7
Slope (%)	-2.0	-1.0	Slope (%)	-1.4	-1.0

Table 4-4. Wall target predicted and observed comparison. Positive movement towards East.

4.7 Summary of Movement

Figure 4-29 summarizes the predicted ground deformations at ground surface and at 75L and 55R. The majority of movement after EOC (CD 273) occurs as vertical consolidation settlement. Practically no horizontal movement occurs on the East side and the rate of lateral movement on

the West is significantly slower after this point. Further, the ground settlement profile clearly illustrates the East-West differential settlements. Differences in drainage condition and effective vertical stress causes the differential settlement and apparent westward rotation of the MSE walls.

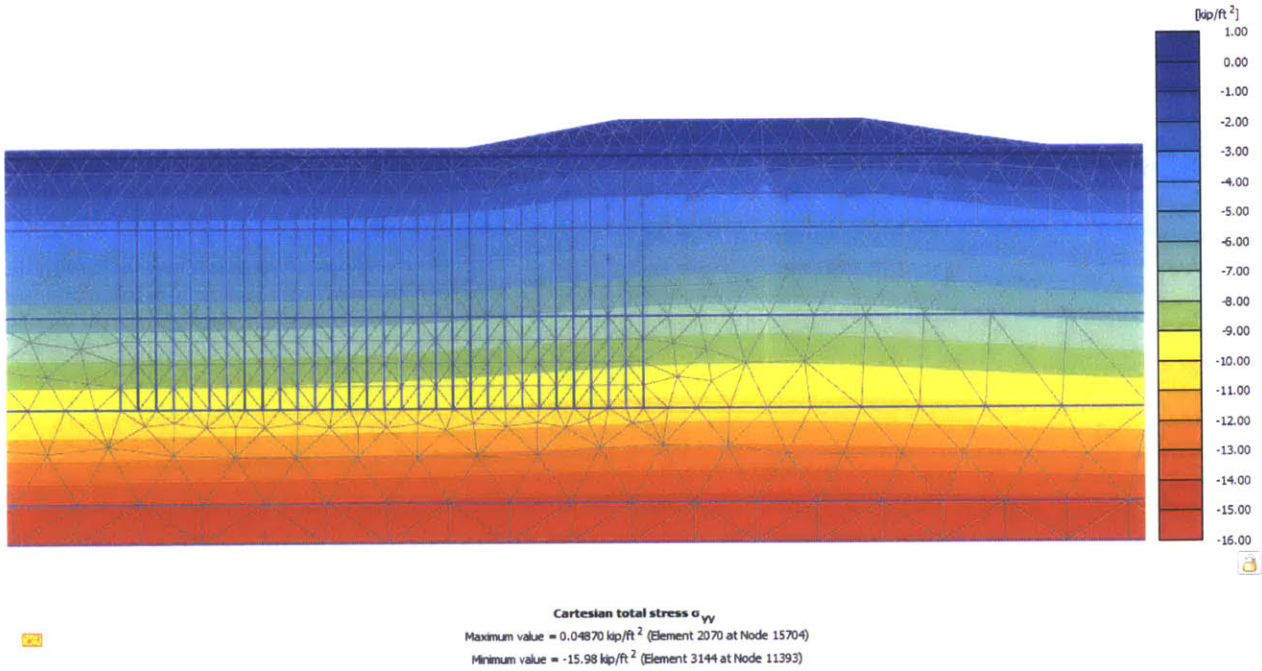


Figure 4-1a. Total vertical stresses prior to new embankment construction

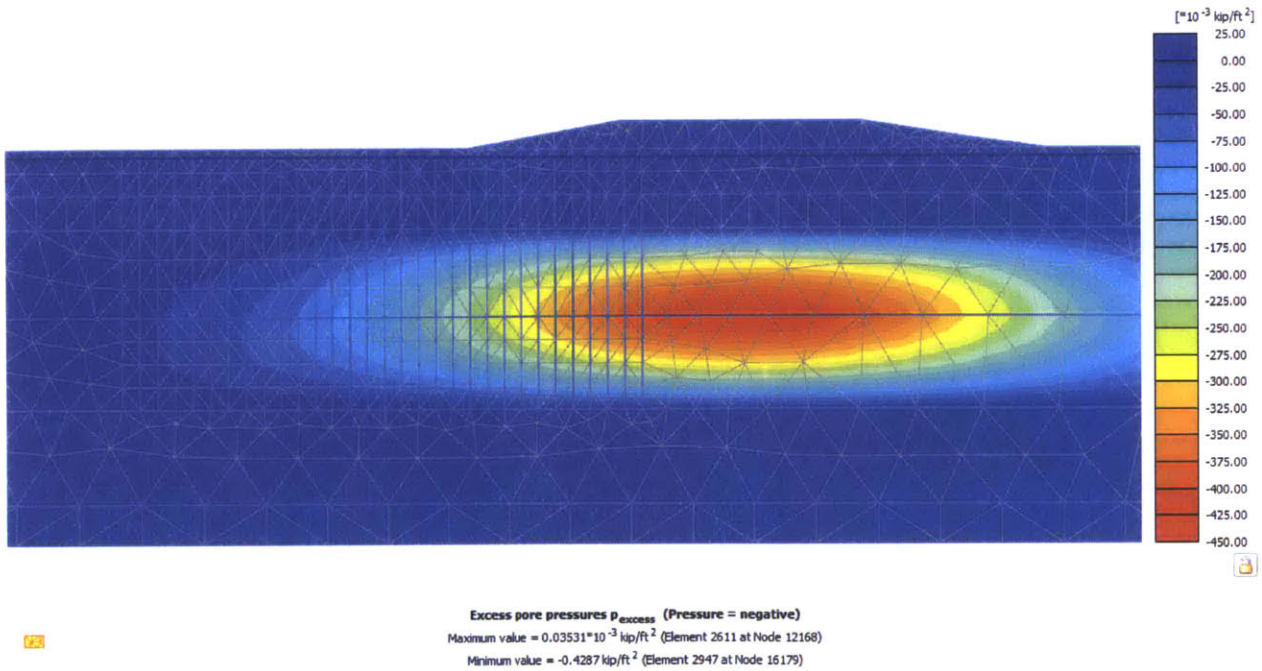


Figure 4-1b. Excess porewater pressure with $t=30$ years of consolidation of existing embankment

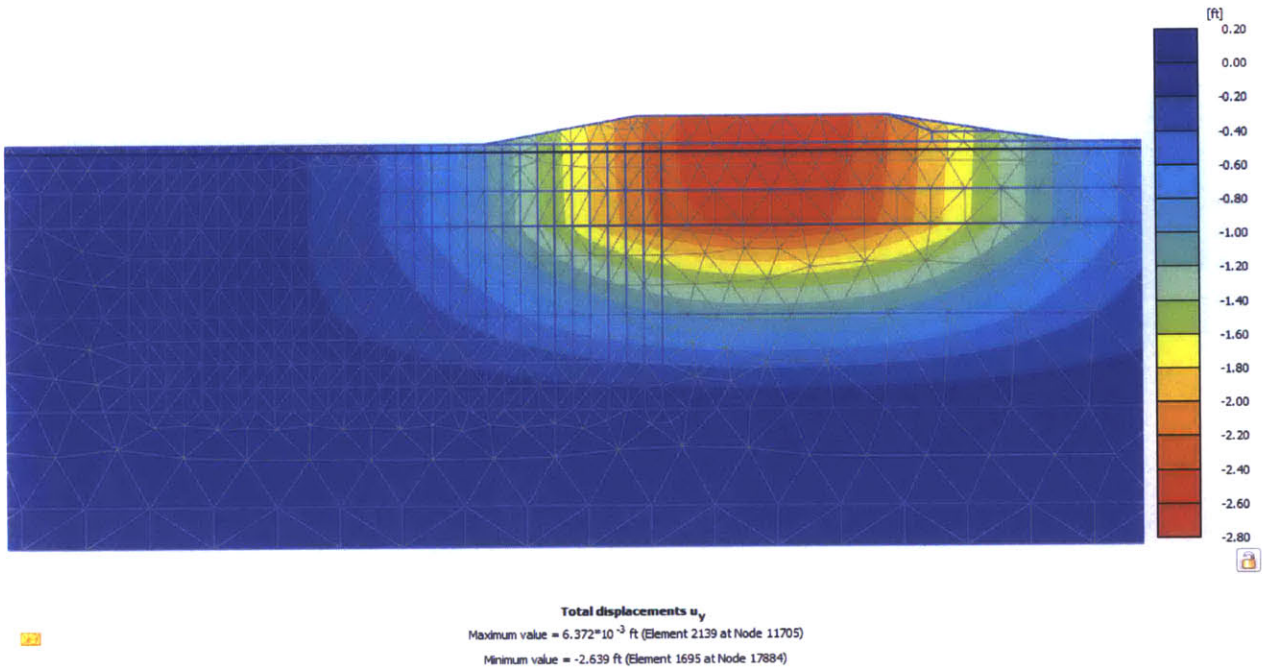


Figure 4-1c. Expected settlement beneath existing embankment assuming full consolidation.

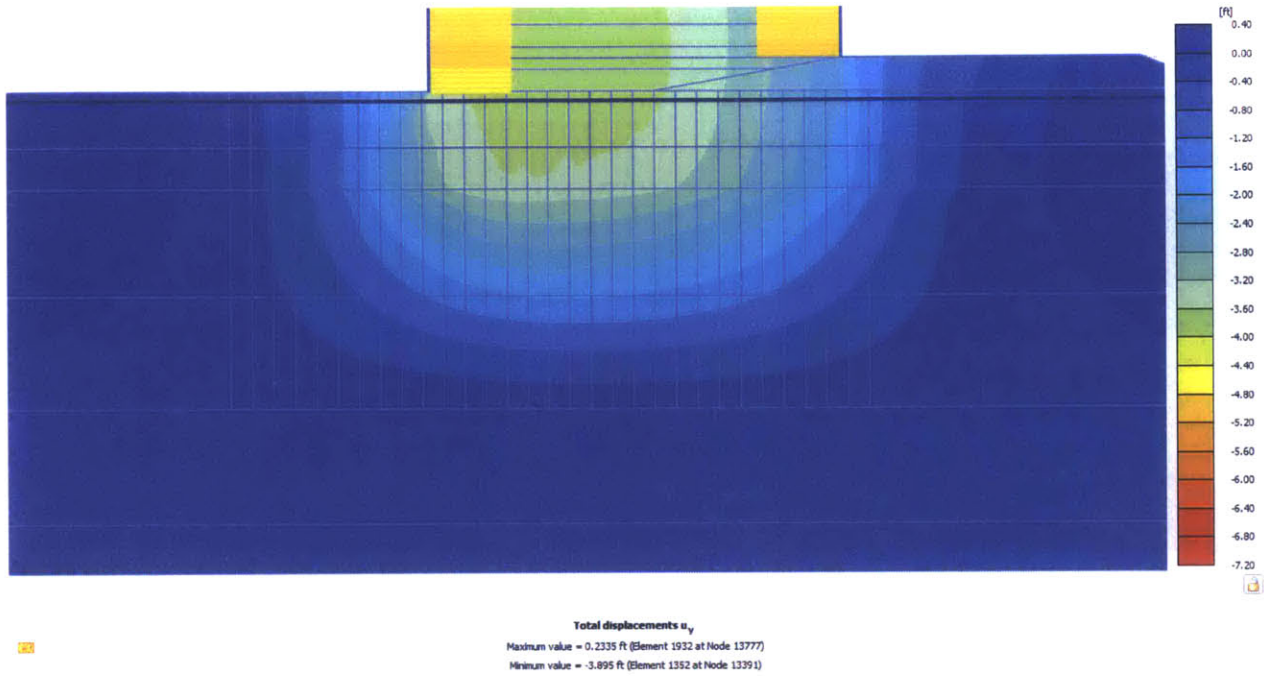


Figure 4-2a. Vertical settlements at EOC (CD 273) for base case MCC analysis.

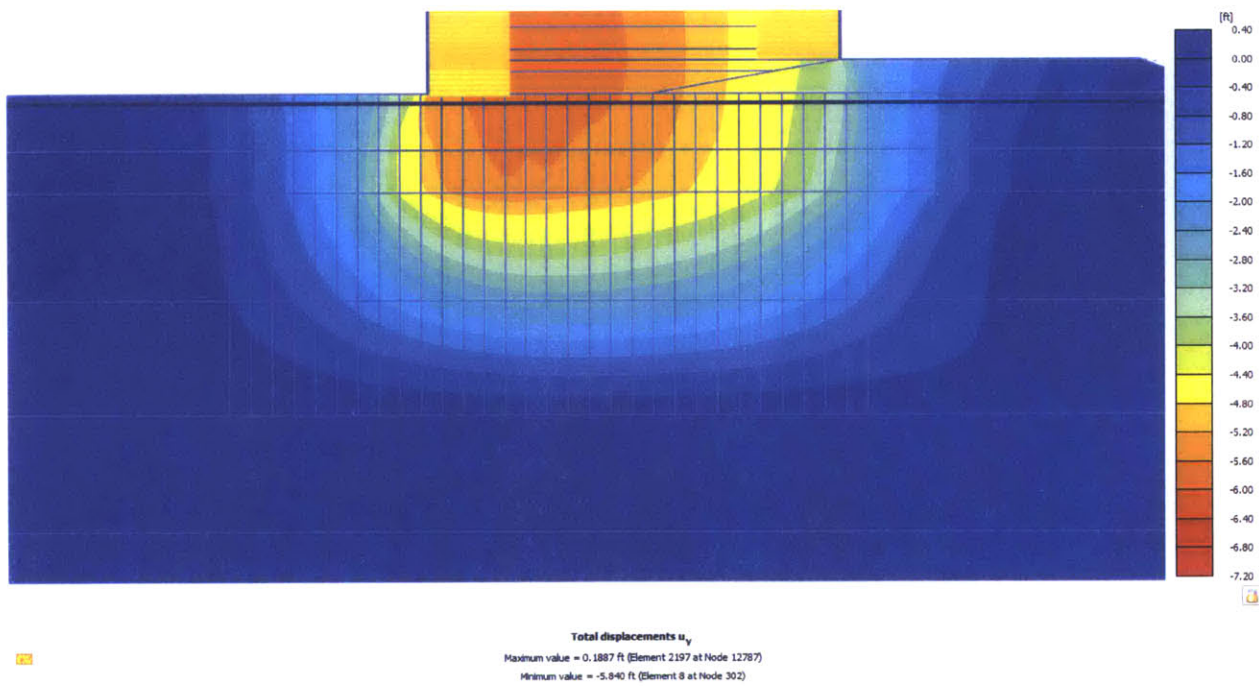


Figure 4-2b. Vertical settlements at EOM (CD 773) for base case MCC analysis.

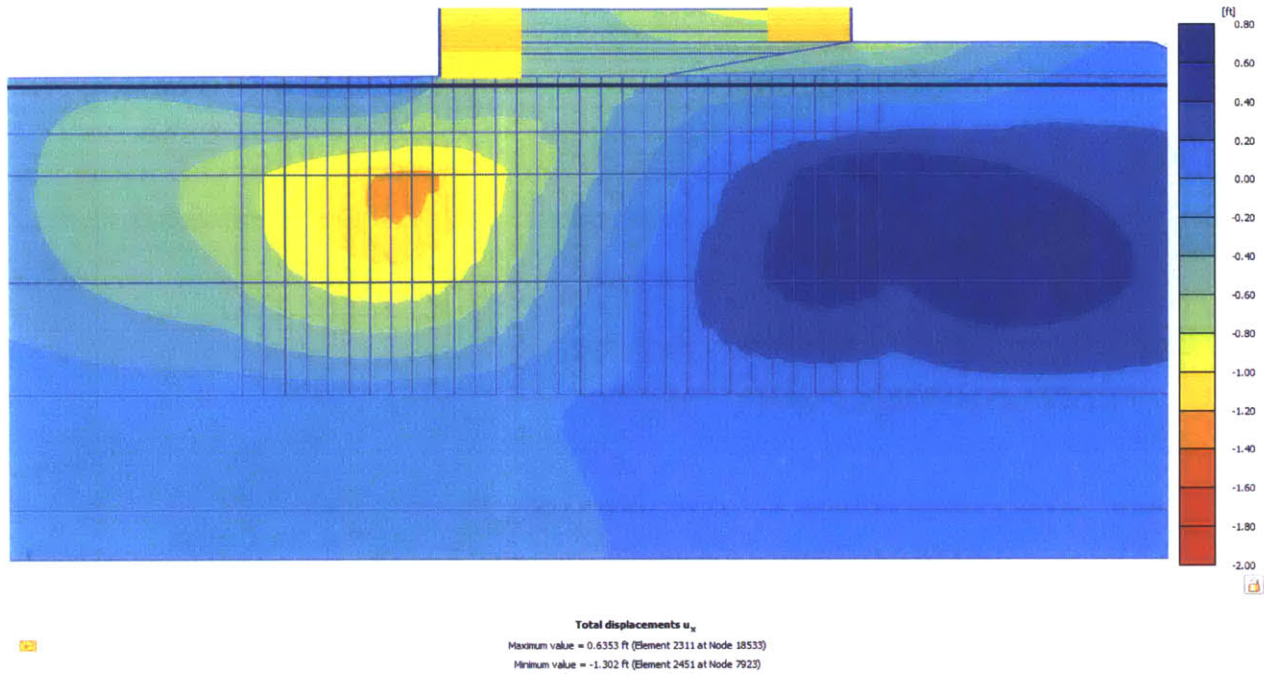


Figure 4-2c. Horizontal movements at EOC (CD 273) for base case MCC analysis.

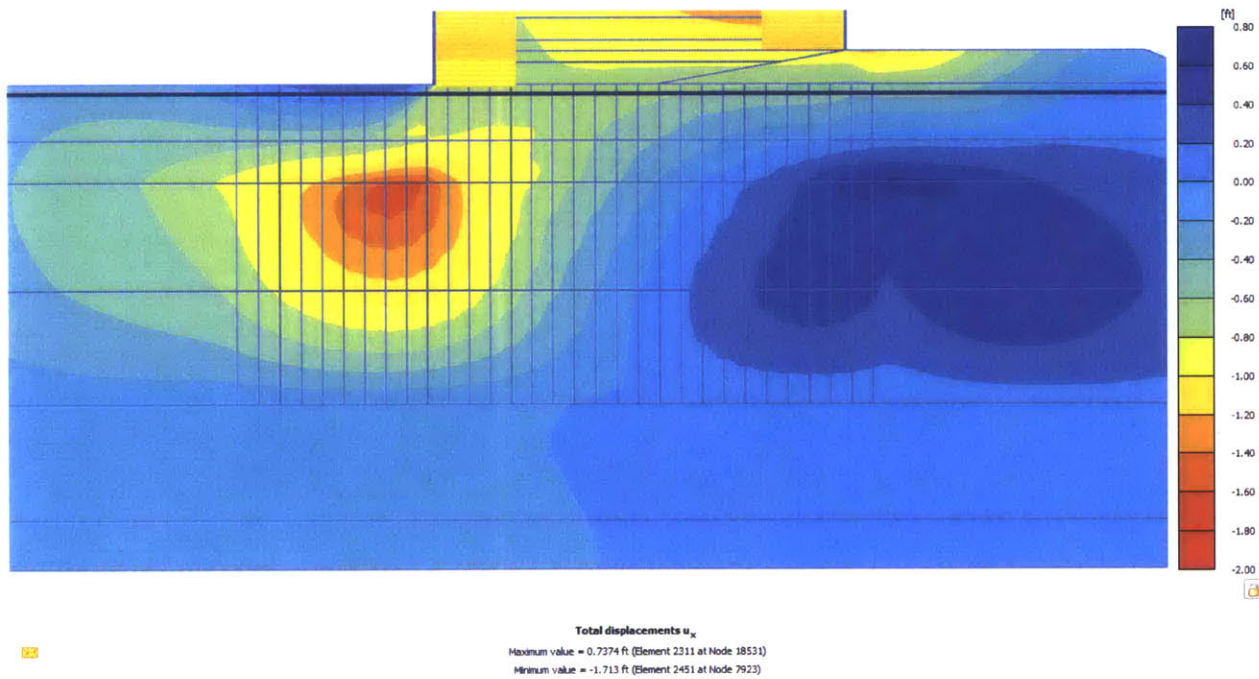


Figure 4-2d. Horizontal movements at EOM (CD 773) for base case MCC analysis.

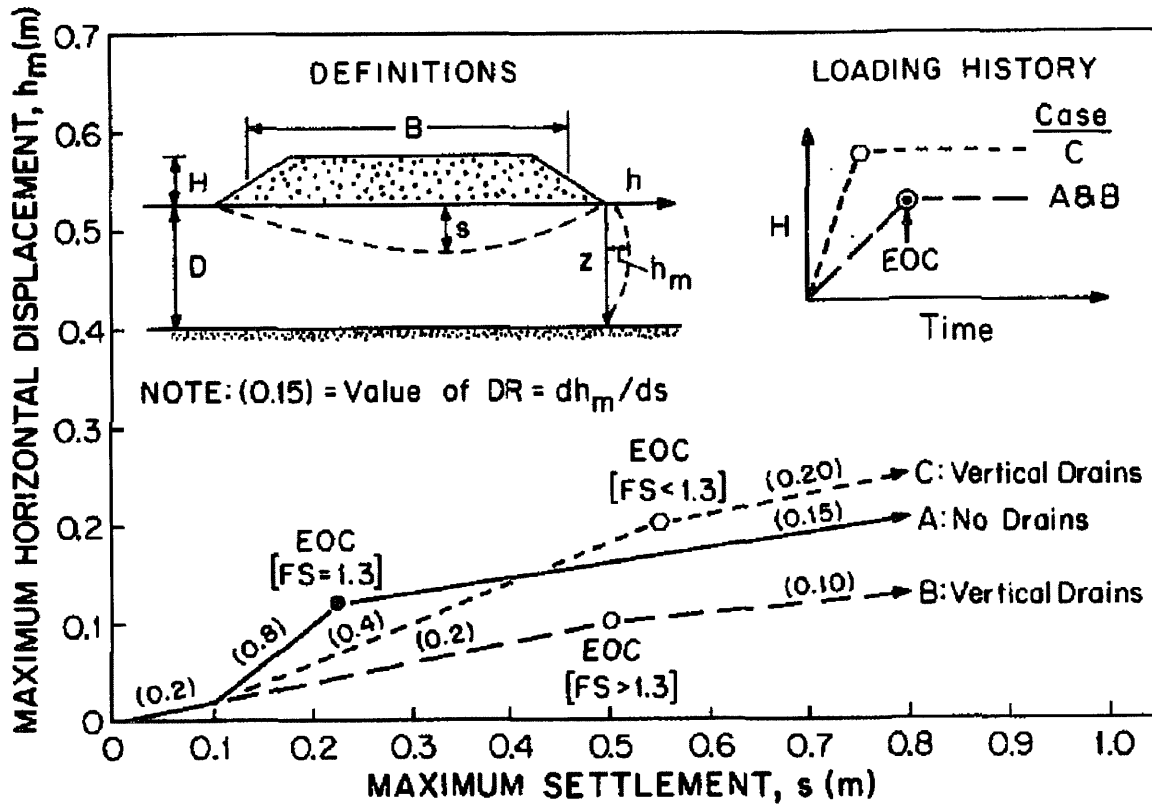


Figure 4-3. Schematic relationship between maximum horizontal displacement and maximum settlement for a staged embankment construction (Ladd, 1991).

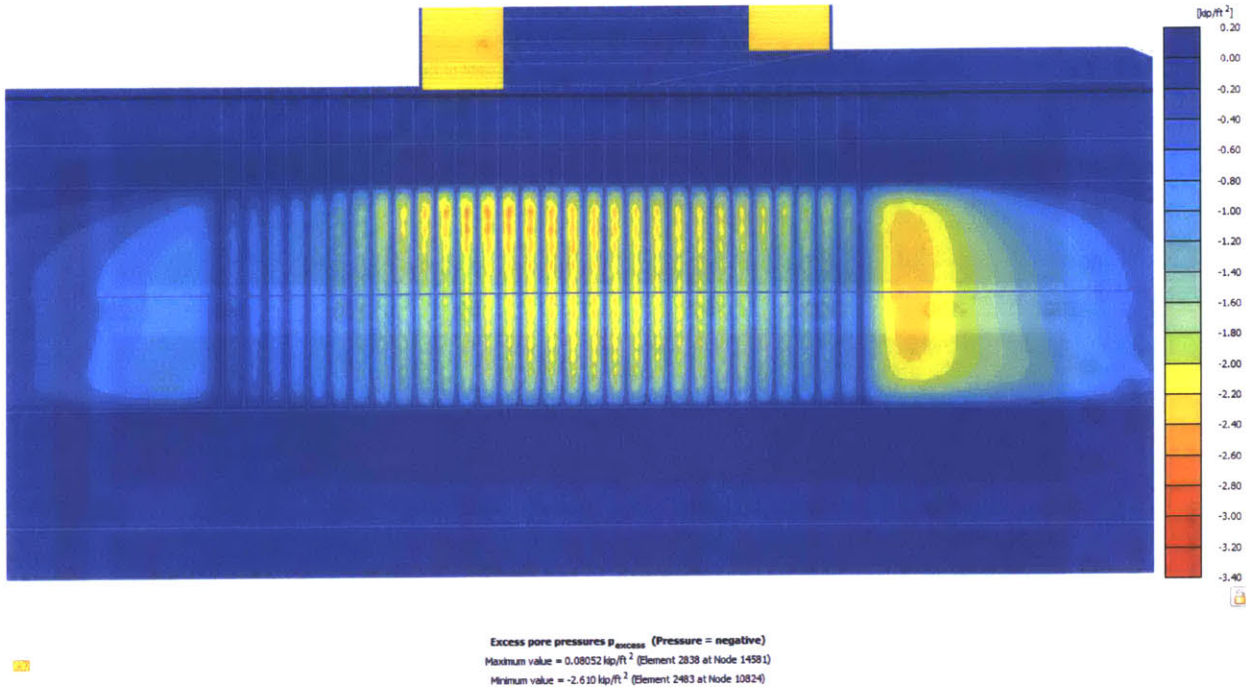


Figure 4-4a. Excess pore pressure at EOC (CD 273) for base case MCC analysis

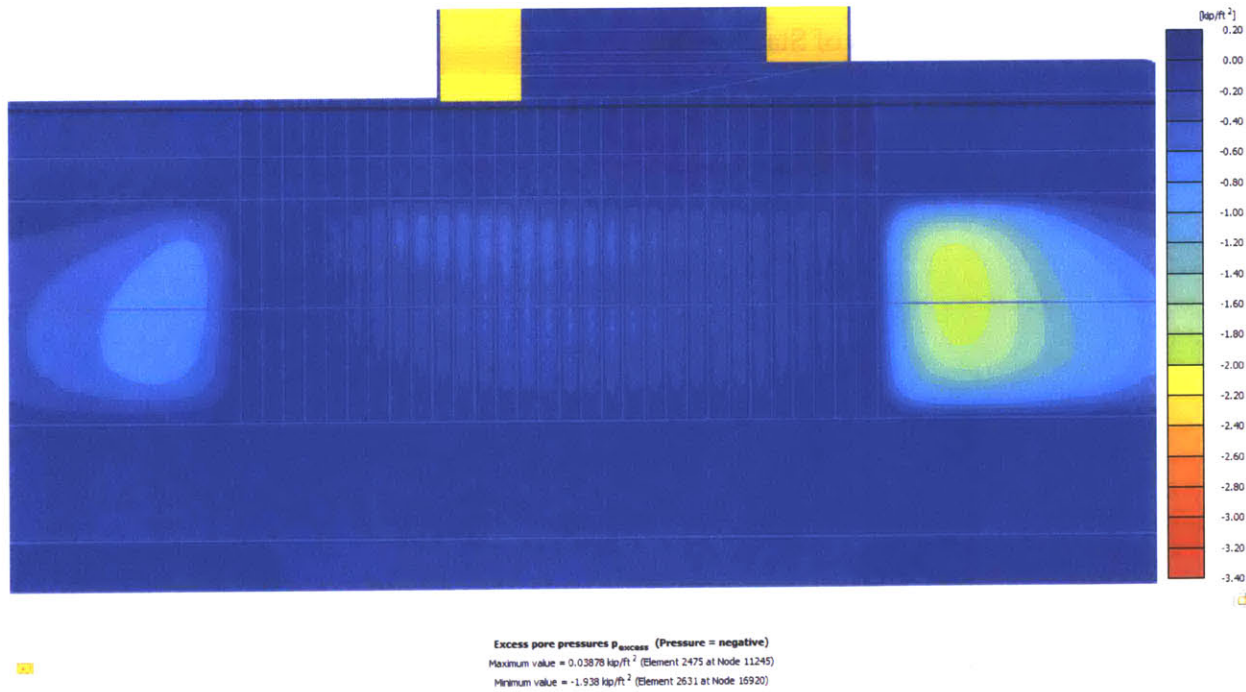


Figure 4-4b. Excess pore pressure at EOM (CD 773) for base case MCC analysis.

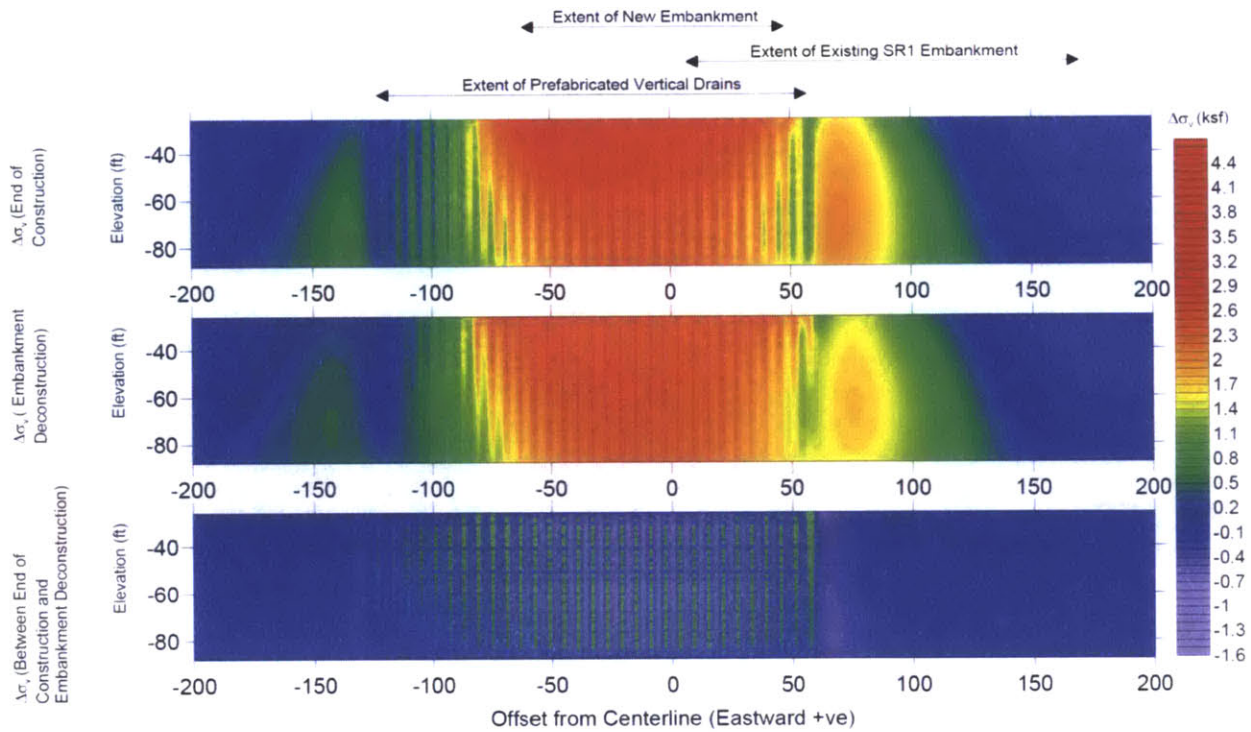


Figure 4-5. Change in total vertical stress as a result of embankment construction predicted with the MCC model at cross section of Sta.289+00.

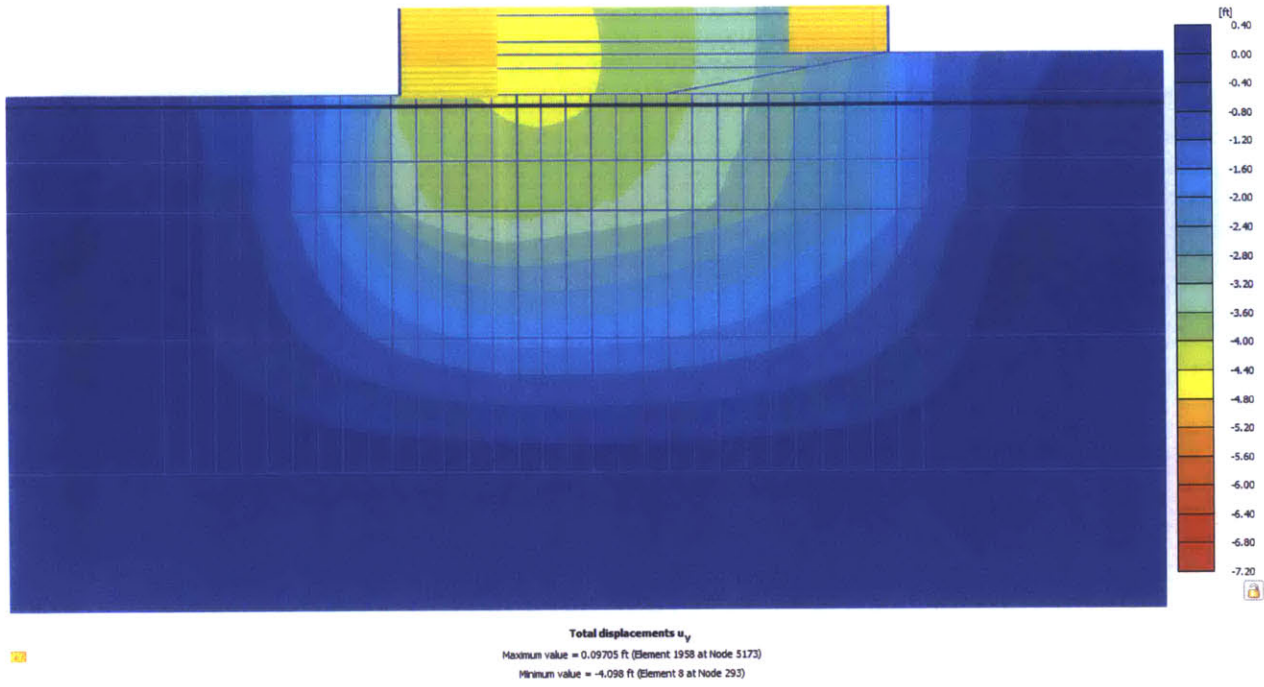


Figure 4-6a. Vertical settlements at EOC (CD 273) with MIT-E3 analysis.

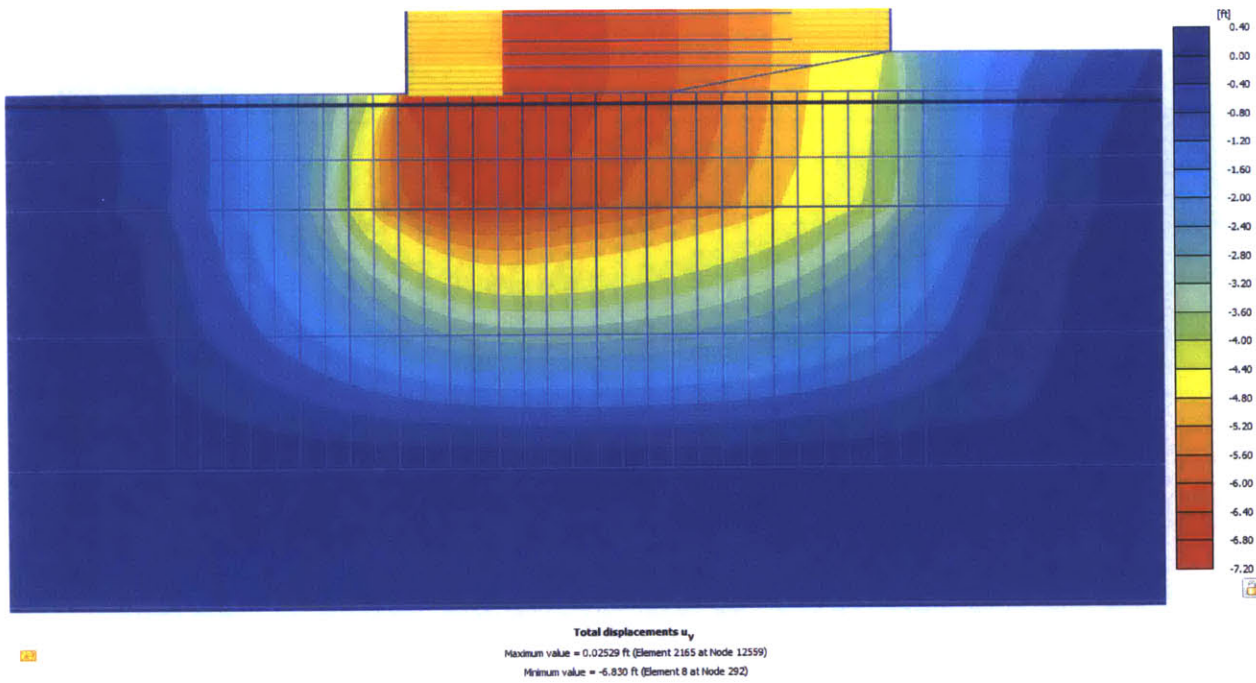


Figure 4-6b. Vertical settlements at EOM (CD 773) with MIT-E3 analysis.

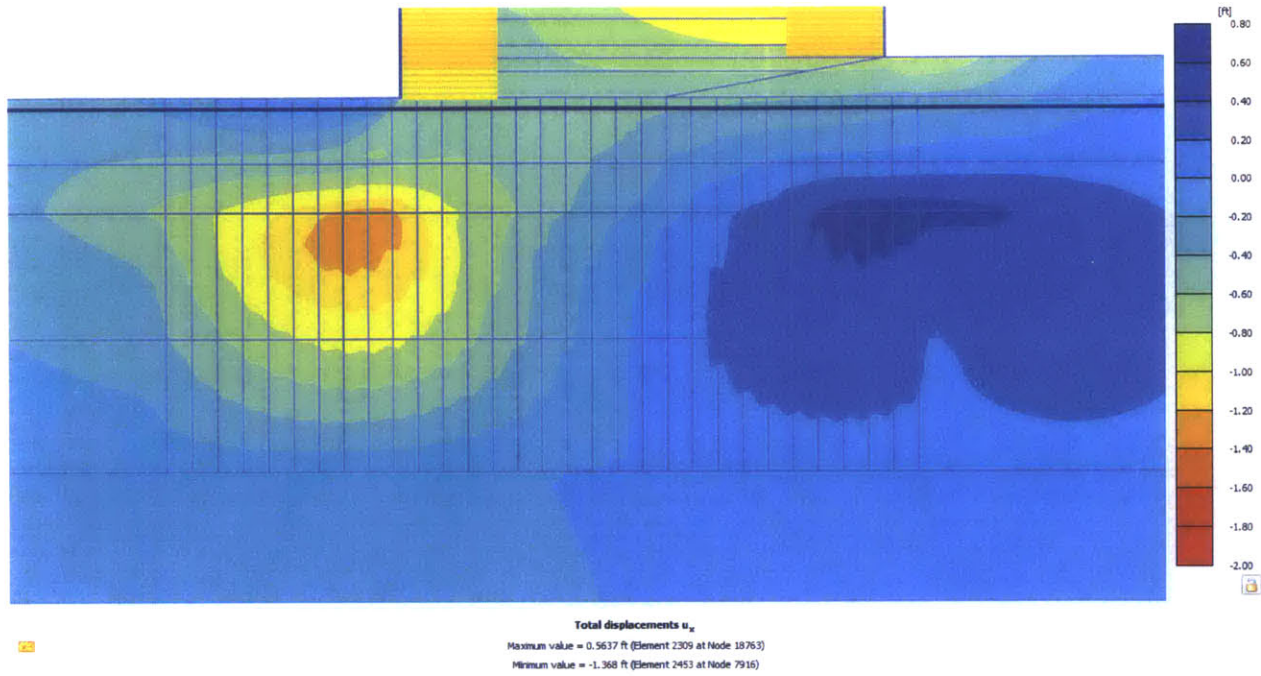


Figure 4-6c. Horizontal movement at EOC (CD 273) with MIT-E3 analysis.

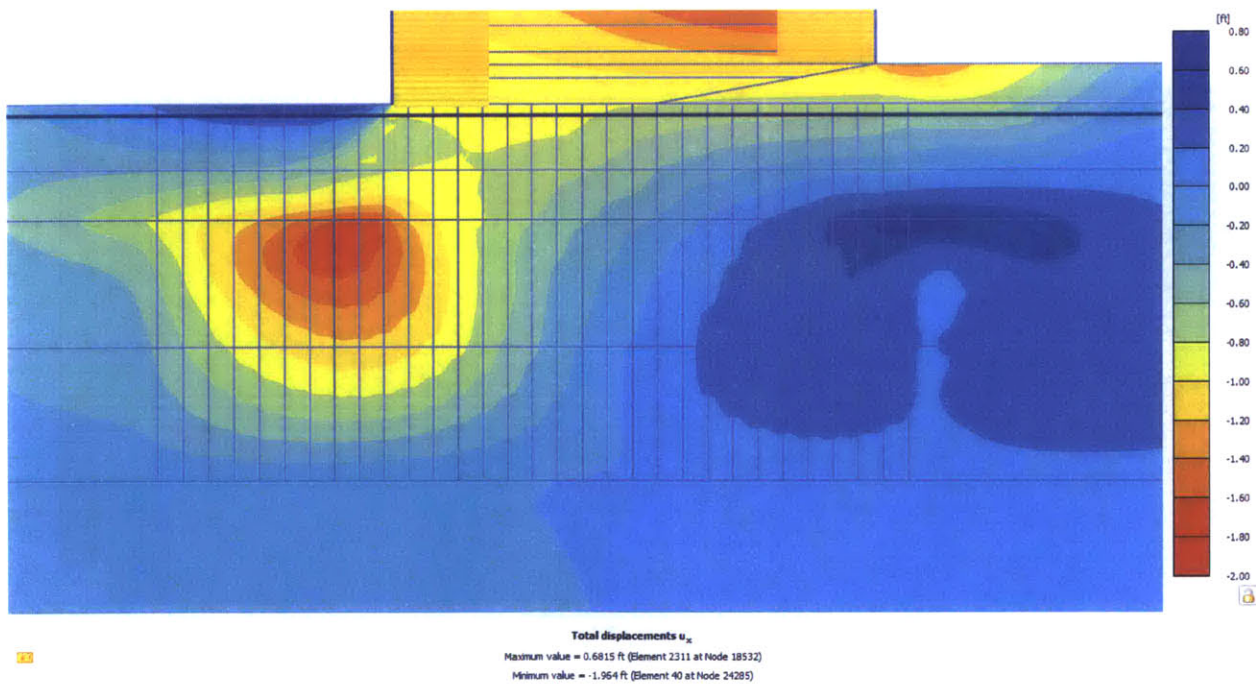


Figure 4-6d. Horizontal movement at EOM (CD 773) with MIT-E3 analysis.

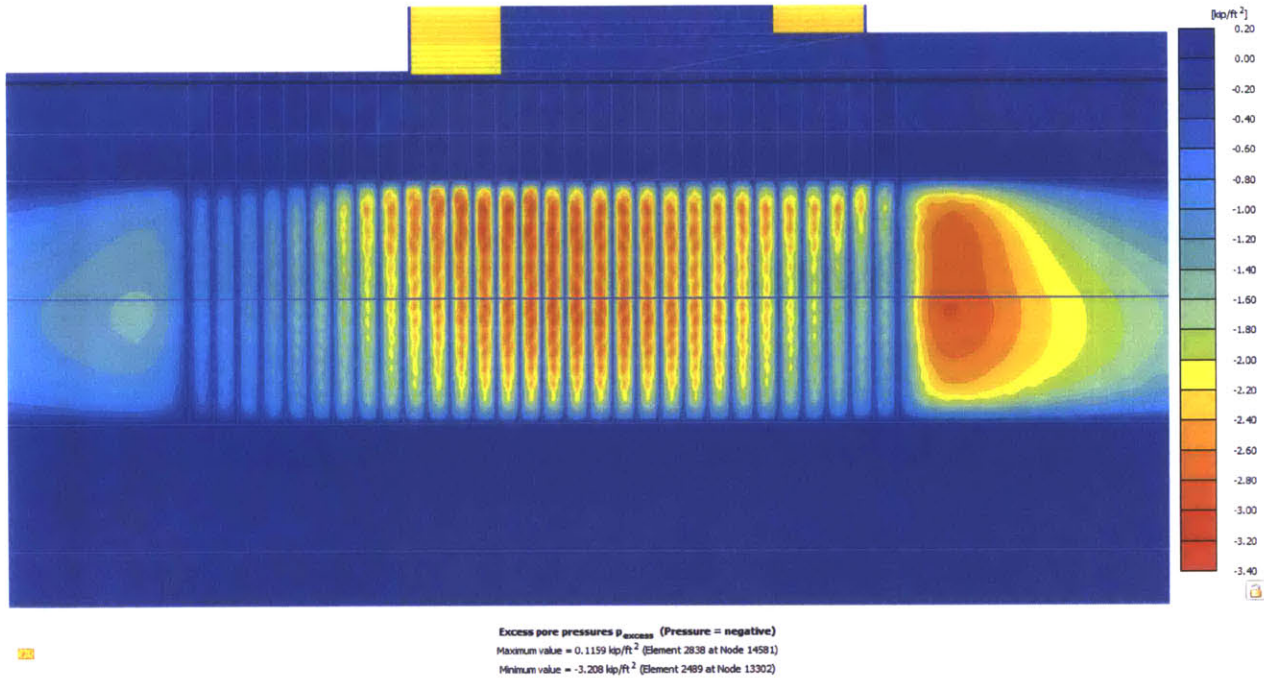


Figure 4-7a. Excess pore pressure at EOC (CD 273) with MIT-E3 analysis.

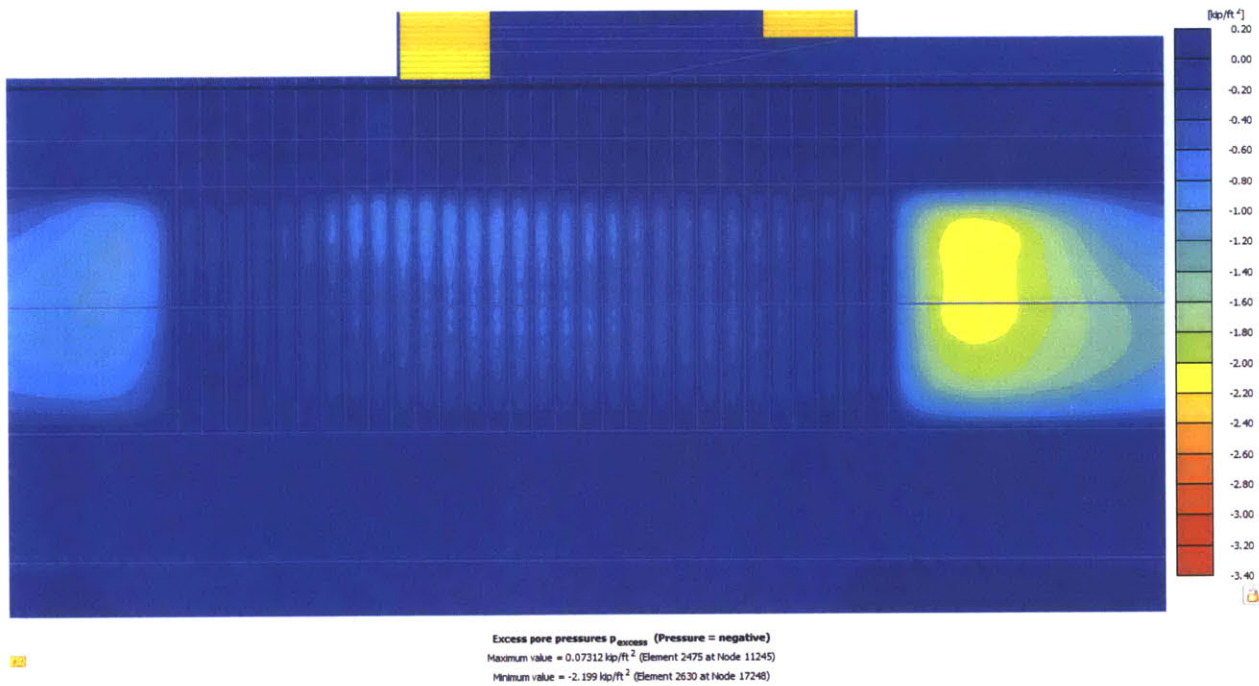


Figure 4-7b. Excess pore pressure at EOM (CD 773) with MIT-E3 analysis.

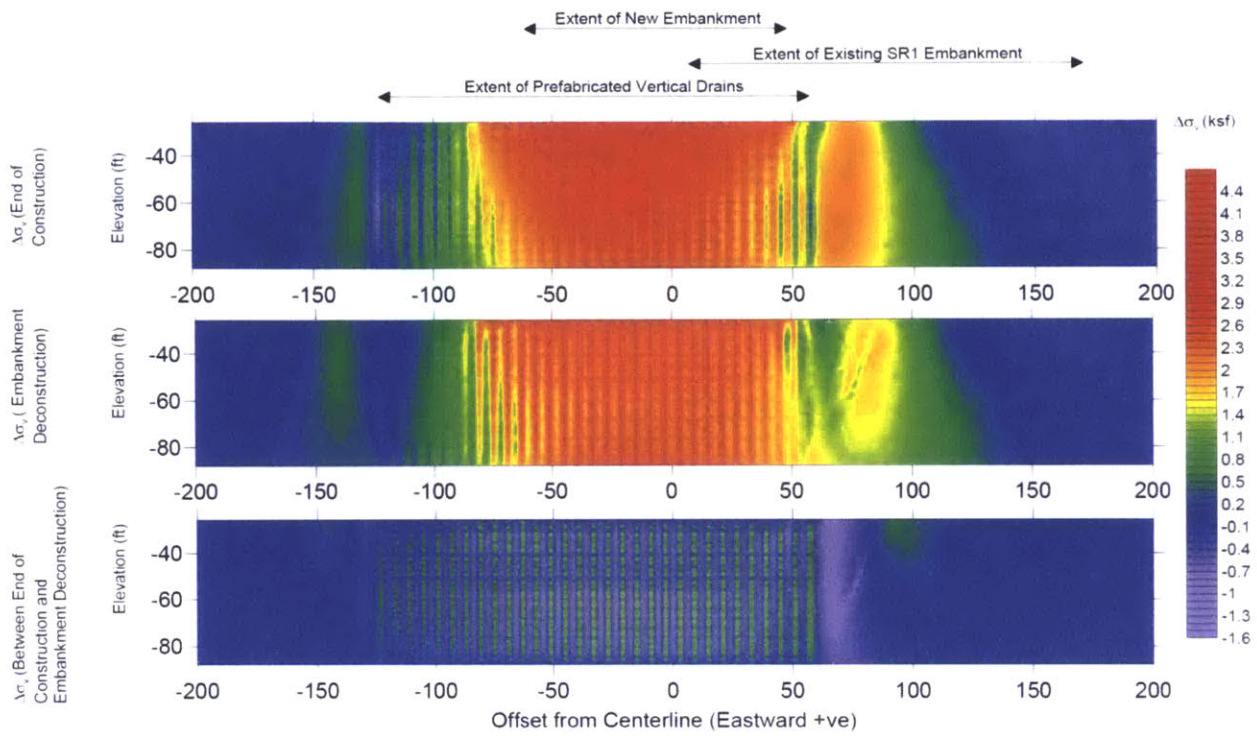


Figure 4-8. Change in total vertical stress as a result of embankment construction predicted with the MIT-E3 model at cross section of Sta.289+00.

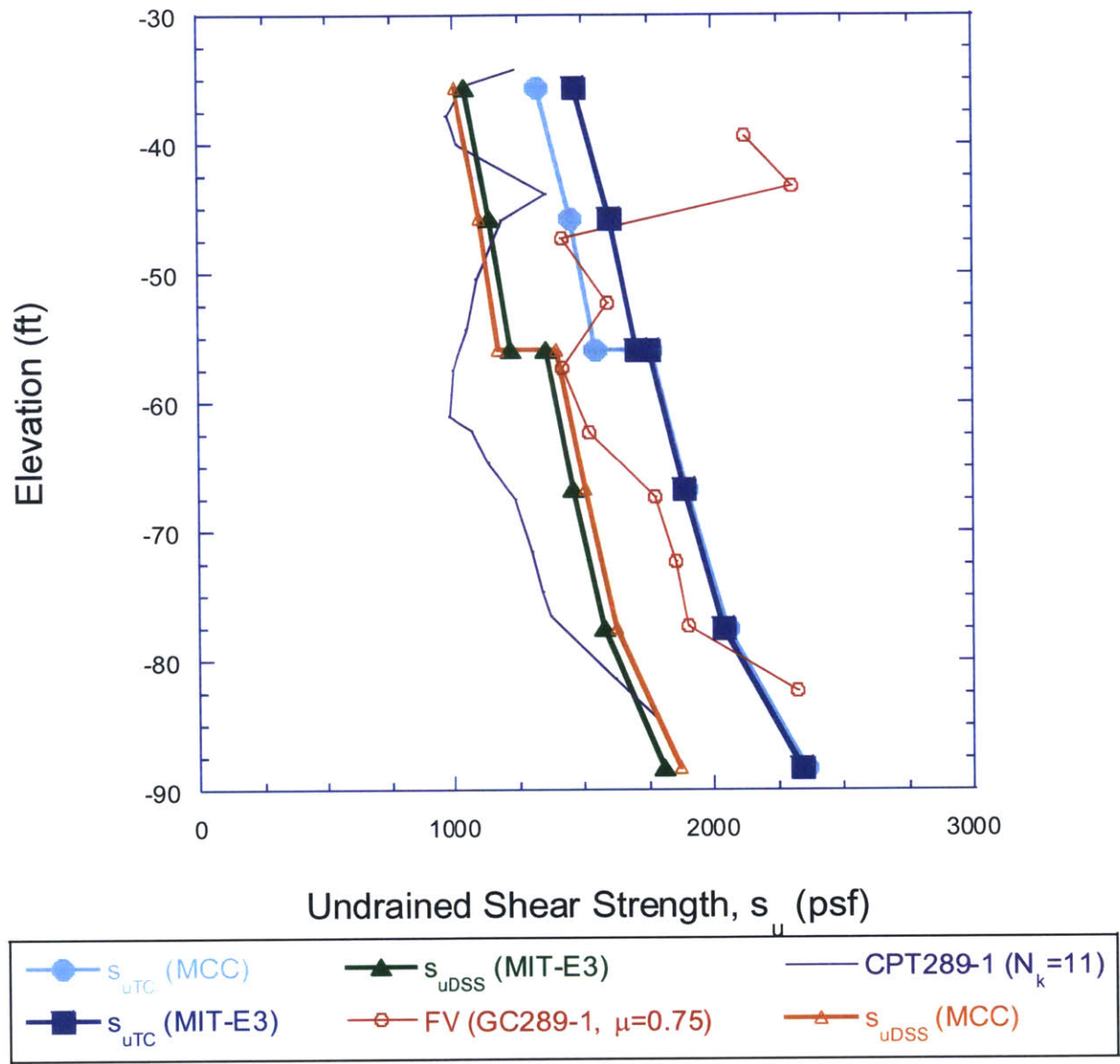


Figure 4-9. Undrained shear strength comparison with measured field data

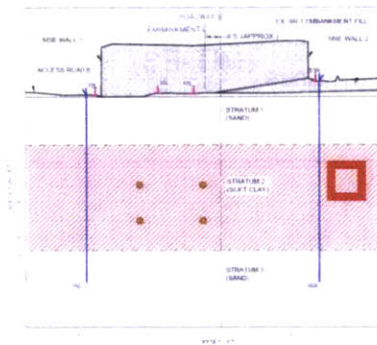
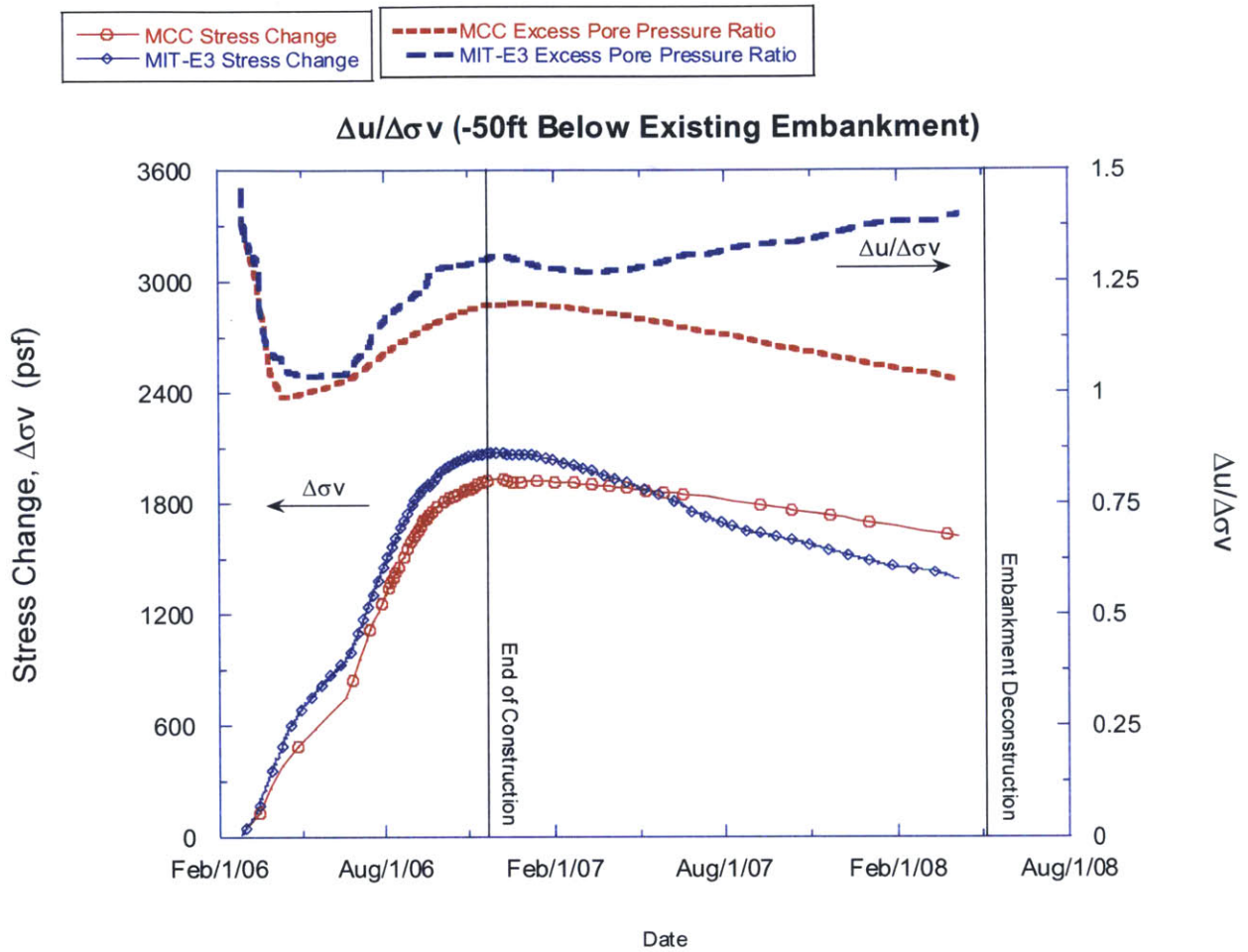


Figure 4-10. Comparison of change in total vertical stress and excess pore pressure ratio as a result of embankment construction predicted with the MCC and MIT-E3 model below existing SR1 embankment (70R, -50 ft.)

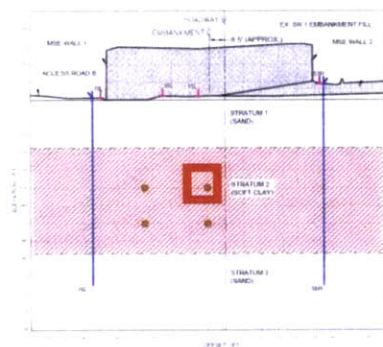
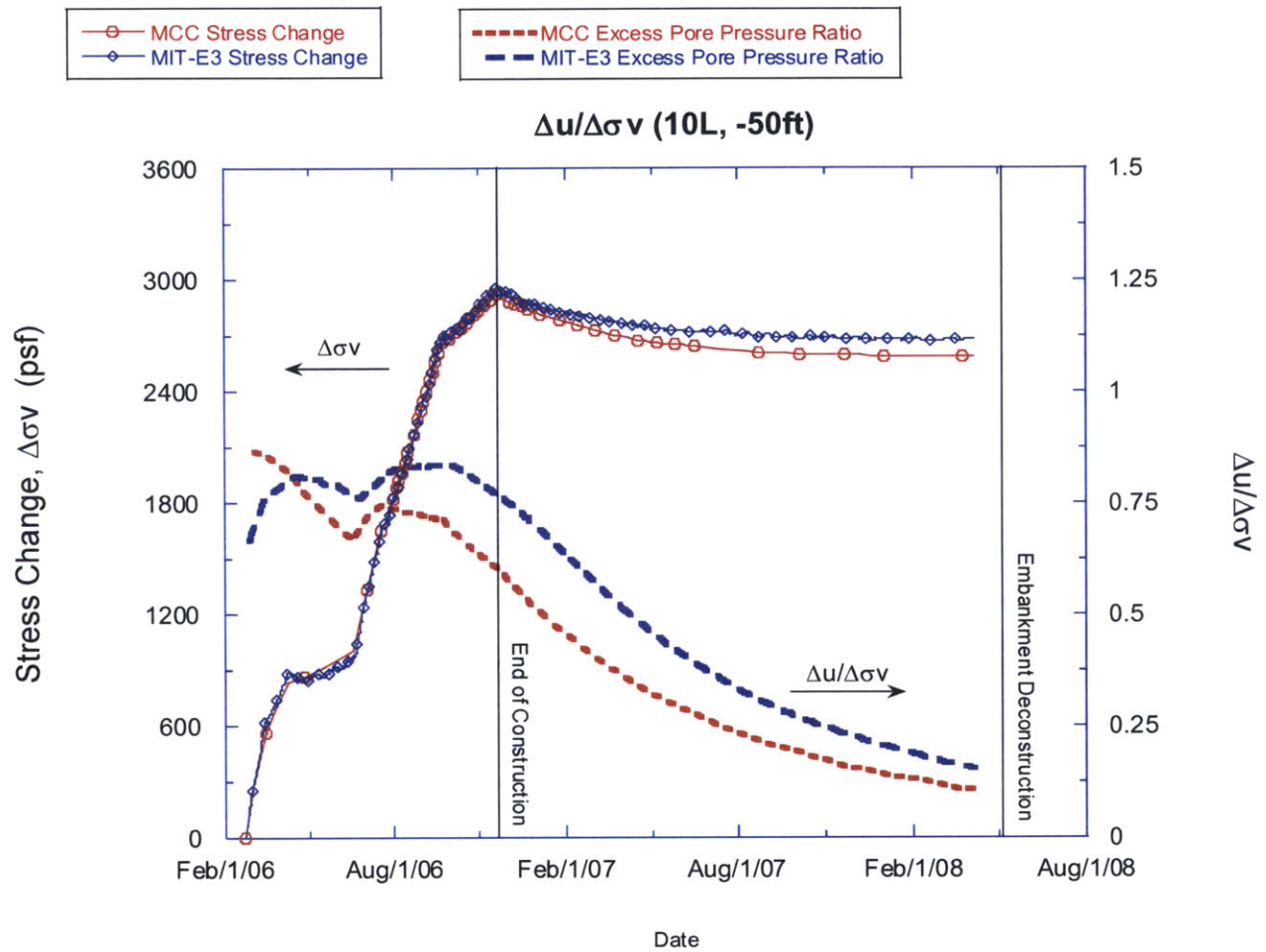


Figure 4-11. Comparison of change in total vertical stress and excess pore pressure ratio as a result of embankment construction predicted with the MCC and MIT-E3 model in the zone of the wick drain (10L, -50 ft.)

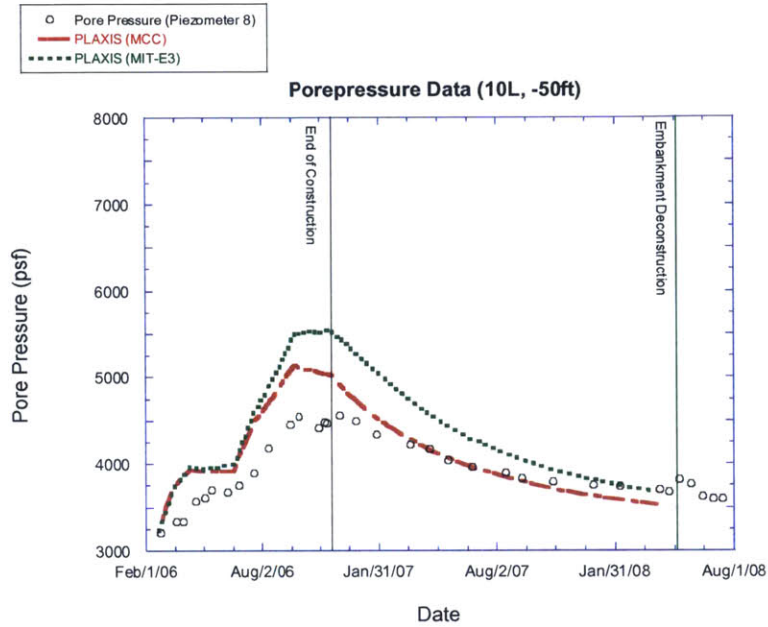


Figure 4-12a. Pore pressure comparison between PLAXIS MCC prediction and measured data (10L, -50 ft.)

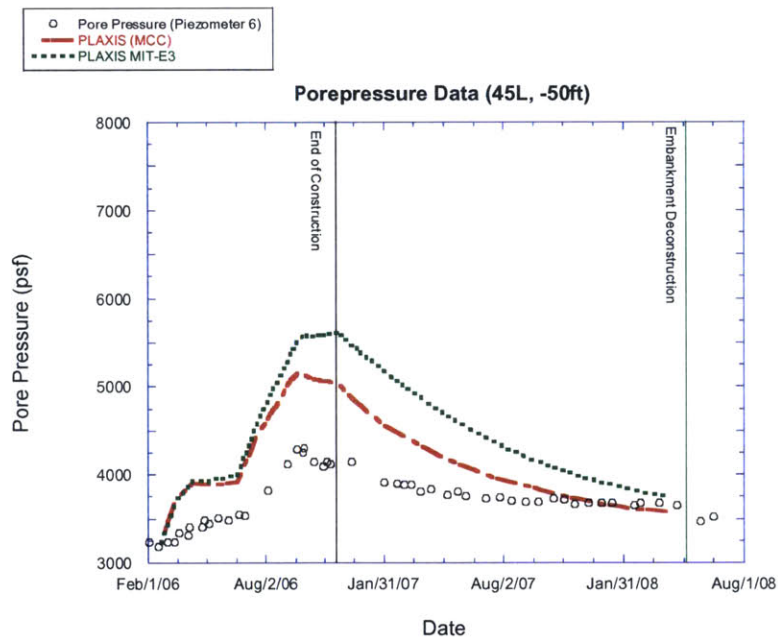


Figure 4-12b. Pore pressure comparison between PLAXIS MCC prediction and measured data (45L, -50 ft.)

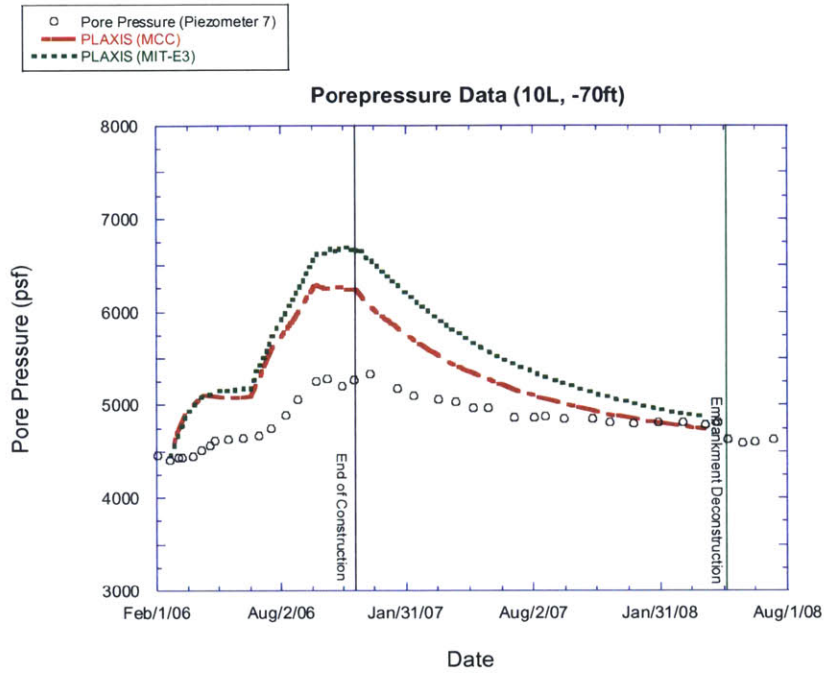
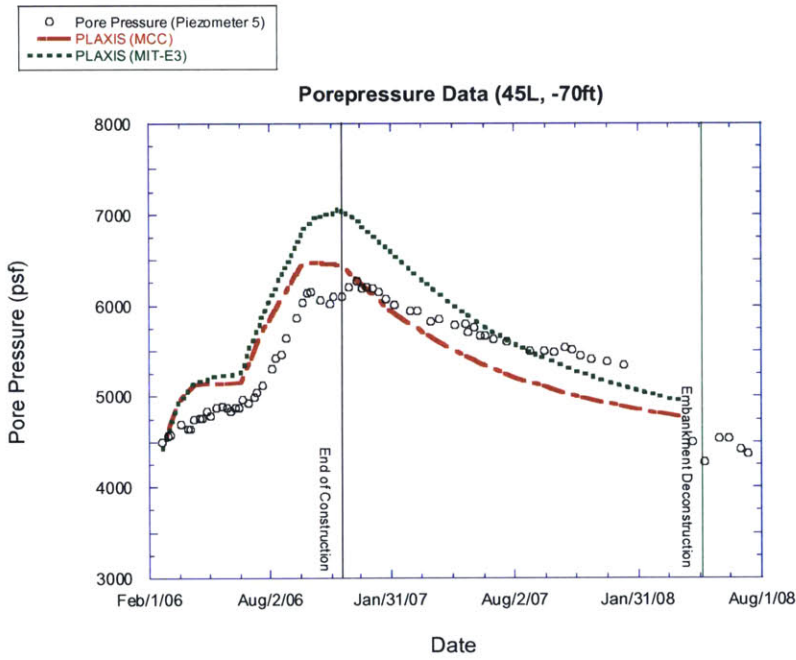


Figure 4-13a. Pore pressure comparison between PLAXIS MCC prediction and measured data (10L, -70 ft.)



*--

Figure 4-13b. Pore pressure comparison between PLAXIS MCC prediction and measured data (45L, -70ft)

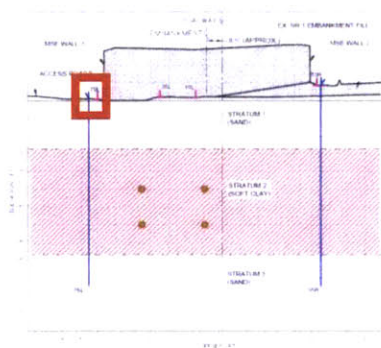
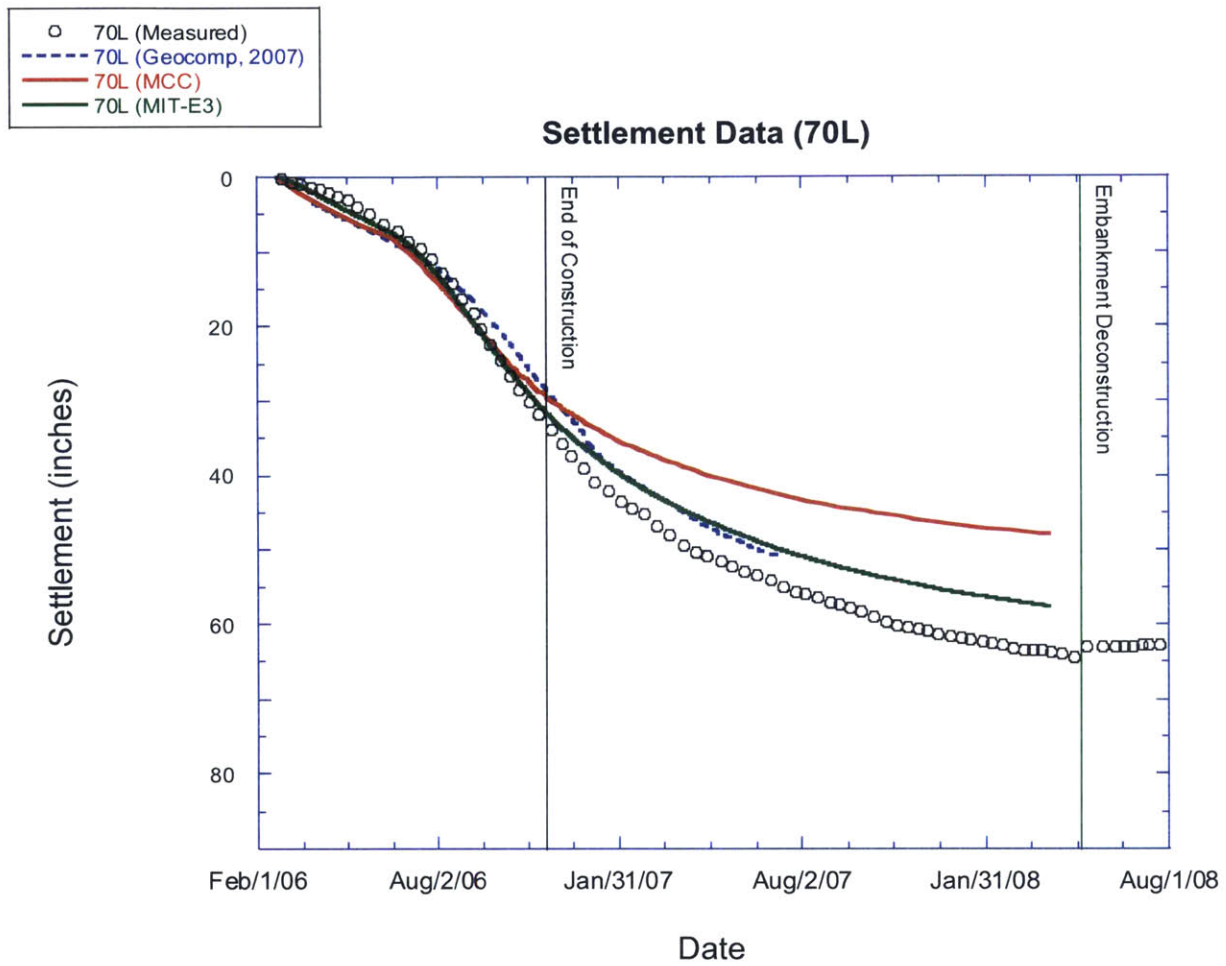


Figure 4-14. Comparison between predicted, and measured settlement data at settlement plate 70L.

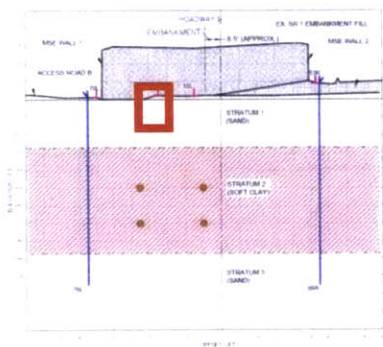
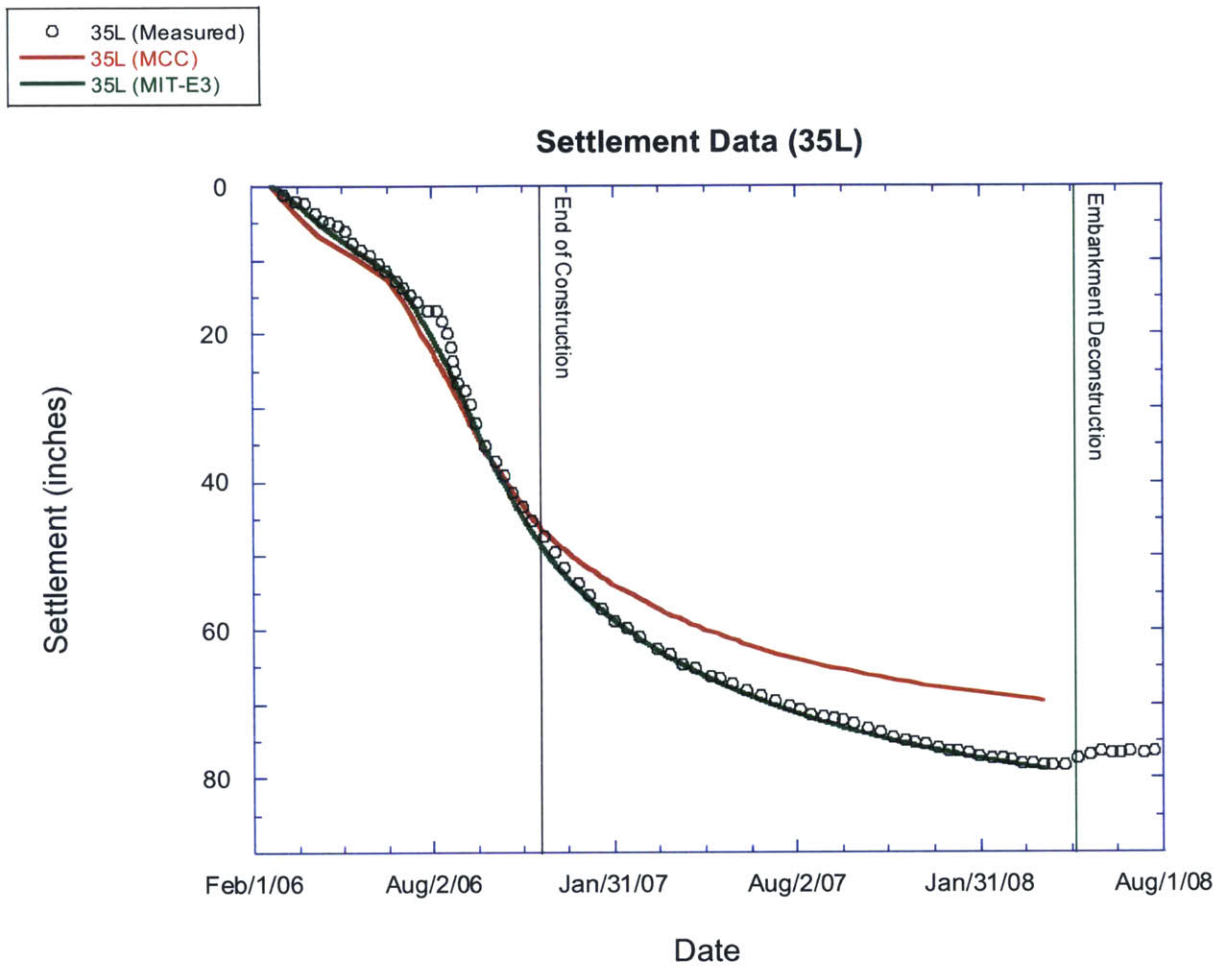


Figure 4-15. Comparison between predicted, and measured settlement data at settlement plate 35L.

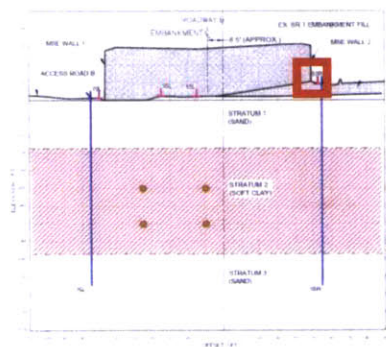
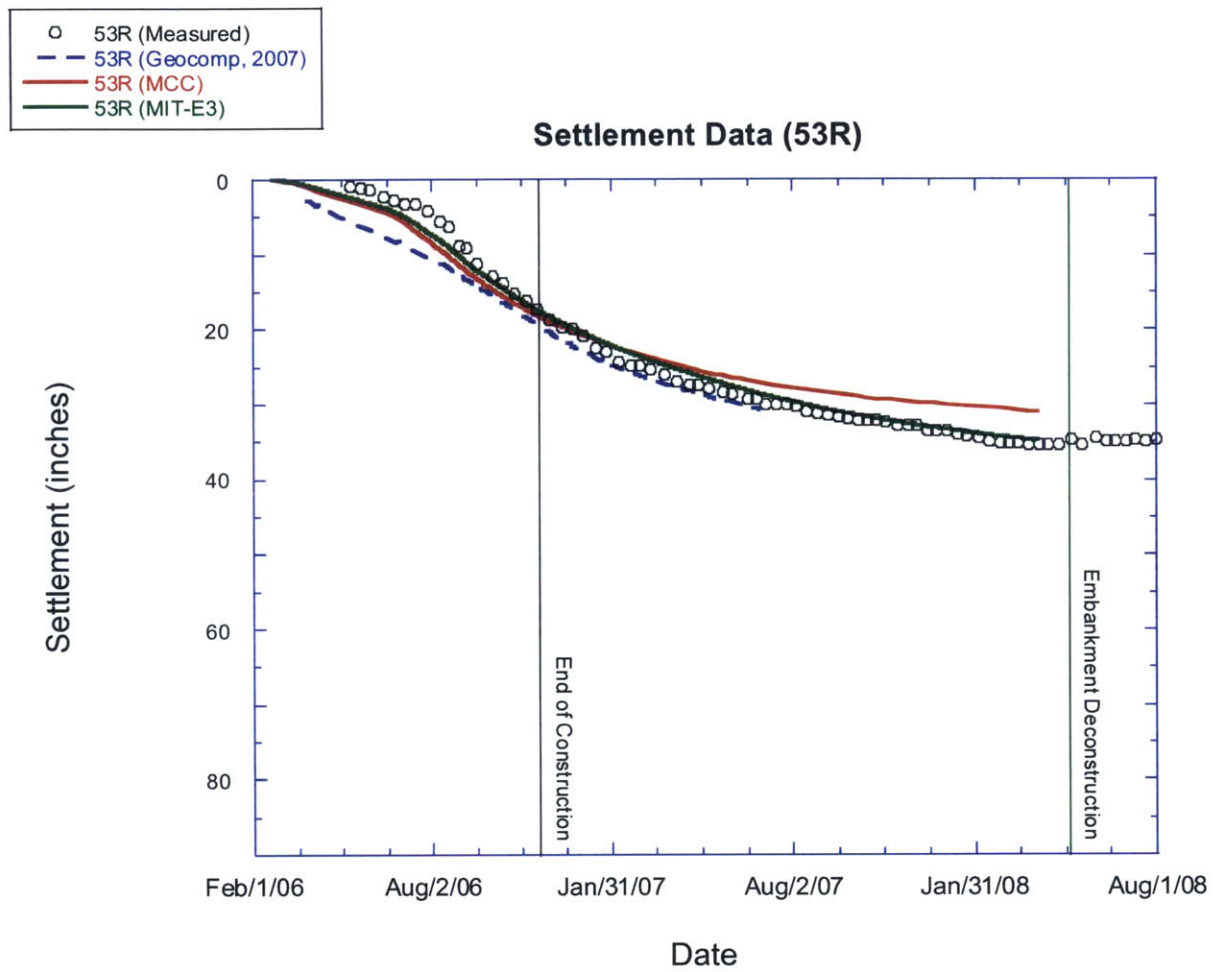


Figure 4-17. Comparison between predicted, and measured settlement data at settlement plate 53R.

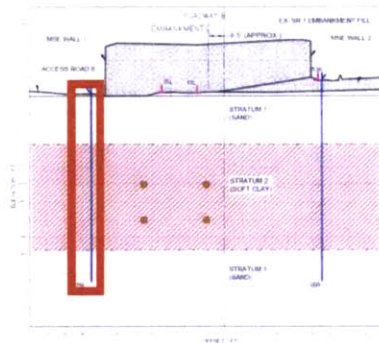
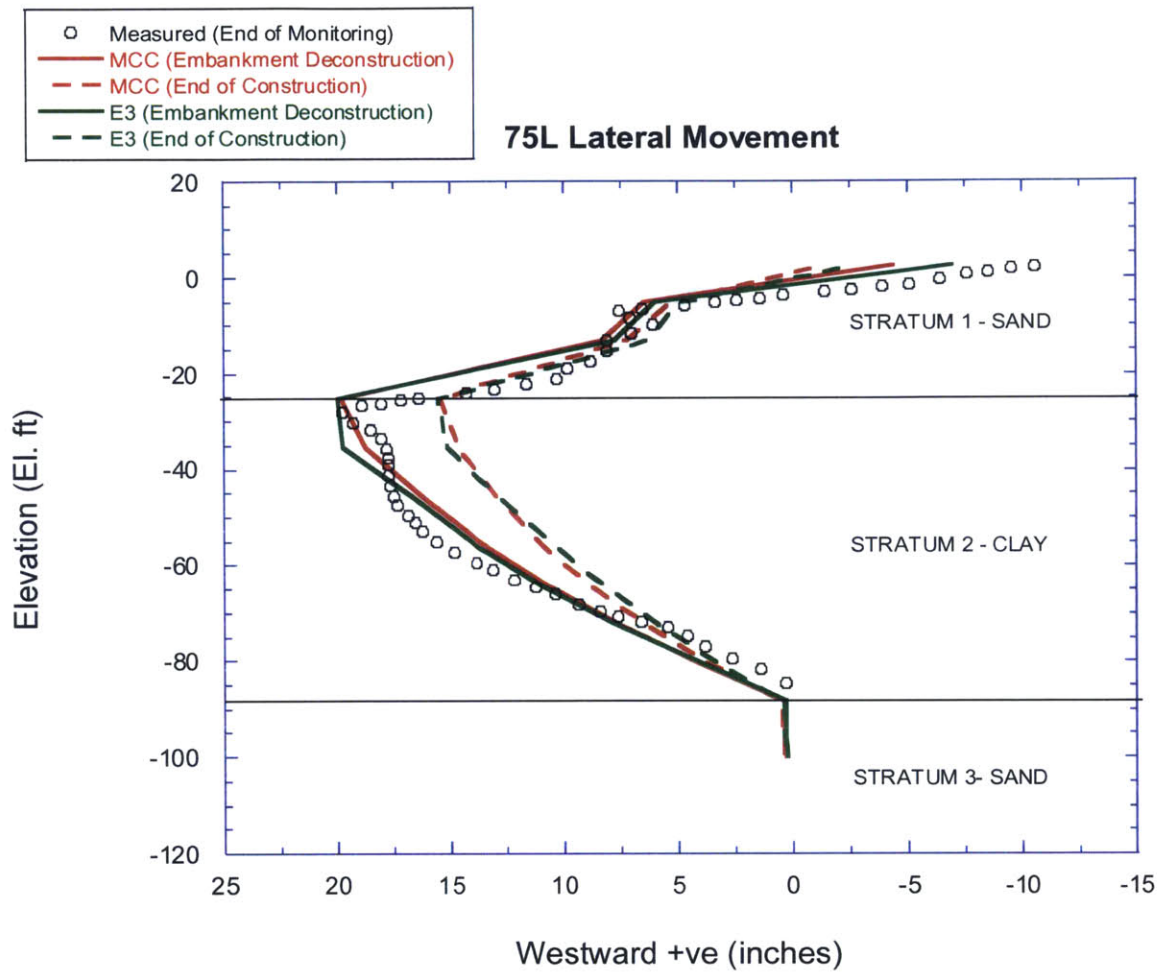


Figure 4-18. Lateral deformation comparison between PLAXIS prediction and measured data at inclinometer 75L.

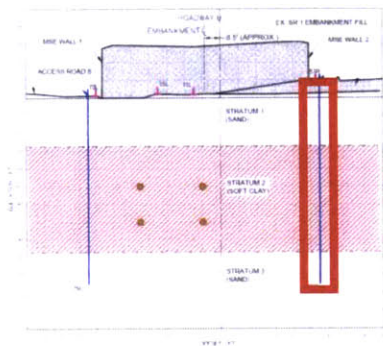
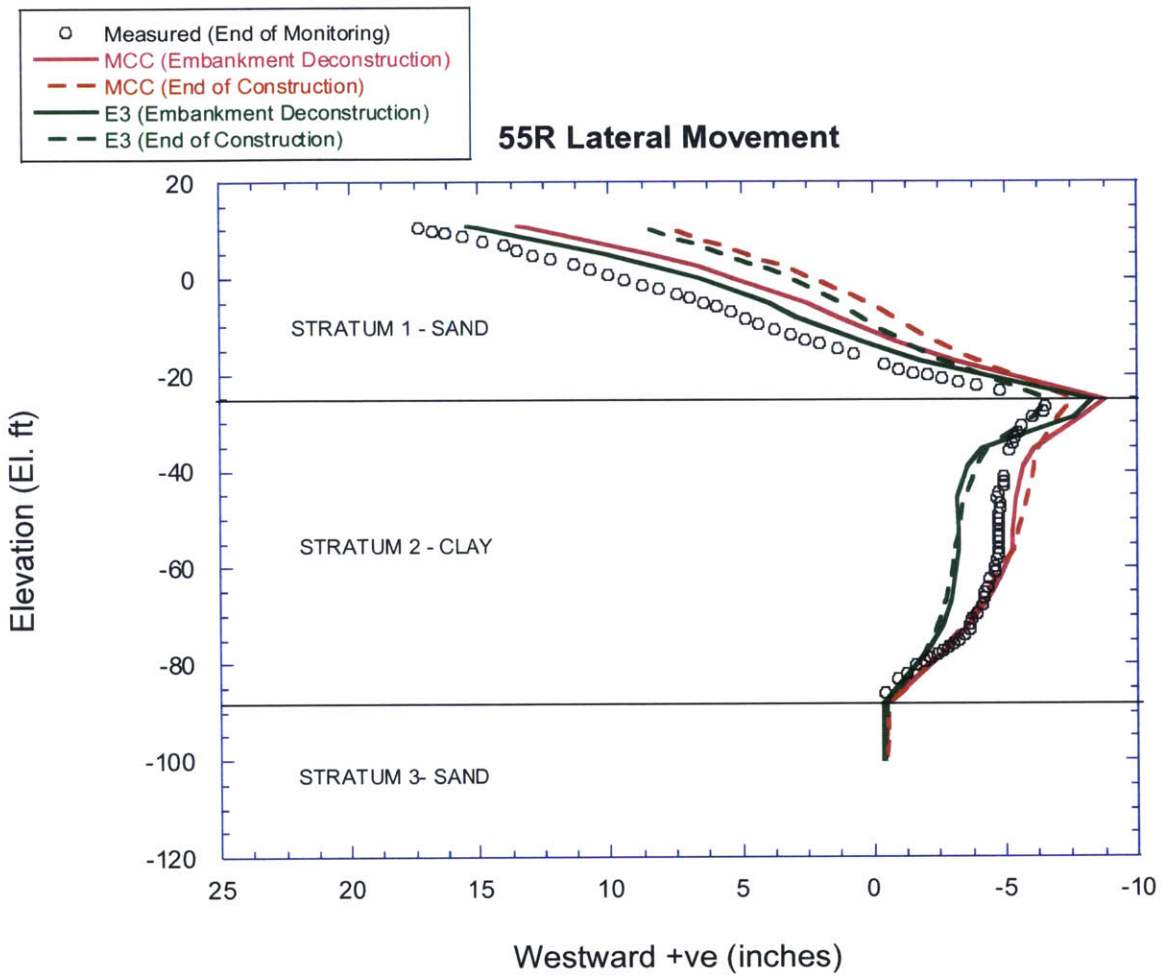


Figure 4-19. Lateral deformation comparison between PLAXIS prediction and measured data at inclinometer 55R.

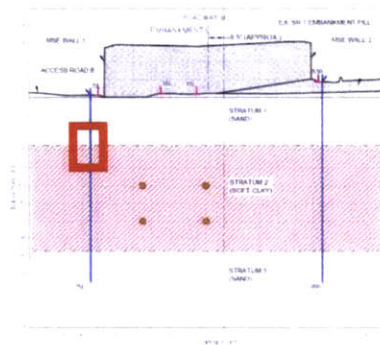
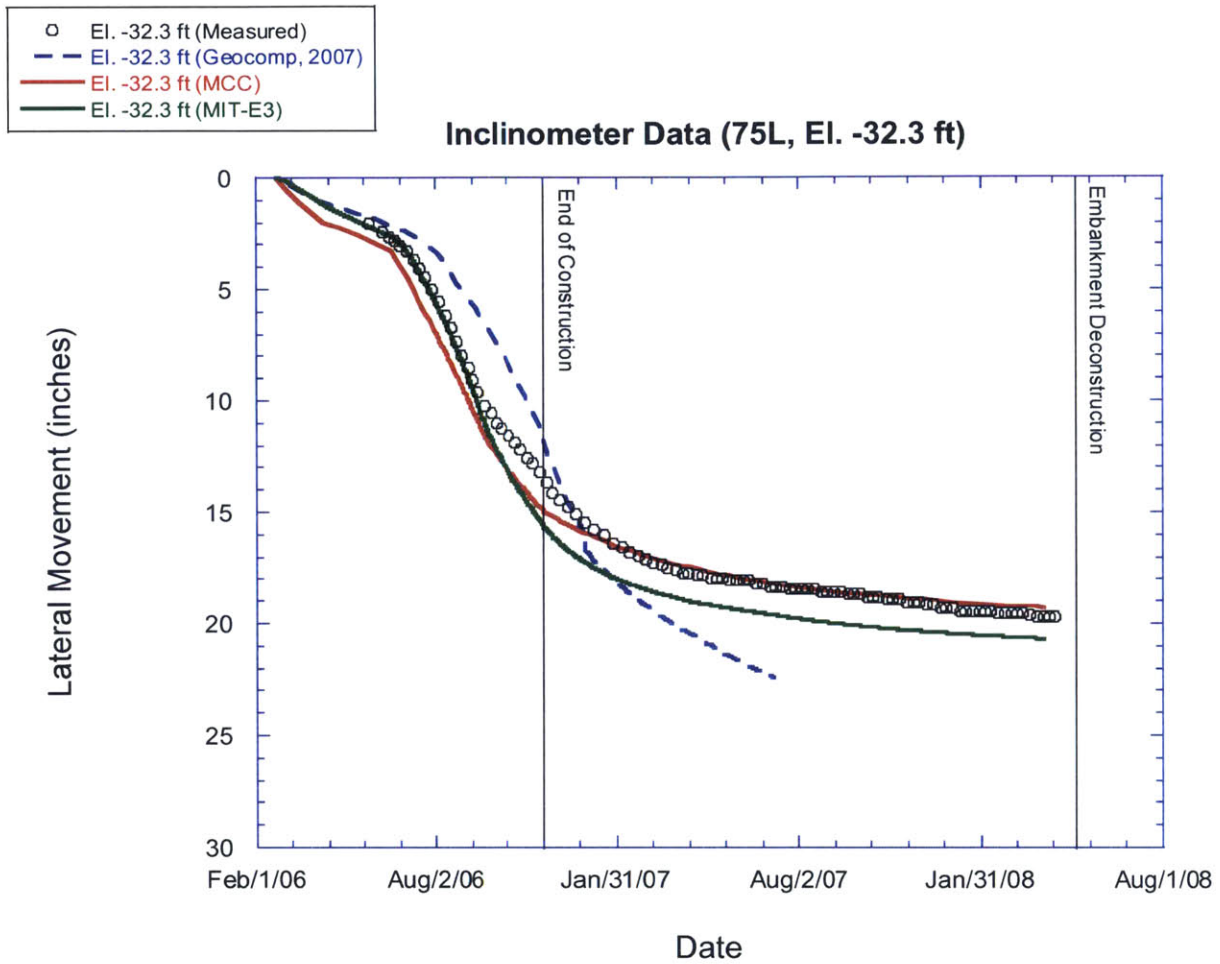


Figure 4-20. Lateral deformation comparison between PLAXIS prediction, Geocomp prediction, and measured data at inclinometer (75L, El. -32.3 ft.)

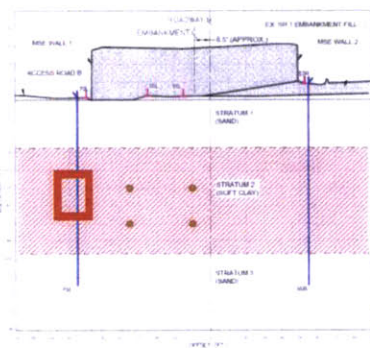
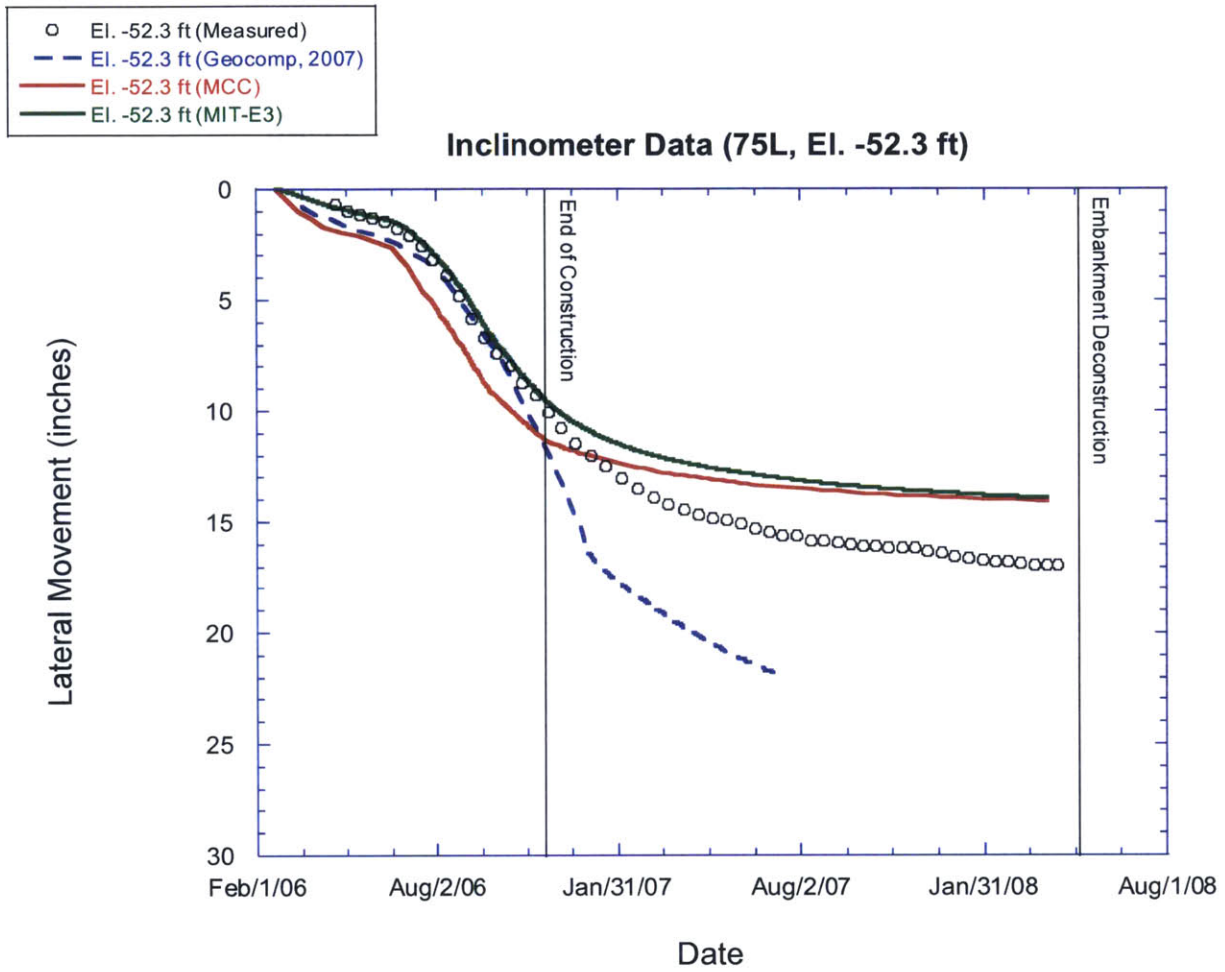


Figure 4-21. Lateral deformation comparison between PLAXIS prediction, Geocomp prediction, and measured data at inclinometer (75L, El. -52.3 ft.)

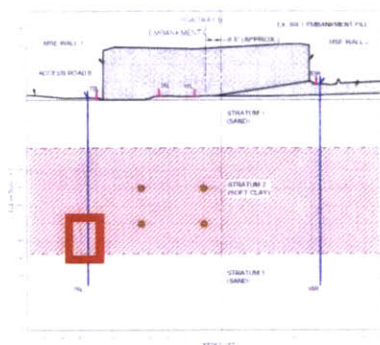
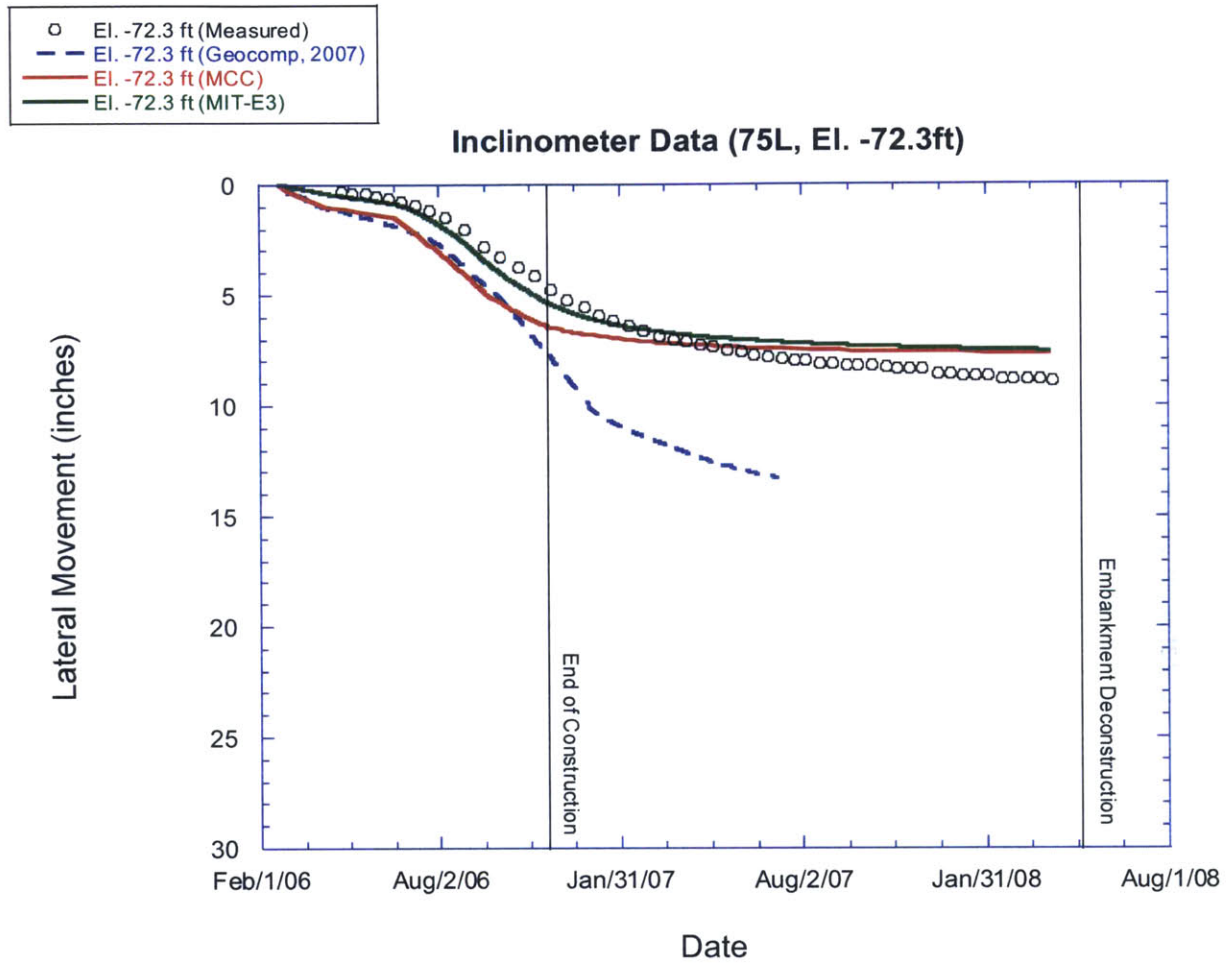
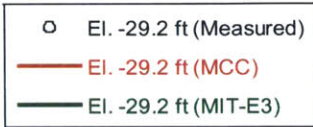


Figure 4-22. Lateral deformation comparison between PLAXIS prediction, Geocomp prediction, and measured data at inclinometer (75L, El. -72.3 ft.)



Inclinometer Data (55R, -29.2 ft)

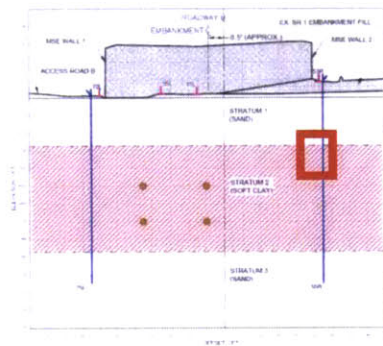
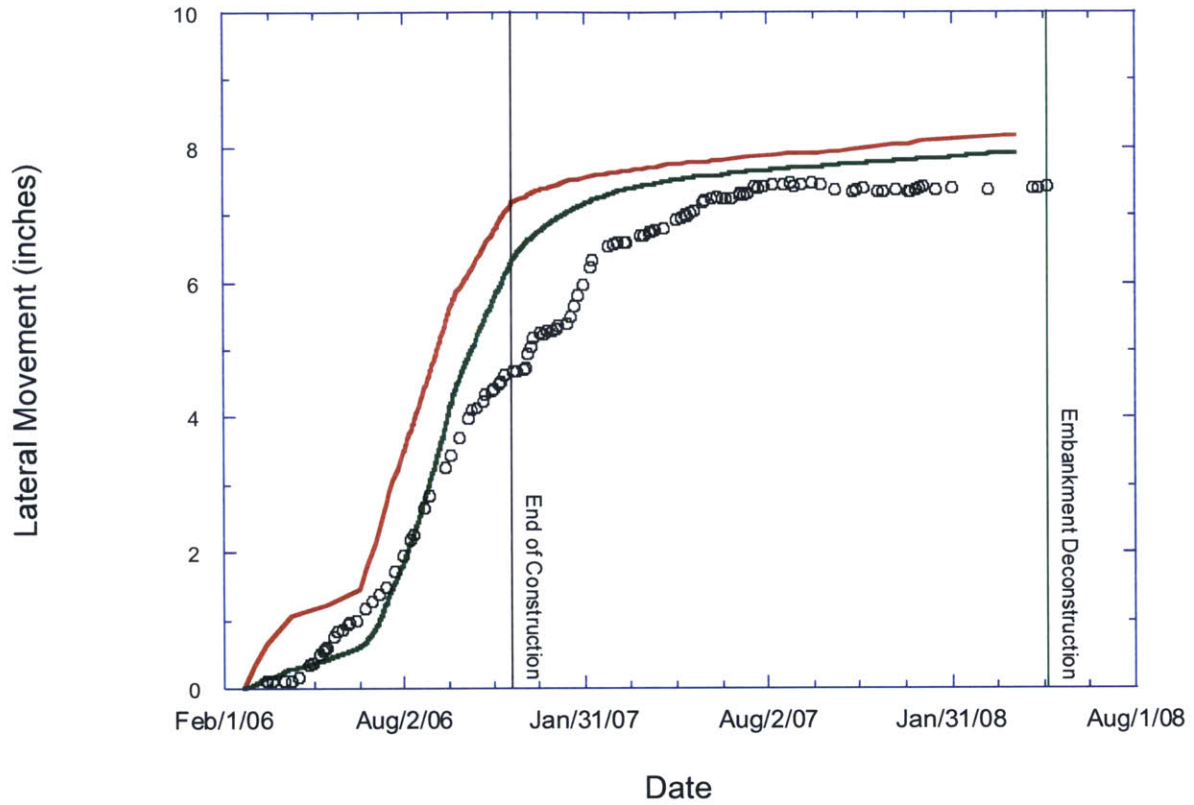


Figure 4-23. Lateral deformation comparison between PLAXIS prediction, Geocomp prediction, and measured data at inclinometer (55R, El.-29.2 ft.)

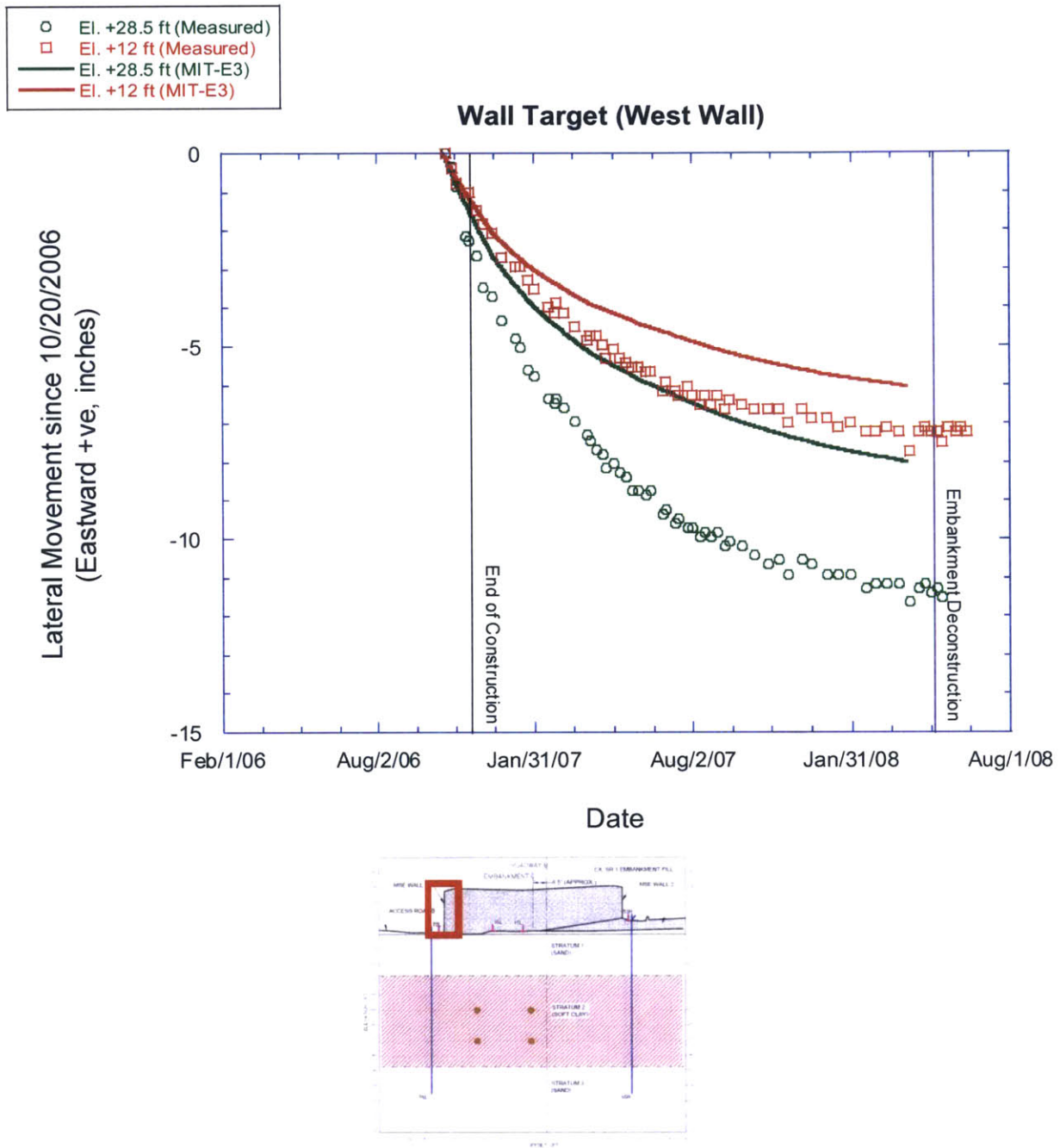


Figure 4-24. Lateral movement comparison of wall target and PLAXIS prediction at West Wall

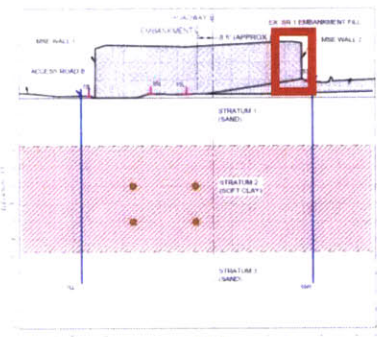
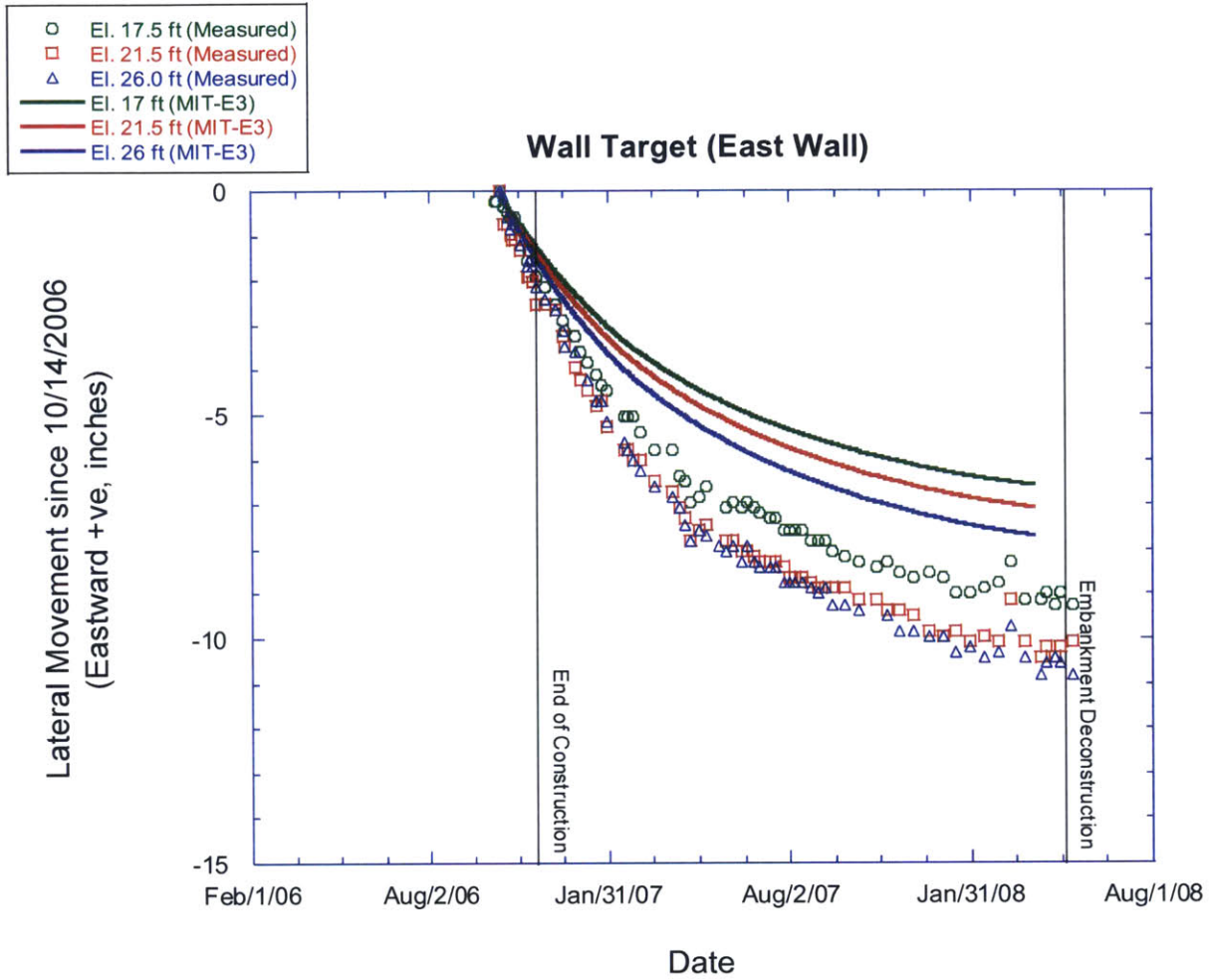


Figure 4-25. Lateral movement comparison of wall target and PLAXIS prediction at East Wall

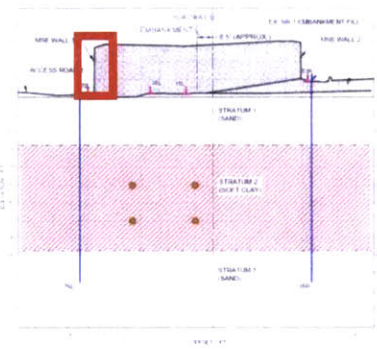
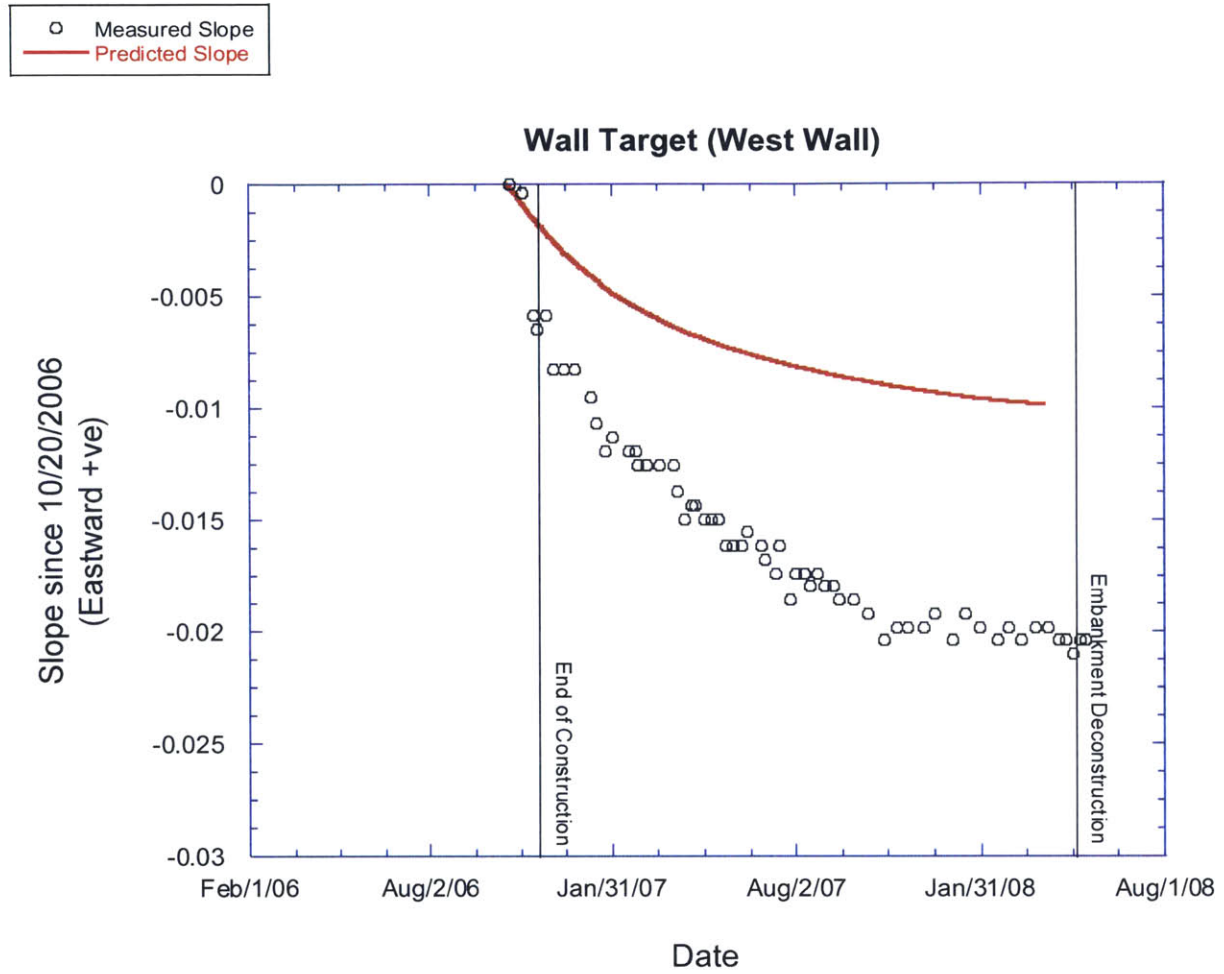


Figure 4-26. Slope of wall targets comparison with PLAXIS prediction at West Wall

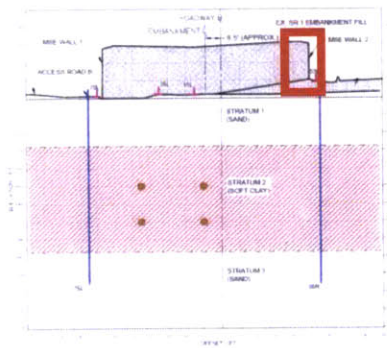
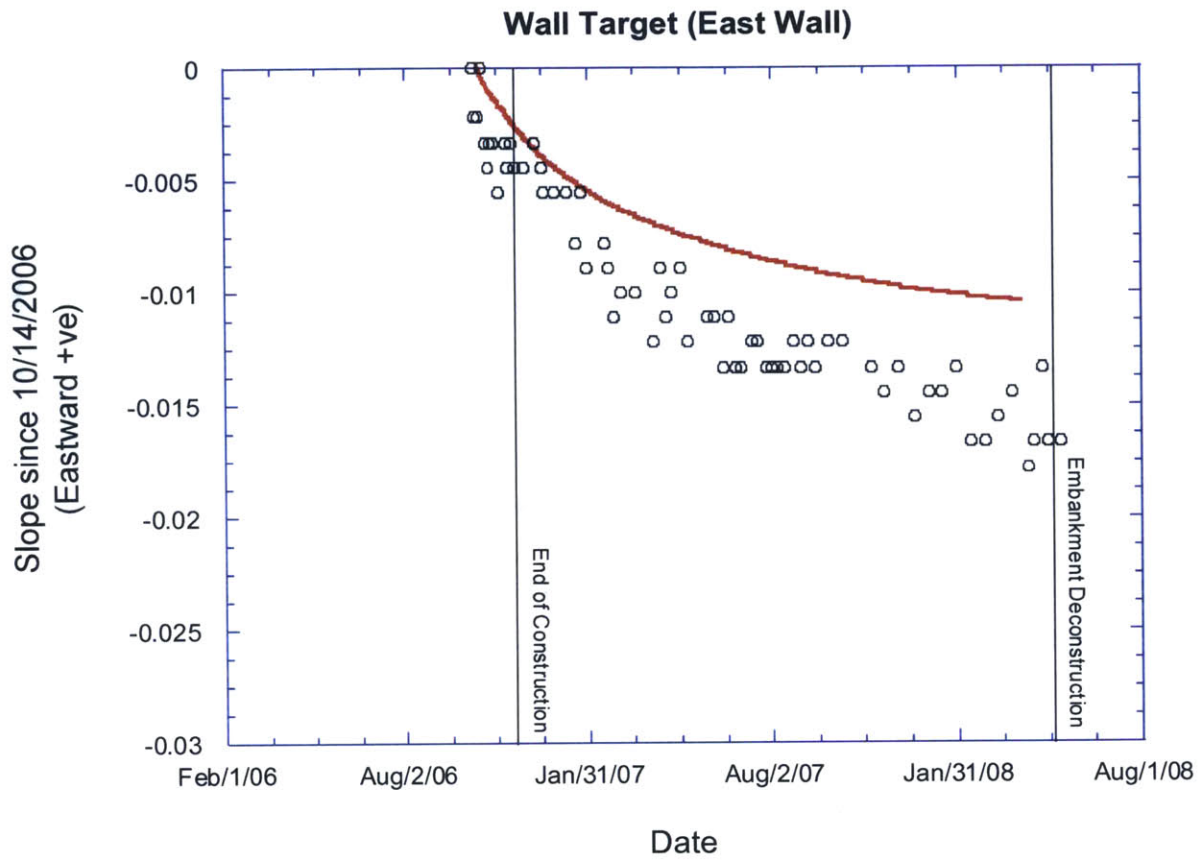
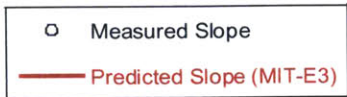


Figure 4-27. Slope of wall targets comparison with PLAXIS prediction at East Wall

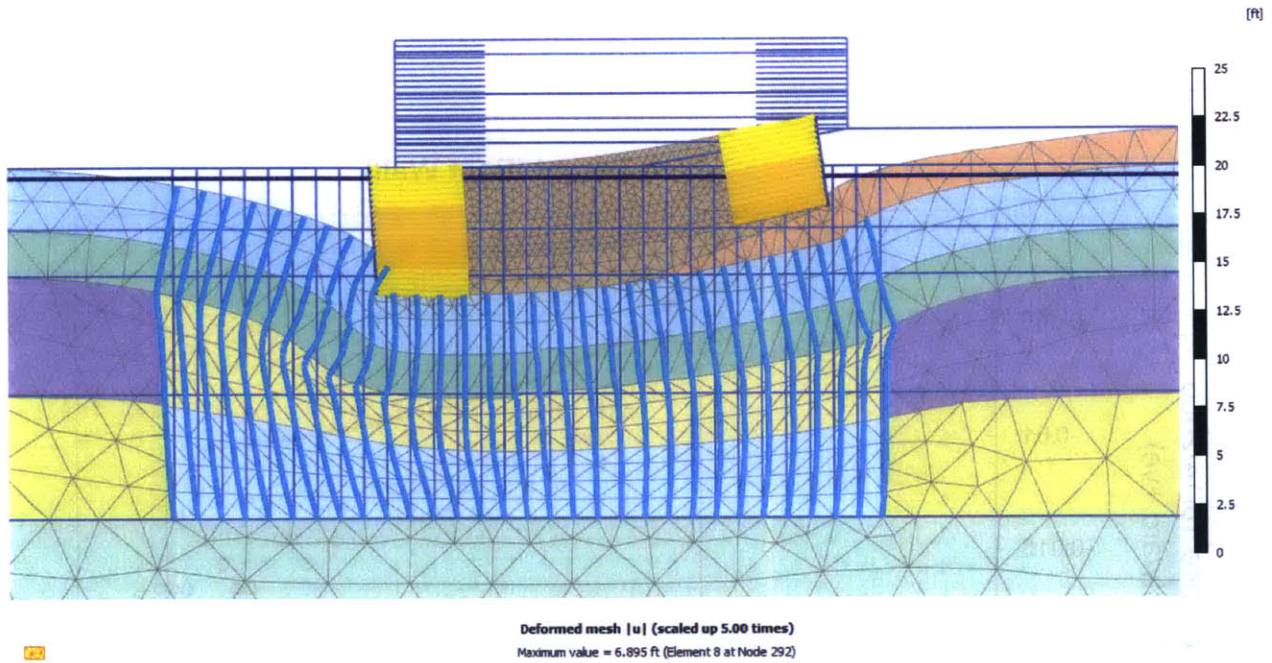


Figure 4-28. Deformed mesh predicted by the MIT-E3 model at embankment deconstruction. Deformations are exaggerated by five times relative to the true geometry.

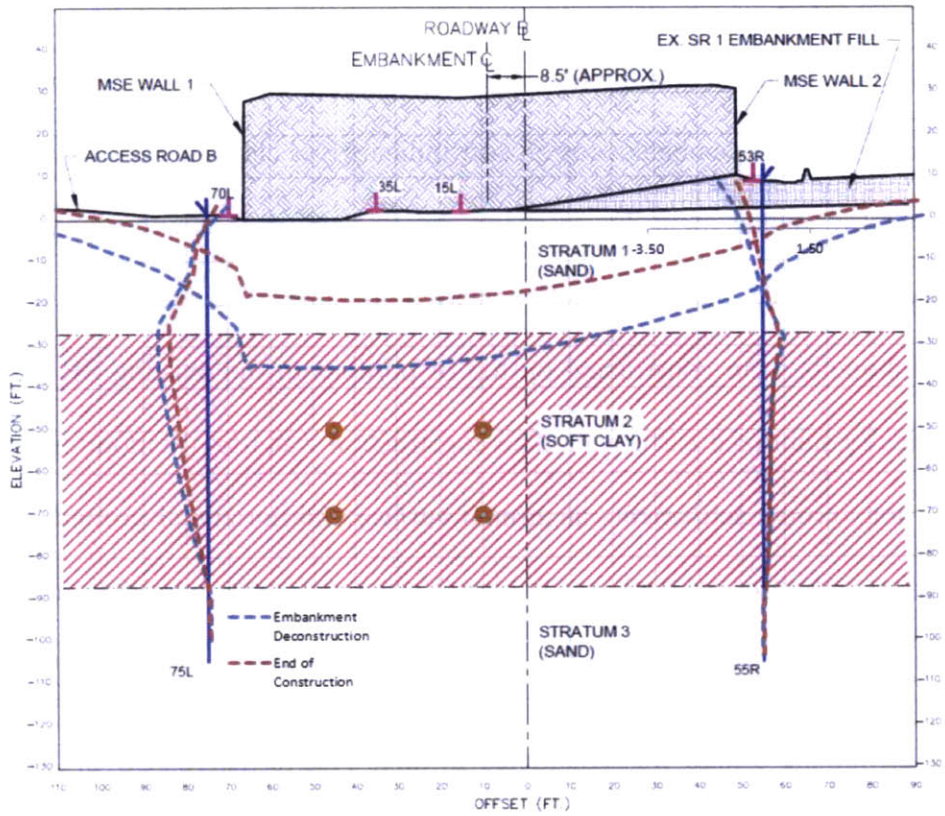


Figure 4-29. Ground movements at end of construction and embankment deconstruction.

5.0 CONCLUSIONS

This thesis evaluates the use of finite element using PLAXIS-2D AE™ as a tool for predicting the large deformations of an embankment on soft Indian River clay. As the original SR1 Bridge 3-156 was in need of replacement due to scour, design work on a new bridge over the Indian River Inlet began in 2003 and construction started in 2005. The Indian River Inlet bridge approach embankments were constructed on top of portions of the existing SR1 embankments with a mechanically stabilized earth wall. The construction was heavily monitored, particularly at Sta.289+00, for vertical settlements at ground surface and horizontal ground movements as well as pore water pressures at depth in the clay. Because of large deformations that exceeded the original predictions by the designers, the embankment was deconstructed in 2008.

Site investigation for the bridge was conducted in three phases (MACTEC 2003a, 2003b; and Geocomp, 2007) and was used in this thesis to reanalyze the data for the development of a numerical model for Sta.289+00 of the south embankment. Sample quality was assessed based on recommendations from Ladd and DeGroot (2003) to make a sensible interpretation of the scatter in the data. For 1-D consolidation tests, it was shown in this thesis that measured vertical strain to in-situ overburden stress in reloading correlates to OCR values <1 for poor quality samples and OCR=1 to 1.3 for better quality samples. From this analysis, the soft clay layer was divided into two layers to best capture the compressibility and strength parameters of the clay. Compression index, C_c , values of 0.6 and 1.4 were selected for the upper and lower units of the clay layer, which were larger values than estimated by the original designers. Large strain friction angles were interpreted from the CK_0UC triaxial testing of 31° and 37° , which were significantly larger than interpretations made from the CIUC triaxial testing conducted by MACTEC (2003a,b).

The interpretations from the laboratory testing were used as input parameters in effective stress soil models used in the finite element modelling. Modified Cam-Clay and the MIT-E3 model were used to capture the behavior of normally consolidated Indian River clay. For simplicity, the Mohr-Coulomb model was used to model the fully drained, cohesionless sand deposits based on $N_{1,60}$ values from borings. In general, the MIT-E3 model predicted slightly large settlements and greater differential settlements than the MCC model, while the MCC predicted larger horizontal movements than the MIT-E3 in the East edge of the embankment.

The model was used to examine the mechanisms of differential ground movement in the clay including undrained shear deformation, consolidation settlement as well as redistribution of total vertical stresses. It was shown that the majority of both the undrained shear deformation and the lateral movements in the clay occurred mainly before the end of construction. On the other hand, from the examination of vertical settlements and dissipation of pore water pressures, consolidation settlement occurs well beyond the end of construction until the embankment was deconstructed. This suggests the lateral squeeze or horizontal deformations in the clay was a result of the undrained shear deformation and the vertical settlements that occurred afterwards are due to the consolidation settlement. It was also shown that the lateral deformations are restrained by the sand layer at surface. The differential movements in the clay was shown to be related to the stiffening of the clay from the prefabricated vertical drains, redistribution of total vertical stresses as well as the differential loading of the embankment construction. Soil arching was significant on this project as a result of the movement of excess porewater pressures as well as the previous consolidation of the existing SR1 embankment construction. The MIT-E3 and MCC results differed in this respect as the MIT-E3 predicted a larger amount of redistribution of total stresses throughout the depth of the clay layer which resulted in greater differential

settlement. Further, the MIT-E3 model predicted larger excess pore water pressures in the both the zones underneath the existing SR1 embankment and within the zone of the wick drains.

Using a reasonable interpretation of the material properties and effective stress soil modelling, the results from the 2D-plane strain finite element analysis show a good agreement with the measured data at the site for both the lateral deformation and vertical settlement of the clay. There is consistent agreement between the predicted results for both the MCC and MIT-E3 models with the measured data in both magnitude of settlement and rate of settlement. The MIT-E3 model matched the settlement data slightly more accurately especially at the West edge of the embankment, with percent error between measured settlement plate data and computed result less than 10%. The MIT-E3 model slightly under-predicts the total lateral deformation by 4.5 ft³/ft (less than 5% error) but accurately captures the differential lateral movements. On the other hand, the MCC marginally overestimates the total lateral deformations by 1.2 ft³/ft but underestimates the differential movements somewhat. In particular, the lateral deformation in the clays were more accurately predicted than estimates made by Geocomp (2007) which largely over-predict the lateral movements in the clay using the Soft-Soil-Creep model in PLAXIS. However, while the finite element analysis correctly predicted the direction of the tilt of the wall it was not able to reproduce the magnitude of the base-lined slope measurements as there is uncertainty with the stiffness input parameters for the modelling of the wall.

A careful examination and interpretation of the soil parameters led to relatively accurate predictions of the ground movements using finite element analyses and effective stress soil models in staged construction of an embankment. This thesis focuses solely on Sta.289+00 on the South bank using 2-D plane-strain analyses. The interpretation of model input parameters was based on a reasonable judgement of the available data and was not meant to fit the measured

results. Refinement of these parameters may lead to more accurate predictions of the results. Further study is recommended with the use of 3-D finite element analyses to capture the geometry of the existing and new embankments particularly at the bridge abutment location at Sta.293+00.

REFERENCES

- Berkheimer, S.A (2007). Instrumented Geogrid Reinforced Mechanically Stabilized Earth Wall Undergoing Large Settlement, *Master's Thesis*. University of Delaware
- Bowles, J.E. (1997). Foundation Analysis and Design Fifth Edition, McGraw-Hill, New York. ISBN 0-07-118844-4
- Geocomp Corporation (2007). Indian River Inlet Bridge Project, Report on Independent Geotechnical Review, prepared for the Delaware Department of Transportation, dated August 17, 2006)
- Golder Associates (2011). Geotechnical Assessment of Embankment Approach Fills at the Indian River Inlet Bridge Project, prepared for the Delaware Department of Transportation, dated January 3, 2011
- Golder Associates (2013). Reply Report on Defendant's Expert Reports at the Indian River Inlet Bridge, prepared for the Delaware Department of Transportation, dated September 30, 2013
- Hird, C. C., Pyrah, I. C. & Russell, D. (1992). Finite element modelling of vertical drains beneath embankments on soft ground, *Géotechnique* 42, No. 3, 499-511
- Ladd, C.C. (1991), Stability Evaluation During Staged Construction, *22nd Terzaghi Lecture, ASCE Journal of Geotechnical Engineering* Vol. 117, No.4, April, pages 540-614
- Ladd, C.C., Whittle., A.J., Legaspi, D.E. (1994). Stress-Deformation Behavior of an embankment on Boston Blue Clay, *Conference Proceedings: Vertical and Horizontal Deformations of Foundations and Embankments* pp. 1730-1759
- Ladd, C.C. and DeGroot, D.J., (2003), Recommended Practice for Soft Ground Site Characterization, Arthur Casagrande Lecture, 12th *Panamerican Conference on Soil Mechanics and Geotechnical Engineering*, Vol 1, 1-57,
- MACTEC Engineering and Consulting (2003). Indian River Inlet Bridge Project, Final Geotechnical Roadway Report, prepared for Figg Engineering Group dated September 26, 2003.
- MACTEC Engineering and Consulting (2003). Indian River Inlet Bridge Project, Site Characterization and Preliminary Geotechnical Study, prepared for Figg Engineering Group dated December 24, 2003.
- MACTEC Engineering and Consulting (2005). Indian River Inlet Bridge Project, Geotechnical Summary Report, prepared for Figg Engineering Group dated April 26, 2005.
- MACTEC Engineering and Consulting (2007). Indian River Inlet Bridge Project, Roadway Calculations Package, prepared for Figg Engineering Group dated March, 7 2007.

- MACTEC Engineering and Consulting (2007). Indian River Inlet Bridge Project, Summary of Soil Design Parameters, prepared for Figg Engineering Group dated March 7, 2007.
- Matsuo, M. and Kawamura, K. (1977), Diagram for Construction Control of Embankment on *Soft Ground*, *Soils and Foundations*, 17(3), 37- 52
- Mesri, M., and Choi, Y. (1985). Settlement Analysis of Embankments on Soft Clays, *Journal of Geotechnical Engineering*, Vol. 111, No. 4, April 1985, pp. 441-464
- Olson, R. (1998). Settlement of Embankments on Soft Clays, (*The Thirty-First Terzaghi Lecture*). *J. Geotech. Geoenviron. Eng.*, 124(4), 278–288.
- PLAXIS 2D User's Manuals (2010), Edited by Brinkgreve, R.B.J., Swolfs, W.M. and Engin, E., Plaxis BV, Delft, The Netherlands
- Poulos, H.G., and Davis, E.H. (1974). Elastic Solutions for Soil and Rock Mechanics, John Wiley and Sons. ISBN 0-471-69565-3
- Ramsay, K.W. (1999). Cross Section of Pliocene and Quarternary Deposits Along the Atlantic Coast of Delaware, Delaware Geological Survey.
- Schofield, A., and Wroth, P. (1968). Critical State Soil Mechanics, McGraw-Hill. ISBN 978-0641940484
- Tavenas, F., Mieussens, C., and Bourges, F. (1979). Lateral Displacements in Clay Foundation Under Embankments, *Canadian Geotechnical Journal*, 16, 532-550
- Tensor International Corporation (2012). Tensor Uniaxial Geogrids for Soil Reinforcement. *Product Brochure*. Alpharetta, GA.
- Vermeer, P.A. and Neher, H.P. (1999). A soft soil model that accounts for creep. *In: Proceedings PLAXIS Symposium "Beyond 2000 in Computational Geotechnics"*: 249-262. Amsterdam
- Whittle, A.J. (1993). Evaluation of a constitutive model for overconsolidated clay, *Géotechnique*, 43(2), 289-315.
- Whittle, A. J., Kavvas M. J., (1994), Formulation of MIT-E3 Constitutive Model for Overconsolidated Clays, *Journal of Geotechnical Engineering*, ASCE, 120(1), (173-198).
- Wong. Y.K (2013). Comparison of Drainage Line Elements in PLAXIS 2D and 3D applied in Consolidating Marine Clay Deposits, *SEIC 2013*. IP 6-63

APPENDIX A

Documentation on the use of MIT-E3 model in PLAXIS:

MMT

MMT files are used to change material parameters

Used for

- 3DFoundation 2: **XXSNFXK.DF3/mmtfile** or **XXSNFXK.DF3/xxsnfxx.mmt**
- Plaxis 2D 201x: **project.P2DAT/data.mmt.rs#** (# = a for all phases, or use # = integer for phase ID)
- Plaxis 3D 201x: **project.P3DAT/data.mmt.rs#** (# = a for all phases, or use # = integer for phase ID)

Example

```
1 number of (important) lines
3 1 5 0.05
```

In general, there are 4 values per line

```
i j k v
```

i: 1=soil, 2=anchor, 3=geotextile, 4=plate, 5=Beam3, 11 : mtypel

j: material set number

k: parameter number

v: new value

Another example

```
5
11 1 115 0.0 mtypel(1) = 115 = drained model 15
1 1 31 3.0 prolay(31,1) = 3.0
1 1 32 7.5 prolay(32,1) = 7.5
1 3 38 0.5 prolay(38,3) = 7.5
4 1 5 6e3 plate propmind(5,1) = 6e3
```

```
18  changes (1 material type + 17 parameters)

11  5 210 -999          change to undrained model (2) and 10=MIT-E1
1   5 31  1.84000000E-01 lambda
1   5 32  1.98800000E+00 1+e0
1   5 33  1.00000000E-03 kappa
1   5 34  1.05000000E+00 2G/K
1   5 35  1.46000000E+00 (1+2K0)/(3-3K0)
1   5 36  8.66000000E-01 yield surface ratio of semi axes
1   5 37  1.00000000E+02 rate of rotation of yield surface
1   5 38  0.07700000E+00 sic
1   5 39  1.05000000E+00 xkc2
1   5 40  1.60000000E+00 xmm
1   5 41  2.20000000E+01 cc
1   5 42  5.00000000E-01 gma
1   5 43  2.00000000E-01 hpo
1   5 44  4.50000000E+00 st
1   5 45  0.70000000E-01 scx
1   5 46  1.38948300E+00 ALPHAC
1   5 47  0.76379900E+00 A1C
```

18 changes
first line changes model to 210 means undrained (2) model 10 (=MIT-E1)
next 17 lines change type 1 (=soil), material set 5, index 31..47 or ProLay(31..47, 5)
The text behind the input is not read and can be an indication for the user what is changing.
Note that output does not know anything about these changes.

The text of the input file (formatted as a .mmt) used to run the MIT-E3 model for this thesis is as follows:

```
72 changes (1 material type + 17 parameters)
11 3 210 -999 change to undrained model (2) and 10=MIT-E3
1 3 31 2.60000000E-01 lambda
1 3 32 2.40000000E+00 1+e0
1 3 33 3.00000000E-03 kappa
1 3 34 0.94000000E+00 2G/K
1 3 35 1.50700000E+00 (1+2K0)/(3-3K0)
1 3 36 9.50000000E-01 yield surface ratio of semi axes
1 3 37 1.00000000E+02 rate of rotation of yield surface
1 3 38 0.14900000E+00 sic
1 3 39 0.75100000E+00 xkc2
1 3 40 1.55000000E+00 xmm
1 3 41 1.00000000E+01 cc
1 3 42 5.00000000E-01 gma
1 3 43 3.00000000E-01 hpo
1 3 44 3.00000000E+00 st
1 3 45 4.00000000E-01 scx
1 3 46 0.50000000E+00 ALPHAC
1 3 47 0.27100000E+00 A1C
11 10 210 -999 change to undrained model (2) and 10=MIT-E3
1 10 31 2.60000000E-01 lambda
1 10 32 2.40000000E+00 1+e0
1 10 33 3.00000000E-03 kappa
1 10 34 0.94000000E+00 2G/K
1 10 35 1.50700000E+00 (1+2K0)/(3-3K0)
1 10 36 9.50000000E-01 yield surface ratio of semi axes
1 10 37 1.00000000E+02 rate of rotation of yield surface
1 10 38 0.14900000E+00 sic
1 10 39 0.75100000E+00 xkc2
1 10 40 1.55000000E+00 xmm
1 10 41 1.00000000E+01 cc
1 10 42 5.00000000E-01 gma
1 10 43 3.00000000E-01 hpo
1 10 44 3.00000000E+00 st
1 10 45 4.00000000E-01 scx
1 10 46 0.50000000E+00 ALPHAC
1 10 47 0.27100000E+00 A1C
11 4 210 -999 change to undrained model (2) and 10=MIT-E3
1 4 31 4.78000000E-01 lambda
1 4 32 3.40000000E+00 1+e0
1 4 33 4.00000000E-03 kappa
1 4 34 0.94000000E+00 2G/K
1 4 35 1.15200000E+00 (1+2K0)/(3-3K0)
1 4 36 9.50000000E-01 yield surface ratio of semi axes
1 4 37 1.00000000E+02 rate of rotation of yield surface
1 4 38 0.20500000E+00 sic
1 4 39 1.04900000E+00 xkc2
1 4 40 1.55000000E+00 xmm
1 4 41 1.00000000E+01 cc
1 4 42 5.00000000E-01 gma
1 4 43 3.00000000E-01 hpo
```

1 4 44 3.00000000E+00 st
1 4 45 4.00000000E-01 scx
1 4 46 0.50000000E+00 ALPHAC
1 4 47 0.35500000E+00 A1C
11 11 210 -999 change to undrained model (2) and 10=MIT-E3
1 11 31 4.78000000E-01 lambda
1 11 32 3.40000000E+00 1+e0
1 11 33 4.00000000E-03 kappa
1 11 34 0.94000000E+00 2G/K
1 11 35 1.15200000E+00 (1+2K0)/(3-3K0)
1 11 36 9.50000000E-01 yield surface ratio of semi axes
1 11 37 1.00000000E+02 rate of rotation of yield surface
1 11 38 0.20500000E+00 sic
1 11 39 1.04900000E+00 xkc2
1 11 40 1.55000000E+00 xmm
1 11 41 1.00000000E+01 cc
1 11 42 5.00000000E-01 gma
1 11 43 3.00000000E-01 hpo
1 11 44 3.00000000E+00 st
1 11 45 4.00000000E-01 scx
1 11 46 0.50000000E+00 ALPHAC
1 11 47 0.35500000E+00 A1C